

Niche preclinical and clinical applications of photoacoustic imaging with endogenous contrast

Samuel John^{a,1}, Scott Hester^{b,1}, Maryam Basij^{a,1}, Avijit Paul^b, Marvin Xavierselvan^b,
 Mohammad Mehrmohammadi^{c,d,e,*}, Srivalleesha Mallidi^{b,f,**}

^a Department of Biomedical Engineering, Wayne State University, Detroit, MI, USA

^b Department of Biomedical Engineering, Tufts University, Medford, MA, USA

^c Department of Imaging Sciences, University of Rochester Medical Center, Rochester, NY, USA

^d Department of Biomedical Engineering, University of Rochester, Rochester, NY, USA

^e Wilmot Cancer Institute, Rochester, NY, USA

^f Wellman Center for Photomedicine, Massachusetts General Hospital, Boston, MA 02114, USA

ARTICLE INFO

Keywords:

Photoacoustics
 Ultrasound
 Spectroscopy
 Diagnostics
 Clinical
 Endogenous
 Image-guided
 Interventions
 Theranostics

ABSTRACT

In the past decade, photoacoustic (PA) imaging has attracted a great deal of popularity as an emergent diagnostic technology owing to its successful demonstration in both preclinical and clinical arenas by various academic and industrial research groups. Such steady growth of PA imaging can mainly be attributed to its salient features, including being non-ionizing, cost-effective, easily deployable, and having sufficient axial, lateral, and temporal resolutions for resolving various tissue characteristics and assessing the therapeutic efficacy. In addition, PA imaging can easily be integrated with the ultrasound imaging systems, the combination of which confers the ability to co-register and cross-reference various features in the structural, functional, and molecular imaging regimes. PA imaging relies on either an endogenous source of contrast (e.g., hemoglobin) or those of an exogenous nature such as nano-sized tunable optical absorbers or dyes that may boost imaging contrast beyond that provided by the endogenous sources. In this review, we discuss the applications of PA imaging with endogenous contrast as they pertain to clinically relevant niches, including tissue characterization, cancer diagnostics/therapies (termed as theranostics), cardiovascular applications, and surgical applications. We believe that PA imaging's role as a facile indicator of several disease-relevant states will continue to expand and evolve as it is adopted by an increasing number of research laboratories and clinics worldwide.

1. Introduction

A primary focus of the medical imaging field for the past century has

been the capture of “snapshots” of the physiological processes occurring in an organ, tissue, or cell to diagnose a disease state or infer the effectiveness of a given therapy. Fortunately, several imaging

Abbreviations: ANSI, American National Standard Institute; BCS, breast-conserving surgery; CT, computed tomography; CW, continuous wave; CNN, convolutional neural network; DL, Deep learning; DMD, Duchenne muscular dystrophy; EVLA, endovenous laser ablation; FDA, food and drug administration; Hb, deoxyhemoglobin; HbO₂, oxyhemoglobin; HV, healthy volunteer; HIF-1 α , hypoxia-inducible factor 1 α ; HIFU, high-intensity focused ultrasound; IVPA, intravascular photoacoustic imaging; IVUS, intravascular ultrasound; LED, light emitting diodes; MRI, magnetic resonance imaging; MPE, maximum permissible exposure; MIFU, medium-intensity focused ultrasound; MIR, mid-infrared; MSOT, multispectral optoacoustic tomography; NIR, near-infrared; OCT, optical coherence tomography; pCO₂, partial pressure of CO₂; pO₂, partial pressure of oxygen; sO₂, oxygen saturation; sPA, spectroscopic photoacoustic; PA, photoacoustic; PAT, PA Tomography; PALL, photoacoustic lifetime imaging; PARS, photoacoustic remote sensing; PDT, photodynamic therapy; PTT, photothermal therapies; PET, positron emission tomography; PRF, pulse repetition frequency; RFA, radiofrequency ablation; ROS, reactive oxygen species; RNN, recurrent neural network; RPE, retinal pigment epithelium; RA, Rheumatoid arthritis; SNR, signal-to-noise ratio; SPECT, single positron emission computed tomography; SDT, sonodynamic therapy; sPA, spectroscopic PA; TRUS, Transrectal ultrasound; TPAM, Twente PA Mammoscope; US, ultrasound; UV, ultraviolet; WLI, white light imaging.

* Corresponding author at: Department of Imaging Sciences, University of Rochester Medical Center, Rochester, NY, USA.

** Corresponding author at: Department of Biomedical Engineering, Tufts University, Medford, MA, USA.

E-mail addresses: Mohammad.Mehr@urmc.rochester.edu (M. Mehrmohammadi), Srivalleesha.Mallidi@tufts.edu (S. Mallidi).

¹ Authors have equal contribution.

<https://doi.org/10.1016/j.pacs.2023.100533>

Received 10 March 2022; Received in revised form 30 June 2023; Accepted 14 July 2023

Available online 17 July 2023

2213-5979/© 2023 Published by Elsevier GmbH. This is an open access article under the CC BY-NC-ND license (<http://creativecommons.org/licenses/by-nc-nd/4.0/>).

techniques now exist that can provide a great deal of information on the disease dynamics and thus improve the precision of theranostic methodologies. While many of these technologies, such as computed tomography (CT), magnetic resonance imaging (MRI), positron emission tomography (PET), single positron emission computed tomography (SPECT), and ultrasound (US) imaging, have become foundational clinical modalities for both diagnosis and therapy monitoring, there remains a dearth of imaging methods which could monitor real-time physiological processes in a cost-effective manner without the need for exogenous contrast agents [1–4]. The turn of the century has seen a tremendous rise in some novel optical imaging technologies based on the unique optical scattering, absorption, transmission, and reflectance properties of tissues [5]. Amongst these techniques, photoacoustic (PA) imaging has garnered significant interest and popularity due to two of its unique features - facile integration with the widely available US imaging systems and its ability to image endogenous chromophores such as hemoglobin at much higher penetration depths and decent resolution than any other optical imaging techniques [6].

PA imaging, also known as optoacoustic imaging, is a non-ionizing modality based on the production of US waves generated from nanosecond-pulsed light absorption and the subsequent thermoelastic expansion of a chromophore [7]. A multitude of chromophores can accomplish this, whether they be endogenous (hemoglobin, melanin) or exogenous (dyes, nanoparticles) to the human body. By relying on acoustic waves as a basis of signal detection, instead of reflected or scattered photons, deeper tissue regions can be imaged as the attenuation of acoustic waves in the body is far less than it is for photons. A far cry from the first biomedical implementation of this dynamic, modern PA imaging has seen a marked increase in the fidelity of several imaging parameters courtesy of the development of novel probes, detectors, light sources, and image-processing methodologies [8]. Furthermore, several preclinical and clinical studies involving PA imaging to diagnose and monitor therapies for various malignancies such as cancer and cardiovascular disease, in addition to guiding surgical procedures, have successfully been demonstrated by many research groups [9–12]. In fact, a PubMed® query last year with keywords “Photoacoustic” OR “Optoacoustic” on either the title or abstract yielded 5086 articles. Amongst these articles, 438 were review articles with exclusion criteria such as non-biological applications, case studies, non-English articles, and magazine articles. We identified that 115 articles (~26%) were on applications or technological advancements of photoacoustic imaging, and 8.5% were on the use of development of contrast agents, nanoparticles for imaging, and image-guided therapies. The remaining articles fell under the multimodal imaging technical advancements, imaging, and theranostics applications, where photoacoustic imaging was not the focus. Analyzing the publications further also indicated that the number of publications has risen exponentially, substantiating PA imaging’s aggressive proliferation in the scientific community. The last decade has seen a revolution in biomedical applications of nanotechnologies which have furthered the development of exogenous contrast-augmented PA imaging. Nanoscale entities with inherent high optical absorption properties, such as inorganic plasmonic particles, dyes, and carbon nanotubes, have been deployed alone or encapsulated within nanostructures such as liposomes to enhance PA contrast exogenously and deliver targeted therapeutics with greater precision [13–17]. There has been a steady increase in the percentage of publications in recent years that have demonstrated various applications using photoacoustic contrast agents [18]. While PA imaging with nano contrast agents holds tremendous potential for various precision medicine applications, its full impact has yet to be explored. In addition to their limited clinical applications at this time, non-bioinspired or inorganic metal nanomaterials are also limited by their biocompatibility and cytotoxicity profiles. In light of these observations and the recent advances in preclinical and clinical PA imaging, this review aims to provide a comprehensive look at niche applications of PA imaging utilizing endogenous contrast alone. Specifically, we present the diagnostic, tissue characterization, surgical

guidance, and therapeutic monitoring capabilities of PA imaging and discuss modern advances fostering this unique technology towards broad clinical adoption and deployment. The review does not include details on electronics and data acquisition of photoacoustic signals as they have been recently reviewed elsewhere [19]. The review is divided into two major sections: (a) diagnostic applications and (b) image guided-therapy applications involving PA imaging, with a discussion on the limitations and challenges of PA imaging in clinical settings for the finale.

2. Diagnostic applications of PA imaging

PA imaging provides a wealth of physiological data about the biological systems using which decisions on the type of therapeutic options and related dosimetry can be made. The contrast of PA imaging relies on the optical absorption properties of the tissue chromophores being imaged. In other words, PA imaging can be used to distinguish between different chromophores by tuning the nanosecond pulsed laser wavelength to match the absorption spectra peak of the target chromophore. Of the many serendipitous qualities of the different chromophores and molecules in the mammalian body that allow for scientific exploitation and signal acquisition, the optical spectroscopic profiles of blood were maximally exploited by PA imaging. This is due to the protein hemoglobin that can absorb visible and near-infrared (NIR) laser irradiation (Fig. 1(i)) to generate signals that are strong enough to allow for differentiation between vascular and non-vascular tissues. PA imaging can use similar or the same electronics as other non-invasive methodologies such as US imaging where the transducers detect acoustic waves generated because of optical energy deposition and the consequent thermoelastic expansion. This ability allows for the overlay of physiological structures obtained from ultrasound with the PA contrast obtained from vasculature, and the oxygenation status of an imaged tissue, all within a single system [20–23]. Several PA imaging techniques based on chromophores not limited to blood are described in the sections below, and they serve as excellent examples of the breadth of information PA imaging can provide in many diagnostic and therapeutic settings. For example, the variation in optical properties of tissue chromophores’ during tissue ablation or treatment and the ability of PA imaging to detect these changes makes it a suitable candidate for image-guided therapeutic procedures. In surgical nerve blocks, PA imaging distinguishes nerves from surrounding structures including tendons to minimize nerve punctures [24]. In addition to characterizing chromophores, PA imaging adds tissue temperature information to aid in surgeries. PA imaging monitors real-time tissue temperature which can provide useful feedback in thermal therapies as it allows the surgeon to control the laser energy to provide an effective therapy and minimize collateral tissue damage [25]. All of these diagnostic applications of PA imaging are discussed in the sections below organized by the chromophore of interest.

2.1. PA imaging of vasculature and blood oxygen saturation

Hemoglobin is an excellent endogenous chromophore that provides PA contrast in the visible and NIR range (Fig. 1(i)). PA imaging in addition to providing information about vasculature, can also provide functional information. Oxygen saturation (sO_2) of blood can be extracted from PA images, courtesy of the unique spectroscopic profiles of oxy- (HbO_2) and deoxy-hemoglobin (Hb). When oxygen molecules bind to hemoglobin, its optical properties change, resulting in a change in the absorption spectrum. This enables determining the oxygenated and deoxygenated blood ratio and combination of several visible and NIR wavelengths have been used for the purpose [31–33]. Due to this dynamism, in vivo imaging of vascular structures and their oxygen content can be conducted to diagnose and monitor many maladies ranging from a tumor [34], and wound healing [35,36] to the absence of sufficient oxygenation of tissues in the case of stroke [37,38] or

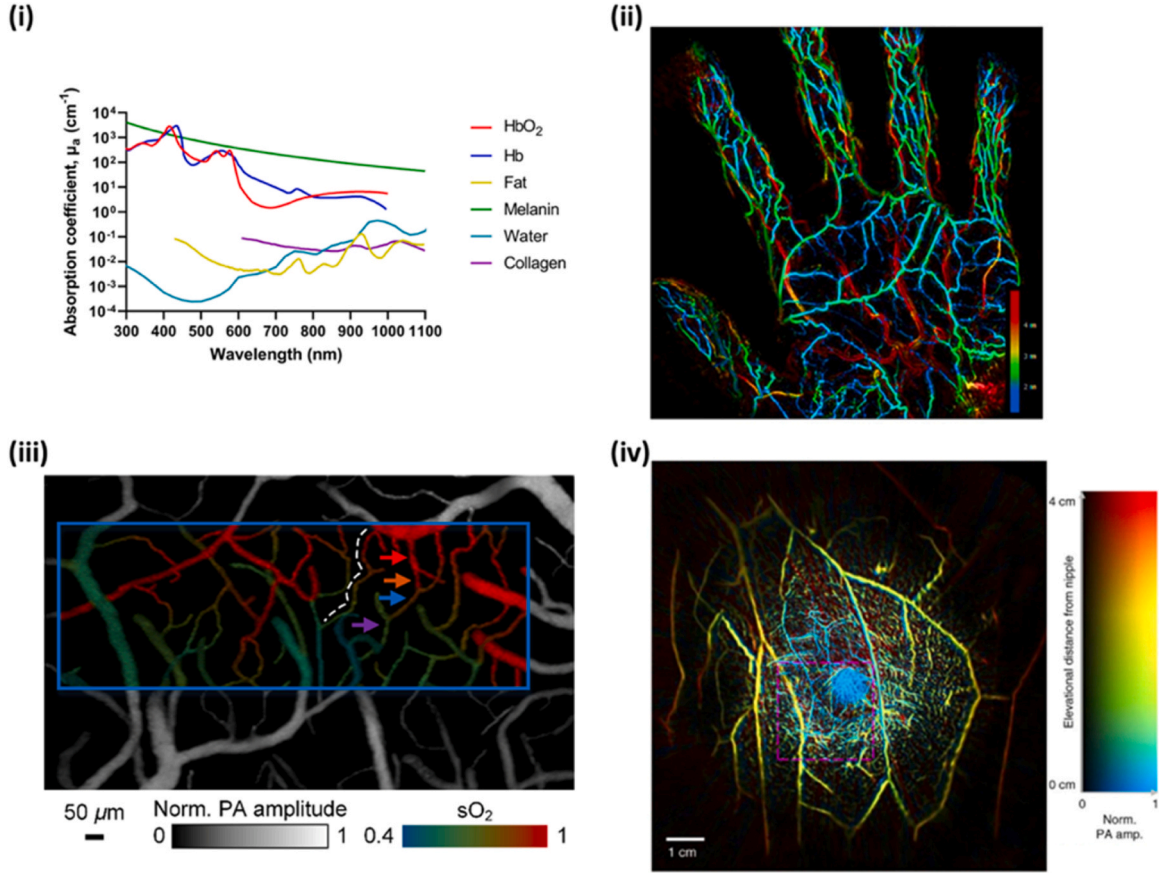


Fig. 1. (i) Absorption coefficient, μ_a (cm^{-1}), as a function of wavelength for several tissue chromophores such as HbO_2 , Hb, fat, melanin [26] and Water. Collagen from [27]. (ii) Maximum intensity projection of PA image of the blood vessels in the palm obtained at 795 nm. The color bar represents the depth. (iii) Oxygen saturation mapping of the somatosensory area in response to electrical stimulations. The blue rectangle represents the region of interest for subsequent functional imaging analysis. (iv) Vasculature in the right breast of a healthy female volunteer obtained using PA computed tomography. The image has been color-coded to represent depth.

(ii) Adapted from [28]. (iii) Adapted from [29]. (iv) Adapted from [30].

placental dysfunction [32], or brain function [39].

To understand the mathematical principle behind the multiple wavelength imaging approach, we first need to ascertain the number of unknown variables, i.e., the concentrations of Hb and HbO_2 . Consider absorption coefficients of Hb and HbO_2 at two wavelengths λ_1 and λ_2 , then $\mu_a^{\lambda_1}$ and $\mu_a^{\lambda_2}$ (cm^{-1}), respectively can be represented as the equations below

$$\mu_a^{\lambda_1} = \epsilon_{\text{Hb}}^{\lambda_1} * C_{\text{Hb}} + \epsilon_{\text{HbO}_2}^{\lambda_1} * C_{\text{HbO}_2} \quad (1)$$

$$\mu_a^{\lambda_2} = \epsilon_{\text{Hb}}^{\lambda_2} * C_{\text{Hb}} + \epsilon_{\text{HbO}_2}^{\lambda_2} * C_{\text{HbO}_2} \quad (2)$$

where, $\epsilon_{\text{Hb}}^{\lambda}$ and $\epsilon_{\text{HbO}_2}^{\lambda}$ are Molar extinction coefficients (unit: $\text{cm}^{-1} \text{M}^{-1}$) for Hb and HbO_2 , respectively at a specific wavelength λ ; C_{Hb} and C_{HbO_2} are the corresponding molar concentrations of the two types of absorbing hemoglobin chromophores. From Eqs. (1) and (2), we can solve for C_{Hb} and C_{HbO_2} as follows:

$$C_{\text{Hb}} = \frac{\epsilon_{\text{HbO}_2}^{\lambda_1} * \mu_a^{\lambda_2} - \epsilon_{\text{HbO}_2}^{\lambda_2} * \mu_a^{\lambda_1}}{\epsilon_{\text{Hb}}^{\lambda_2} * \epsilon_{\text{HbO}_2}^{\lambda_1} - \epsilon_{\text{Hb}}^{\lambda_1} * \epsilon_{\text{HbO}_2}^{\lambda_2}} \quad (3)$$

$$C_{\text{HbO}_2} = \frac{\epsilon_{\text{Hb}}^{\lambda_2} * \mu_a^{\lambda_1} - \epsilon_{\text{Hb}}^{\lambda_1} * \mu_a^{\lambda_2}}{\epsilon_{\text{Hb}}^{\lambda_2} * \epsilon_{\text{HbO}_2}^{\lambda_1} - \epsilon_{\text{Hb}}^{\lambda_1} * \epsilon_{\text{HbO}_2}^{\lambda_2}} \quad (4)$$

Now, the oxygen saturation ($s\text{O}_2$) of hemoglobin can be calculated in the blood from Eqs. (3) and (4) using the formula: $s\text{O}_2 = \frac{C_{\text{HbO}_2}}{C_{\text{HbO}_2} + C_{\text{Hb}}}$, which

ultimately can be rewritten as:

$$s\text{O}_2 = \frac{\epsilon_{\text{Hb}}^{\lambda_1} * \mu_a^{\lambda_2} - \epsilon_{\text{Hb}}^{\lambda_2} * \mu_a^{\lambda_1}}{\epsilon_{\text{diff}}^{\lambda_2} * \mu_a^{\lambda_1} - \epsilon_{\text{diff}}^{\lambda_1} * \mu_a^{\lambda_2}}$$

$$\text{where } \epsilon_{\text{diff}}^{\lambda} = \epsilon_{\text{Hb}}^{\lambda} - \epsilon_{\text{HbO}_2}^{\lambda}.$$

Recent examples of utilizing blood as contrast in PA imaging are provided in Fig. 1. The maximum intensity projection of blood vessels in the palm of a hand obtained with 795 nm and color coded based on the depth of the blood vessels is shown in Fig. 1(ii) [28]. The superficial palmar arch, the common palmar digital arteries, and the proper palmar digital arteries were located deeper than the vein network in the palm. PA imaging can also provide functional imaging particularly the blood oxygen saturation as shown in Fig. 1(iii) that displays the functional image of somatosensory cortex of the brain in response to electrical stimulations [29]. The structure of microvessels along with its oxygenation status can be clearly observed. As the vasculature of both normal and diseased tissues can be obtained with PA imaging, it can be used to detect and diagnose cancers particularly of breast. Fig. 1(iv) shows the blood vessels in the entire breast tissue [30]. Furthermore, the image has also been color coded for depth of the vasculature in the breast providing a comprehensive volumetric vascular information in the breast tissue.

The interplay between partial pressure of oxygen (pO_2) and blood $s\text{O}_2$ has been of interest in various diseases, given that understanding the molecular and cellular oxygenation changes within tissue can provide critical diagnostic inferences. Particularly in oncology, understanding hypoxia in cancer treatment is vital as hypoxia is often linked with

tumor propagation, malignancy, and resistance. Gauging tumor vascular heterogeneity and the associated hypoxia becomes critical in evaluating treatment success. Currently, there are no clinically used techniques that can provide full extent of hypoxia in real-time. Histology is often used as reliable gold standard in assessing tissue hypoxia but is met with limited spatial and temporal processing. Similarly spatial sampling of the heterogeneous microenvironment is not possible with electrodes measuring partial pressure of oxygen. Various imaging techniques have been employed in scaling hypoxia such as, functional MRI and PET [40]. However, these techniques suffer from spatial resolution and lack of ability to produce image contrast without using external molecules. As PA imaging can exploit the optical absorption property of endogenous hemoglobin, it can provide functional information of tumor vasculature and blood oxygen saturation. Further, PA imaging is in mesoscale and can provide superior optical contrast with a reasonable penetration depth. Many studies have demonstrated the functional PA imaging as a surrogate biomarker for tumor oxygenation and its utility in gauging changes to tumor microenvironment in response to therapy and predicting the treatment response preclinically and clinically [34,41–43]. Some of the preclinical studies in the last decade have been summarized in Table 1 below.

Monitoring of vascular function and sO_2 is desirable to diagnose several malignancies, including breast cancer, ovarian cancer and thyroid cancer [41,49,55]. Specifically, here we provide technical advances on imaging breast tumors given the recent approval of utilizing PA imaging for diagnosing breast cancer in humans [56]. Existing techniques including mammography, B-mode US imaging, and MRI are used for screening and differential diagnosis of breast cancer [57]. Limitations such as the poor diagnostic performance in women with dense breasts by mammography [58,59], poor specificity in B-mode US imaging [60], and the fact that MRI is not point-of-care and readily available to patients, indicate a clinical need for more advanced diagnostic tools. The

anatomy of the breast tissue makes it a suitable candidate for PA imaging since there are many different ways to deliver laser light and detect PA signals from the breast tissue. Exploiting the PA effect, PA tomography (PAT) provides molecular and functional information about the tumor within the breast tissue [6,30,61]. Spectroscopic PA (sPA) imaging provides sO_2 maps that can act as an important indicator of cancer progression [61] and an important biomarker of tumor angiogenesis [62].

Breast PA imaging systems are divided into three categories based on the system configurations and geometries: a) PA mammoscopic system; b) tomographic (volumetric) imaging systems using hemispherical or ring-array transducers; and c) planar using phased or linear array transducers. PA mammoscopy system was introduced by researchers at University of Twente. This system includes the Twente PA Mammoscope (TPAM), which uses a pulsed laser excitation source of $\lambda = 1064$ nm for visualizing most malignant tumors in compressed breasts with high contrast [63]. The system uses a 2D US detector array of 590 elements to generate uniform 3D spatial resolution equipped images (Fig. 2a). The next generation of the TPAM 2 was developed in a form of a volumetric tomographic system to overcome the limitations of the first prototype including a limited field of view (90×80 mm² of the detector surface area), limiting whole breast coverage and breast compression-induced patient discomfort [64]. In contrast to a single imaging wavelength, this modified system utilizes a dual-wavelength approach ($\lambda = 1064$ and 755 nm) for illuminating the breast in a fashion where one beam illuminates the nipple, and nine different beams illuminate the ventral sides (Fig. 2b-c). 3D US and PA images indicate clear vascularization superimposed with anatomical information of the patient's breast in a prone position, within a water-filled imaging tank are probed through 12 arc-shaped detector arrays of 32 elements each. This system provides an imaging depth of 22 mm, oxygen saturation probing capabilities, and reveals information about the lactiferous ducts within the nipples.

Table 1

Summary of a few selected preclinical studies in the last decade where photoacoustic imaging was used to monitor vascular function in response to therapy in various preclinical tumor models.

Disease Ontology	Model	Wavelength (nm)	Therapy and Biomarkers	Imaging Apparatus	Reference
Basal Cell Carcinoma	Mouse	532/785	Evaluation of vascular/tumoral destruction following photodynamic therapy,	Custom	[44]
B-cell Mantle Cell Lymphomas	Mouse harboring patient-derived xenografts	750/850	Analysis of oxygenation and vasculature formation as indicators of tumoral aggressiveness, foundation for future post-therapy efficacy studies	Vevo 3100/LAZR-X	[45]
Breast Cancer	Mouse harboring 4T1 murine or KPL4/MDA-MB-231 human breast cancer tumors	690 – 900	Characterization of whole tumors via vasculature dynamics and oxygenation status	Custom	[46]
Breast Cancer	Mouse harboring human EMT-6 breast cancer tumor	750/850	Evaluation of tumor response to liposomal doxorubicin by quantifying drops in oxygen saturation post-treatment	Vevo LAZR	[47]
Breast Cancer	Mouse harboring human KPL-4/MDA-MB-468 breast cancer tumors	700 – 900	Evaluation of tumor response to bevacizumab treatment by quantifying drops in oxygen saturation post-treatment	iThera In Vision 256-TF	[48]
Breast Cancer	Mouse harboring MDA-MB-231 breast cancer tumors	700–900	Differentiation of bevacizumab responders from non-responders	iThera In Vision 256-TF	[49]
Glioblastoma	Mouse	750/850	Early (24 h) prediction of tumor recurrence following photodynamic therapy as a metric of oxygenation changes	Vevo LAZR	[34]
Head and Neck Cancer	Mouse harboring patient-derived xenografts	750/850	Analysis of fractionated radiation therapy on HPV +/- tumors via oxygenation change correlations as an early indicator of treatment efficacy	Vevo LAZR	[50]
Hypopharyngeal Squamous Cell Carcinoma	Mouse	850	Detection and characterization of subcutaneous tumors via vasculature density	Cyberdyne AcousticX	[51]
Prostate Cancer	Mouse harboring human PC3 and LNCaP prostate cancer tumors	700–880	Demonstration of differences in vascularity and oxygen dynamics between 2 prostate cancer types	iThera In Vision 256-TF	[52]
Cancers of the Throat and Trachea	Rabbit	562/584	Generation of baseline oxygenation dynamics and vascular structure for the detection of aberrations, presence of tumors	Custom	[53]
Pancreatic tumors	Mouse harboring AsPC-1 pancreatic adenocarcinoma tumors	750/850	Correlation of pre-treatment to post-treatment tumor oxygenation dynamics and growth rate	Vevo 3100/LAZR-X	[54]

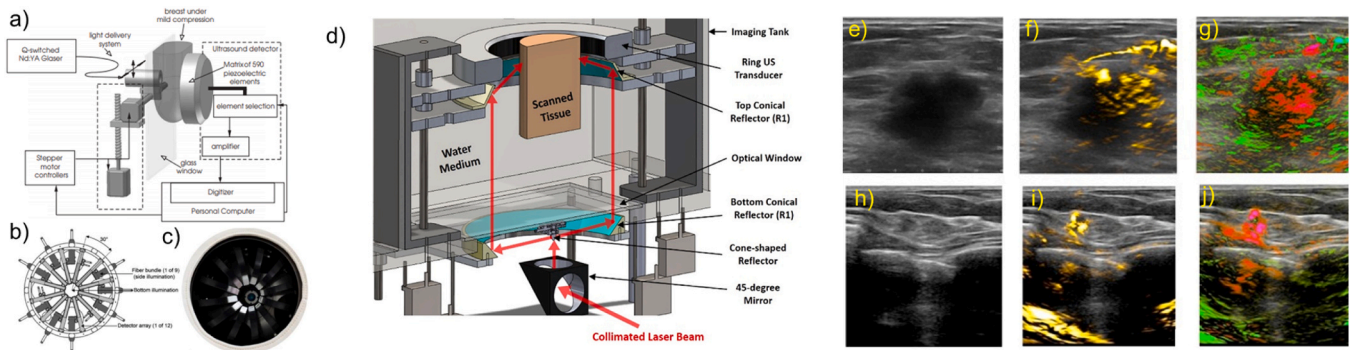


Fig. 2. PA image-guided breast cancer detection: Planar PAT breast cancer detection systems include Mammoscope systems, such as a) Schematic of the PA mammoscope. (a) The compressed surface of the breast between the glass window and flat detector matrix is illuminated locally by a pulsed laser source of $\lambda = 1064$ nm which is scanned in two dimensions. b) illustration indicating the top view of the imaging tank. The breast is illuminated at the nipple (bottom) and sides. US and PA images are acquired through an array of 12 detectors. c) Photograph of the imaging tank. PAT system based on ring geometry: d) 3D view of the PAT system indicating a ring transducer, a pulsed laser, a cone shaped reflector and 2 conical reflectors. US/ PA images probed by this system indicate a uniform PA signal across the scanned cross-sectional area of the tissue being imaged. Linear array-based US/ PA breast cancer detection: e) US image indicating a malignant mass measuring 260 mm. f) Total hemoglobin map indicated in yellow referring to the highest density micro- and major vasculature. Oxygenation map seen in g) and j), where red indicates regions below an oxygen saturation of 85% and green color indicates normally oxygenated regions ($>90\%$). (g) Diffuse internal blood deoxygenation is indicated by PA imaging. h) Low contrast US image indicating a small ductal carcinoma measuring 4 mm in diameter. i) High density of total hemoglobin is seen around a small core. j) Significant blood hypoxia is seen on the oxygen saturation map. (a) Image adapted from [63]. (b, c) Image adapted from [64]. (d) Image adapted from [68]. (e-j) Image adapted from [70].

Another PA tomography system, named LOUISA-3D, was developed by Oraevsky et al. This imaging system utilizes a patient's breast-compatible hemispherical mold. An arc-shaped array (96 elements) and fiber bundle coupled to tunable pulsed laser wavelength $\lambda = 755 - 795$ nm illuminate the breast from different angles and rotate around the breast to provide volumetric co-registered PA and US tomographic images with high isotropic spatial resolution [65]. The system merits advantages such as full breast coverage and the capability of providing functional information. Another example includes a dedicated 3D PA breast cancer detection system, which was developed by Kruger, Robert A., et al. [66]. This imaging system used a 512-element hemispherical detector array to acquire the PA signals from a breast tissue positioned in an optically clear, water-filled spherically shaped cup illuminated by pulsed lasers of wavelength $\lambda = 756$ nm. This system provided 3D PA images of the breast tissue with clear vasculature and demonstrated potential for imaging large breasts at depths up to 53 mm. Ring based PAT system includes the single breath hold - PA computed tomography system (SBH-PACT) [30], developed by Lin et. al, and all-reflective full ring illumination/acquisition system was also proposed by Alshahrani et al. [67]. The SBH-PACT included a modified mammography design, where the compressed breast is placed between a 512 element-ring transducer and is illuminated with an imaging wavelength of $\lambda = 1064$ and 750 nm. Multi-wavelength imaging capability of this system provided sO_2 maps at penetration depth upto 4 cm. A ring-based PAT system without breast compression was developed by Alijabbari et al. [68]. This imaging system included a 256-element ring transducer (Fig. 2d) and uses a multi-wavelength approach for acquiring co-registered US and PA images [69]. Multispectral capabilities allow the system to probe functional properties of different tissue chromophores including tumor vasculature. In contrast to other illumination strategies, this system provides a uniform PA signal between the imaging depths of 10–20 mm [68]. Proof-of-concept studies validated the lower fluence and a greater cross-sectional illumination depth providing capability of this imaging system. A linear array US and PA 128 element probe equipped imaging system, known as Imagio was developed. This handheld probe was used for real-time visualization of tumors measuring 10 mm in diameter at an imaging depth of 3 – 20 mm and large blood vessels at an imaging depth of 40 mm [70]. Illumination was achieved through a dual wavelength $\lambda = 1064$ and 757 nm coupled fiber attached to either side of the transducer. This is the only food and drug administration (FDA) approved PA based system for breast cancer

detection [71]. Moreover, this FDA approved medical imaging system also provides relative total hemoglobin concentration within and around the tumor along with the sO_2 map of the tumor (Fig. 2e-j). In summary, imaging vasculature in deep tissues has become synonymous with PA imaging. However, PA imaging does suffer certain limitations despite being a non-ionizing and non-invasive modality. The depth of imaging and motion-induced artifacts are two of the biggest hurdles for clinical PA imaging today [72,73]. Fortunately, these hindrances to performance are being whittled away by the technological advancements such as leveraging algorithmic data refinement and endoscopic sources of PA excitation and US reception [53,72,74].

In the treatment of cancer, oxygenation is crucial for understanding and forecasting the behavior of a tumor's response to treatment [75]. For example, by monitoring the blood vessels of a tumor and the increase or decrease in oxygenation, we may gauge that the tumor is attempting to become hypoxic post therapeutic effect or increase its glycolytic processing and vascular recruitment for growth and metastasis [76]. Understanding these facets of tumoral behavior is critical for successfully deploying the most efficacious therapy possible at the onset of treatment, in addition to making judgment calls at critical junctures in the planning and follow-up phases of cancer treatment. The same can be said of treating strokes, and PA imaging has proven its efficacy in studying the occlusion, reperfusion, and neovascularization of tissues affected by infarcts [77,78]. The presence, destruction, and neogenesis of vessels may also be easily imaged using PA imaging, and pertains to all of the above conditions as an indicator of either successful vascular destruction via techniques such as photodynamic therapy (PDT), photothermal therapy (PTT), and sonodynamic therapy (SDT) or the detection of vasculature that is not easily seen by white light imaging (WLI) for therapeutic image-guidance [79–81]. Lastly, the severity of symptoms of inflammatory ailments such as rheumatoid arthritis has been shown to exhibit tight correlations to the presence of reactive oxygen species (ROS) and aberrations in pO_2 , pCO_2 , and pH, which can be extrapolated using PA imaging of hemoglobin as an indicator of pO_2 values and therefore a proxy of pCO_2 content [82]. We list below examples of these applications of PA imaging for the monitoring of therapeutic efficacy.

The development of a cancerous state within a cellular system is a complex product of innumerable factors acting alone or in tandem, from oxidative stress or immune challenges to interplays between cellular signaling networks and environmental factors such as diet and radiation

exposure [83–86]. The monitoring of tumor dynamics pre-treatment, during treatment or post-treatment is critical to successfully forecast its behavior and deploy the appropriate therapy for a given tissue. For example, Mallidi et al. have established an algorithm-based ultrasound and photoacoustic imaging pipeline for the classification of tumoral responses to therapy (specifically PDT) as a factor of tumoral oxygenation content [34]. US imaging was used to differentiate tumoral boundaries from proximal healthy tissue. By combining 3D PA imaging on top of US boundary profiles, the oxygenation content of tumors was successfully pseudo-mapped onto their therapeutic response. This allowed for a novel look at tumoral responses during and following the treatment and established an unprecedented method for predicting tumor recurrence. While sO_2 of blood is a surrogate marker for tumor oxygenation status, Shao et al. performed measurements of partial pressure of oxygen (pO_2) content across large regions of tissue based on photoacoustic lifetime measurements of methylene blue dye [87]. Often paramount to the success or failure of a given therapy, the availability or lack thereof of nutrients, signaling agents, and oxygen can be easily monitored using PA imaging of the vasculature as a proxy for the availability of all three. Should the desired clinical endpoint be an increase in these elements, PA imaging of vasculature can easily detect the dilation or neogenesis of novel arteries and veins and thus an increase in the availability of these components [88]. In contrast, the destruction of vasculature is a foundational way to deprive misregulated cellular systems affecting a broader population of cells or tissues and maybe imaged just as easily with PA imaging [44]. Fortunately, many technologies exist that can destroy tumor vasculature, which may use light to generate cytotoxic substrates or ROS as in the case of PDT, or sound to acoustically convert drugs into an active form as in the case of SDT [23, 89]. As PA imaging may be deployed to monitor vascular growth as a proxy for tumoral behavior, it can also be deployed to monitor vascular destruction, as illustrated by the work of Rohrbach et al. or Quiros-Gonzalez et al. for the imaging of vascular destruction in tumors [44,49]. Monitoring these processes can be done in real-time using PA imaging paired with US imaging to follow the evolution of tumoral vasculature and its destruction during therapy. We are observing a rise in clinical applications involving blood sO_2 monitoring during therapy, given the lack of exogenous contrast agents. For example, Fig. 9(d) shows demonstration of sO_2 measurements in the human thyroid tumors [41]. Future pairing with endoscopes and other intra-operative devices for intimate imaging of deep-seated tissues within the body [53] will further catapult the technique into routine clinical use.

2.2. PA imaging of melanin

Melanin is one of the most abundant light-absorbing polymers in the body, derived through multi-stage chemical processes such as the oxidation of tyrosine. In addition to skin, melanin can also be found primarily in the eye, and circulatory system, particularly in the instances of metastatic melanoma [90]. Due to its photochemical and photobiological properties, melanin can be detected and quantified by several optical spectroscopy techniques [91–94]. Specifically in PA imaging the high optical absorption of melanin has aided in its detection within tissues such as the retina [95,96], lymph nodes [97], and skin-based applications [98,99]. In contrast to hemoglobin, melanin has a broad absorption spectrum that spans from visible light to NIR wavelengths (400–1064 nm) and thus allows for a wide range of excitation wavelengths to be used in photoacoustic imaging [100–102].

Within the ocular tissues, melanin can be found in the uvea (the iris, choroid, and ciliary body) and is particularly found in high concentrations in pigmented tumors (e.g., eye melanoma) [95,101]. Silverman et al. used the laser wavelengths of 532 and 1064 nm to obtain melanin maps in ocular tissues [95]. Melanin has higher absorption at 532 nm than at 1064 nm and as expected, the study also showcased higher PA signal at the former wavelength than the latter, despite the latter wavelength generating images with higher penetration depth. In

another study conducted by Shu et al. retinal pigment epithelium (RPE) melanin and choroidal melanin were distinguished from each other as the axial resolution in a PA imaging system ($< 10 \mu\text{m}$) was very high [96,103]. In this study, a Monte Carlo simulation was also used to obtain light absorption dynamics in the retina to optimize the bandwidth for PA microscopy systems and increase its spatial resolution. Beyond ocular imaging, melanin detection in the circulatory system can improve both the prognosis and the treatment plans for melanoma, the most lethal form of skin cancer [104]. To this end, several groups have demonstrated the utility of PA imaging in the detection and eradication of circulating metastatic melanoma cells [105,106]. Interestingly, Wang et al. [107] showed that the PA imaging of melanoma cells at the wavelength of $\lambda = 764 \text{ nm}$ allows for high contrast between hemoglobin ($\lambda = 584 \text{ nm}$) and melanin for a given tissue. However, this study was limited to detecting thin superficial melanomas due to the low penetration depth at the imaging wavelength. Unfortunately, melanin and circulating blood cannot be distinguished in the ultraviolet (UV) and visible wavelength range due to the overlap in spectral absorption of the two targets [108]. The work of Langhout et al. [97] made strides to this end by comparing spectral profiles of various chromophores in the wavelength range of 680–970 nm. Although their method could discriminate between hemoglobin and melanin, a small melanoma lesion could not be adequately detected due to weak PA signal strength, which lead to a low correlation with its reference spectrum. This shortcoming was overcome by Zhang et al. [109] by reconstructing z-stacks of PA images (obtained with wavelength illumination at 764 nm) to create a 3D morphological data set that enabled resolving features that would otherwise be lost from a 2D PA image alone (Fig. 3 (i) & (ii)).

Skin pigmentation is due to the accumulation of melanin-containing melanosomes in the basal layer of the epidermis. Epidermal melanin is a broadband optical absorber and is found in large quantities in the human skin. The presence and concentration of melanin in a tissue can be used as a predictor to gauge the light dosage necessary for the maximal effect in phototherapies [110]. For instance, a physician could theoretically provide an optimized laser fluence for a given therapy depending on the abundance of melanin in the skin to minimize off-target cytotoxicity. Viator et al. demonstrated this concept by utilizing a Nd: YAG (neodymium-doped yttrium aluminum garnet) laser at 532 nm to irradiate skin via an optical fiber. By binning the melanin profiles of the imaged skin into six classes based on the strength of PA signal generated, disparate dosimetry metrics were established for the guidance of future cutaneous therapeutic applications and thus minimizing cytotoxicity based on the melanin content of a patient's skin [111]. Researchers have also tried to measure the thickness of melanoma before the surgery so that they can accurately assesses the depth and the spatial extent of the tumor at the time of biopsy and also can choose sample location by demarcating the desired periphery [98]. The co-registered US-PA images (Fig. 3(iii)) along with the 3D map of the tumor volume obtained from the spectral unmixing process denote that their detection system can be implemented in the clinics before the actual biopsy so that the cutaneous lesion thickness can be accurately calculated. General applications involving melanin, such as imaging of moles [112], hair follicles [113] and skin allergies [114] were also demonstrated by several groups. The clinical translation of PA imaging for melanoma might possibly be materialized once the issues involving spectral coloring and motion artifacts have been resolved. In summary, the biodistribution of melanin, vital for the dermatologic assessment of skin and laser procedures, can be provided by PA imaging. Some of the recent studies showcasing photoacoustic imaging of melanin for various biological applications are summarized in Table 2.

2.3. PA imaging of collagen and water content of tissue

Collagen is a family of extracellular matrix proteins that plays a critical role in providing structural support to tissues and regulating

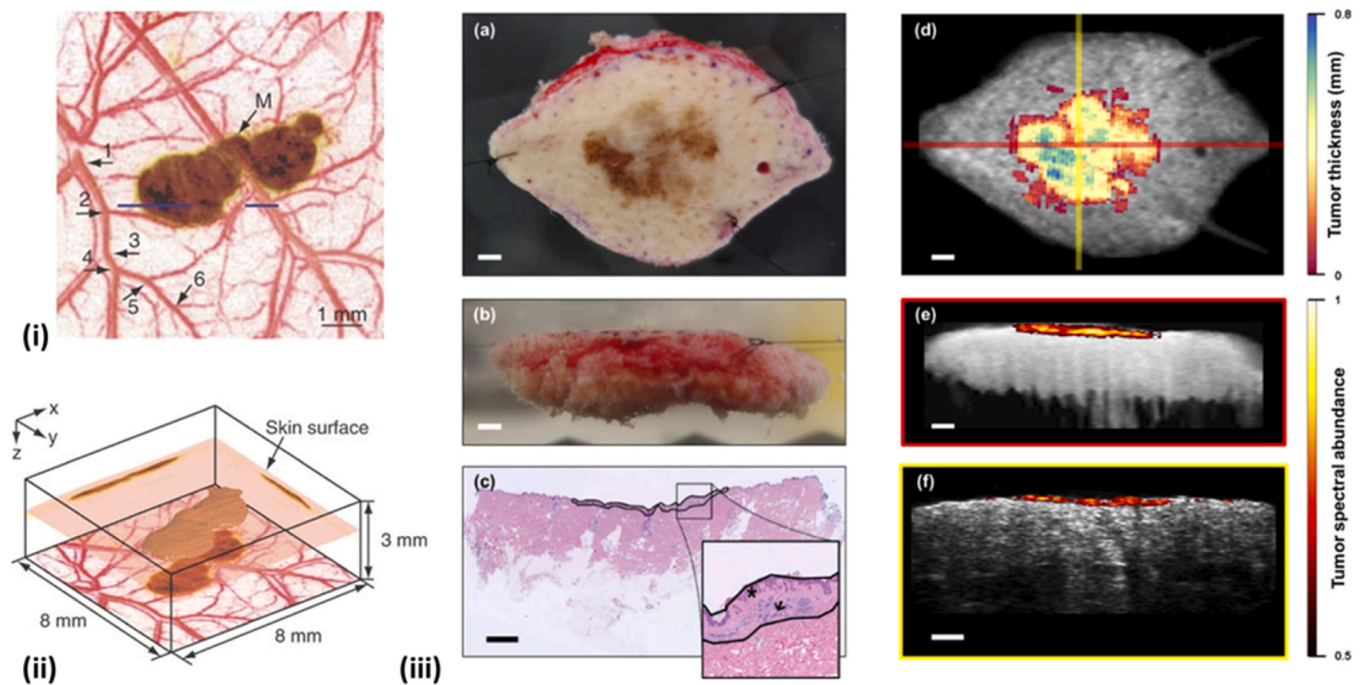


Fig. 3. (i) A composite image of the maximum-amplitude projection along z-axis. Blood vessels imaged at 584 nm and melanoma imaged at 764 nm are shown by red and brown color, respectively. (ii) 3D image of detected melanoma from acquired PA data at 764 nm. (iii) Left column: Photographs of in situ melanoma on the top of the benign dermal layer captured from above (a), Captured transversely (b) and corresponding histopathological image where star denotes the melanoma and arrow signifies the benign dermal layer. Multiwavelength PA images generated by the spectral unmixing are superimposed with the structural ultrasound counterparts (d-f). The colored portion is the spatial extent of the tumor as denoted by the PA imaging. (i, ii) Adapted from [109] (iii). (b) Adapted from [98].

cellular behavior, including the facilitation of vascular elasticity and tissue repair [141]. Collagen has unique optical absorption properties that enable multi-wavelength PA imaging to differentiate it from other chromophores such as lipids and blood in the tissue. A recent study on tissue fibrosis utilized multispectral optoacoustic tomography (MSOT) to provide information on the collagen content of tissues in pigs and humans with Duchenne muscular dystrophy (DMD) disease. The results showed that collagen content (quantified based on spectral unmixing of PA signals) significantly varies between healthy and diseased patients (Fig. 4(iii)) [142]. This study highlighted the importance of PA imaging as a continuous monitoring tool of collagen content in biological tissues.

Collagen is a critical component of atherosclerotic lesions. The differences in optical absorption coefficients of standard plaque components like lipids, water, blood, and collagen enable characterizing various atherosclerotic plaques. The ratio of lipids and collagen can be leveraged to classify plaques for designing specific therapeutic regimens [144,145]. In the work of Wang et al., the mapping of lipid and collagen content was possible due to multi-wavelength PA imaging. Specifically, PA images obtained with a total of 60 wavelengths between the range of 1650–1850 nm were used for unmixing the spectral information from the lipids and collagen with alternating least square analysis [146]. Similarly, Sethuraman et al. utilized the multi-wavelength intravascular photoacoustic (IVPA) imaging (680–900 nm range) to characterize the vulnerability of atherosclerotic plaques. IVPA imaging on a normal aorta and aortic tissue obtained from a rabbit model of atherosclerosis showed high correlation between the collagen deposits in the thickened fibrous cap of the plaque and the histology images across the same cross-section (Fig. 4(i) & (ii)) [143]. Therefore, as this technique was validated in *ex vivo* tissues, its integration with technologies that can glean such data from within a live animal or humans will be instrumental for predicting, identifying, and subsequent post-therapy analysis of diseases stemming from atherosclerotic events.

Aberrant collagen concentrations exist in non-alcoholic fatty liver diseases. These liver disorders arise due to hepatic fat accumulation and

inflammation, resulting in hepatocytic injury and eventual loss of function [147]. Imaging this detrimental event can be observed via $\lambda = 1350\text{--}1390$ nm excitation of collagen, which, when paired with the concentrations of other molecules in the tissue to include blood and water will provide an intimate portrait of the physiological health of the liver, as demonstrated by Xu et al. [148]. Their PA assessment of liver health correlated well with histological analysis and may provide even more therapeutically relevant data about the constituents mentioned above when paired with studies of inhibitory drugs to slow down or prevent the spread of fatty liver diseases. As an example, the findings on the inhibitory effects of nitro-oleic acid on fatty-liver disease progression were demonstrated by Rom et al., and validated using PA imaging via inhibition of both fat and collagen deposition [149].

Collagen undergoes a sequential change through multiple phases during pregnancy, beginning with a compact structure in early gestation and transitioning to a more flexible configuration to allow for the passage of the fetus through the birth canal. This morphological shift occurs in tandem with macroscopic changes such as cervical length, effacement (thinning), and dilation [150–154]. As such, the measurement of a collagen network's reorganization paired with tissue hydration measurements can provide direct real-time analysis of cervical remodeling. Providing more accurate assessments of cervical processes earlier in gestation could aid in identifying patients at risk for prenatal complications such as pre-term birth. To address the limitation involving tissue hydration, Xu et al. applied PAT to extract the absorption spectra of various water concentrations at wavelengths between $\lambda = 925$ and 1025 nm *ex vivo* in a piece of porcine fat; [155]. Fortunately, water and collagen have different optical properties, as shown in Fig. 5(i and ii) and unfortunately, the absorption profile of lipids has a significant overlap with collagen [156]. However, the low concentration of lipids in cervical tissue makes the contribution of lipids to PA signals insignificant for this application [156,157]. In the second spectral range from 1400 to 1600 nm, though water is the dominant absorber by a factor of $\sim 6\times$, water and collagen have separate local peaks at approximately

Table 2
Table summarizing few recent studies involving photoacoustic imaging of melanin.

Applications	Species	Imaging Apparatus	Imaging wavelength (nm)	Imaging depth (cm)	Reference (s)
Ocular imaging	Mouse (in vivo)	MSOT	680–980	1.2	[115]
	Pig (ex vivo)	Vevo 2100/LAZR	680- to 970	NA	[116]
	Human (ex vivo)	Broadband PAM	532	NA	[96]
Metastatic Melanoma cells	Cells	PA flow cytometry (PAFC)	532; 820	NA	[117]
	Mouse (in vivo)	Vevo 2100/LAZR	680–970	0.5	[118]
	Human (ex vivo)	PAFC	532	1.25	[119]
Metastatic Melanoma in lymph nodes	Mouse (in vivo)	Vevo LAZR	700, 715, 730, 760, 800, 830, and 860	2.5	[120]
		MSOT	680–980 (5 nm intervals)	0.8	[121]
	Human (ex vivo)	Vevo LAZR	680–840 nm (40 nm intervals)	2	[97]
	Human (in vivo)	MSOT	680–980	2.5	[122]
Melanoma	Human (ex vivo)	Vevo LAZR-X	680–970 (5 nm intervals)	1	[98,123]
	Human (in vivo)	PA dermoscopy	532	NA*	[124]
		US-PA imaging with 3D handheld PAT	700; 756; 796; 866; 900	0.06–0.91	[125]
		Acoustic resolution PAFC	680; 850	0.4	[126]
		Custom built system	1060	0.1–0.3	[127]
			680–970 (5 nm intervals)	0.3	[128]
	Mouse (in vivo)	OR & AR-PAM	532	1.03	[129]
		OR-PAM	532	1	[130]
		MSOT	680, 710, 730, 740, 760, 770, 780, 800, 850, and 900	0.5	[131]
		AR-PAM Photoacoustic and hyperspectral dual-modality microscope	1064	0.11	[132]
Epidermal / Skin imaging	Human (in vivo)	AcousticX	400–650 (5 nm intervals)	NA	[133]
		MSOT	850	4	[134]
		MSOT	700; 730; 760; 780; 800; 850; 875	2	[135]
		Raster-scanning optoacoustic mesoscopy	532	0.1	[114,136,137]
		MSOT	680–980	3.4	[138]
Hair follicle	Human (in vivo)	MSOM	460–650	0.1–0.5	[139]
		MSOT	660–1300	0.9	[113]
		AcousticX	690; 850	1.5	[140]

* NA: not available

1450 and 1470 nm, respectively (Fig. 5(ii)). From these serendipitous and disparate peaks, the shifts in their respective amplitudes can be used to determine variations in tissues' water and collagen content across two different wavelength ranges. Yan et al. utilized these optical dynamics to propose an approach for detecting water to collagen ratio in the murine cervix *ex vivo* [157,158]. Their results with corresponding histological analysis demonstrated the procedure's success in accurately determining the collagen to water ratio in the mouse cervixes extracted at half and full-term. Building upon this, Varrey et al. recapitulated Yan et al.'s findings via imaging human volunteer cervical biopsies obtained from both non-pregnant women and those who had just undergone cesarean section delivery [159]. In addition, the water concentration in the tissue was tested and observed using a PA-equipped endoscope by Qu et al. [160]. The hydration level of hydrogel phantoms and cervical tissue of pregnant women was quantified by measuring the PA spectra in the NIR range. According to their study performed in humans, the PA signal (as a proxy for water content) demonstrated a strong correlation with advancing gestational age.

2.4. PA imaging of glucose

Glucose is an intrinsic energy source for all mammals on this planet and is a requisite component for cellular respiration and the synthesis of adenosine triphosphate [161]. Unsurprisingly, human disorders

involving the regulation of glucose pathways constitute a significant burden of disease and cause high morbidity and mortality globally across many diseases [162–165]. The metabolic disorder such as diabetes mellitus interferes with the body's ability to properly regulate blood glucose levels due to the faulty insulin translation or the immunological destruction of insulin-producing beta cells [166]. This affects all organs in the body, as improper glucose levels dysregulate the ability of blood vessels to provide proper nourishment to tissues. Accurate functioning of the regulatory glucose pathways decreases the occurrence of these vascular complications, as noted by the decrease in glomerular permeability and the risk of retinopathy in a two-cohort study by The Diabetes Control and Complications Trial Research Group [167]. However, the incidence of diabetes continues to rise globally, affecting ~422,000,000 people as of 2014. A facile and non-invasive imaging modality is needed to improve both the prognosis and the diagnosis of this disease. Although several non-invasive imaging techniques such as NIR spectroscopy, Raman spectroscopy, optical coherence tomography (OCT), fluorescence detection, and the exciting arena of genetically encoded sensors for a number of metabolic pathways exist for the monitoring of glucose level, PA imaging surpasses either their fidelity, imaging depth, or the need for exogenous contrast agents or genetic manipulation [168–176]. Glucose has been quantified by PA in an aqueous solution via gelatin-based tissue simulations with no noted interference from Sodium chloride, cholesterol, or albumin [177,178].

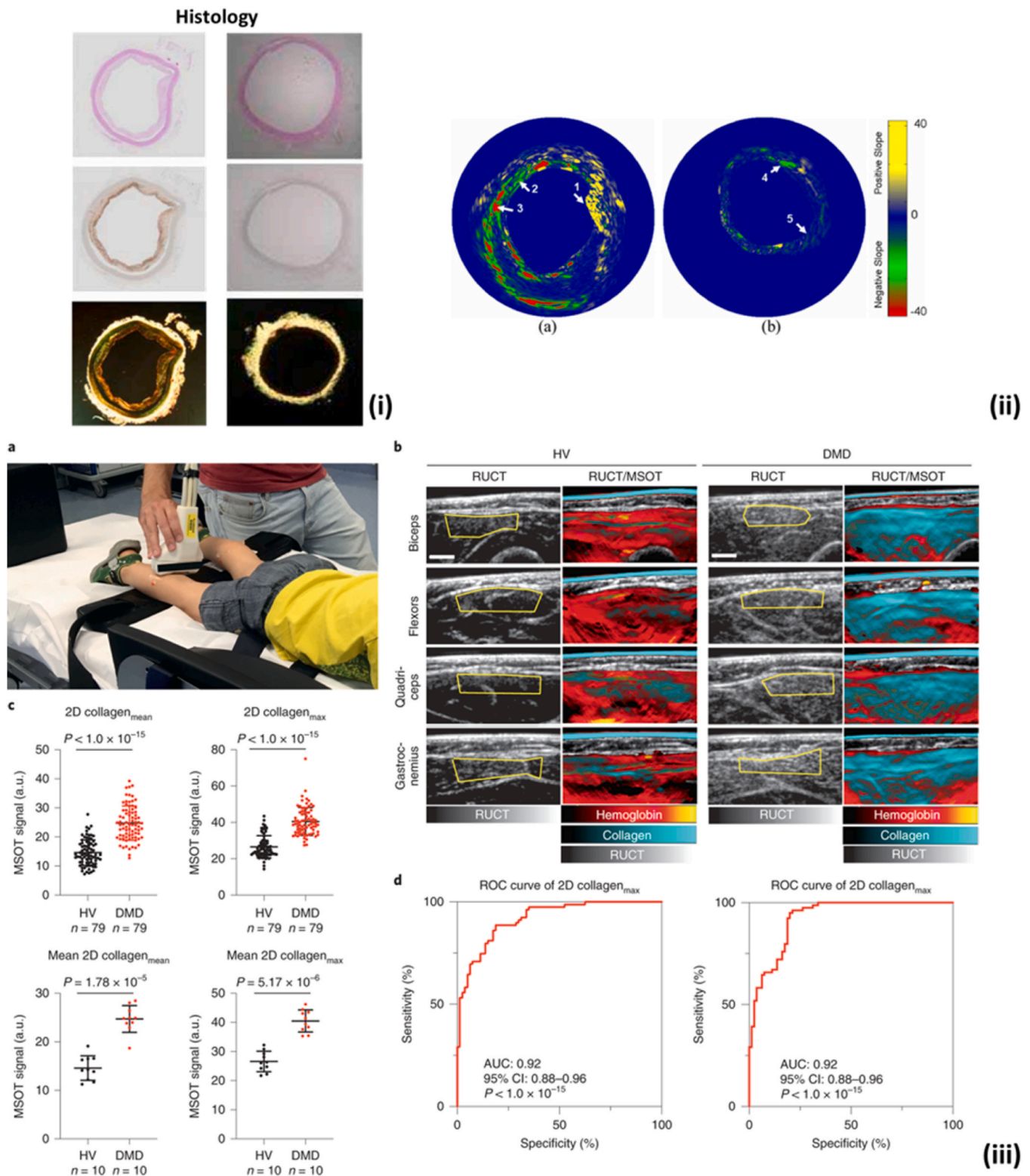


Fig. 4. (i) The histology (hematoxylin and eosin (H&E), RAM11 stain recognizing connective tissue and vascular macrophages, and Picrosirius Red stain for collagen) of two cross-sections of the atherosclerotic (left panel) and normal aorta (right panel). The histology images demonstrate high RAM11 and picrosirius red stain in the presence of plaques in atherosclerotic aorta compared to normal aorta. (ii) The spectroscopic (first derivative) IVPA images. Region 1,2, and 3 in (a) show the suspected region of lipids, collagen type III and collagen type I, respectively. Region 4 and 5 in (b) identify the suspected area of collagen type III. (iii) a. Example of real-time imaging of a 3-year-old healthy volunteer (HV) using the 2D MSOT detector probe. b. Representative MSOT images of transversal scans from four anatomical regions of a 7-year-old HV (left panels) compared to those of a 5-year-old with DMD (right panels). c. Collagen_{mean/max} signals of HV and subjects with DMD, as measured by 2D MSOT. Each filled circle represents one MSOT signal per independent muscle region (upper row) or the mean MSOT signal per independent subject (bottom row). d. Use of ROC curves to distinguish between DMD and HV muscles using unmixed MSOT collagen parameters (collagen_{mean} and collagen_{max}). AUC is indicated with the 95% CI to distinguish between muscles from HV and patients with DMD.

(i, ii) Adapted from [143]. (iii) Adapted from [142].

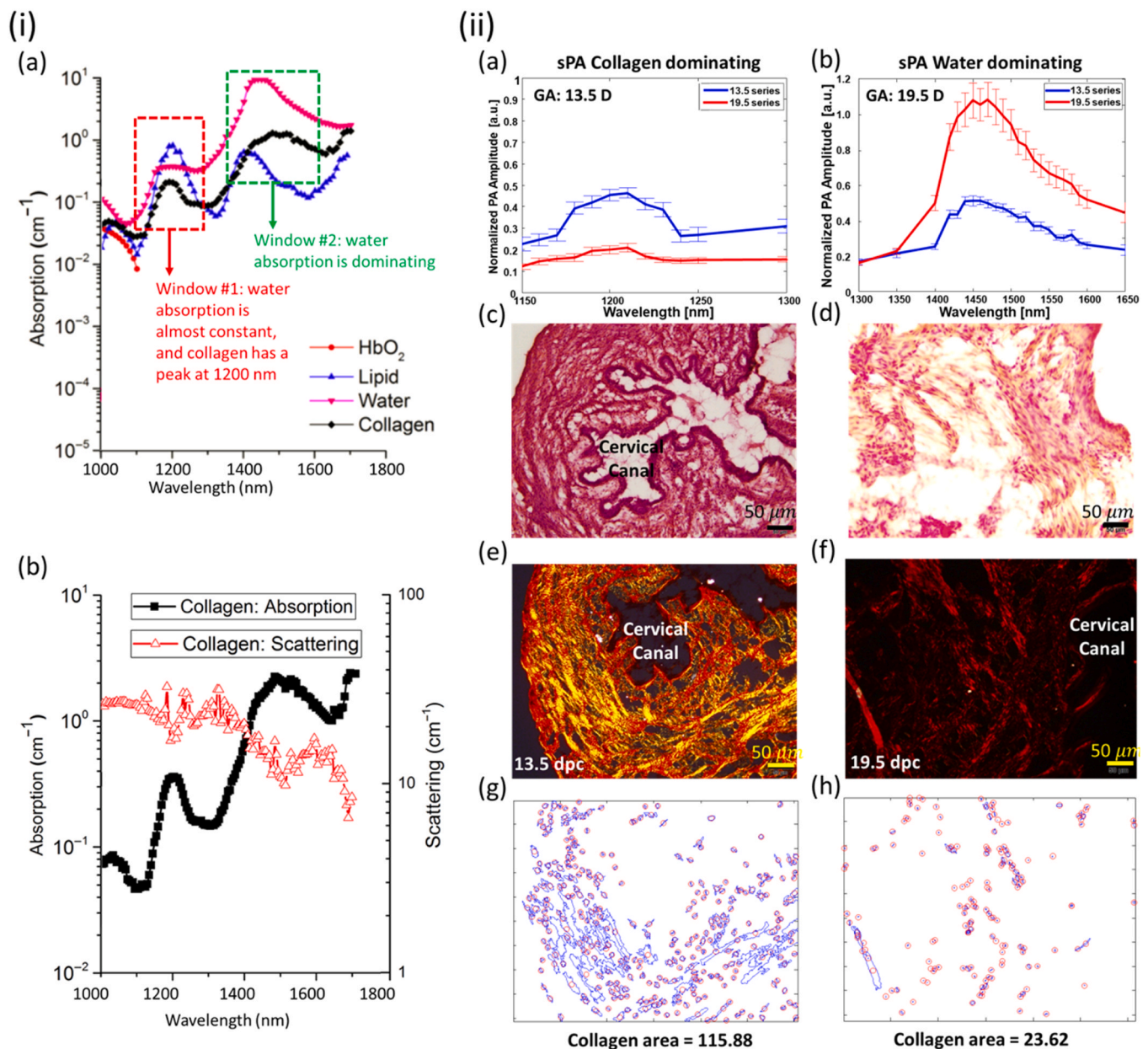


Fig. 5. (i): (a) Simulation of in vivo *optical* absorption spectra of water, collagen, oxyhemoglobin, and lipid in the range of 1000–1800. The red window indicates the area that collagen absorption varies while water is constant. The green Window depicts the region that water is dominant. (b) Collagen (type I) absorption and Scattering. (ii): (a, b): Spectroscopic PA signal amplitudes of murine cervixes at two gestational ages (13.5 and 19.5 dpc, $n = 10$ for each); (c, d): H&E staining; (e, f): Sirius Red staining and polarized light microscopy images of transversal slide of murine cervixes. Position of the cervical canal or lumen is indicated for reference; (g, h): the detected collagen surface-area from histological images. (i) Adapted from [156]. (ii) Adapted from [157].

Several in vivo studies have been carried out to monitor the glucose concentrations through mid-infrared (MIR) photoacoustic spectroscopy of the epidermis [170,171]. However, due to the high absorption of water in the MIR range paired with the shallow penetration depths of MIR light, these wavelengths are impractical for glucose measurement from within deep tissues [179]. To bypass this shortcoming, Kottmann et al. developed an approach utilizing two quantum cascade lasers which provided spectral data from the three absorption peaks of glucose (wavenumbers $k = 1034 \text{ cm}^{-1}$, 1080 cm^{-1} , and 1152 cm^{-1}). Without the use of any complex unmixing algorithms and data analysis, Kottman et al.'s photoacoustic measurements had a high correlation with the glucose values measured using the standard invasive blood glucose meter (coefficient of determination = 0.8) (Fig. 6(i)) [180]. Further improvements in sensitivity could be achieved with use of higher laser

power and more than two quantum cascade lasers for multi-wavelength sensing of glucose content. Measuring glucose content through skin in humans is complex and has high variability to inter and intra subject differences in the skin conditions such as melanin content, water content collagen content etc. Infact, Sim et al. found spatial variability in the glucose absorption due to the activity of sweat glands. In their study, Sim et al., used a raster scanning method to produce maps of spatial variability in the epidermal ridges and glands (sweat or sebaceous glands) [176]. By spatially selecting for regions of minimal interference from these factors, more accurate PA images of glucose were derived with a resolution of $90 \mu\text{m}$. However high-resolution systems such as those utilized by Sim et al. are not capable of real-time measurements. Particularly in this study each measurement required approximately 4.3 minutes after the system was calibrated to each individual user

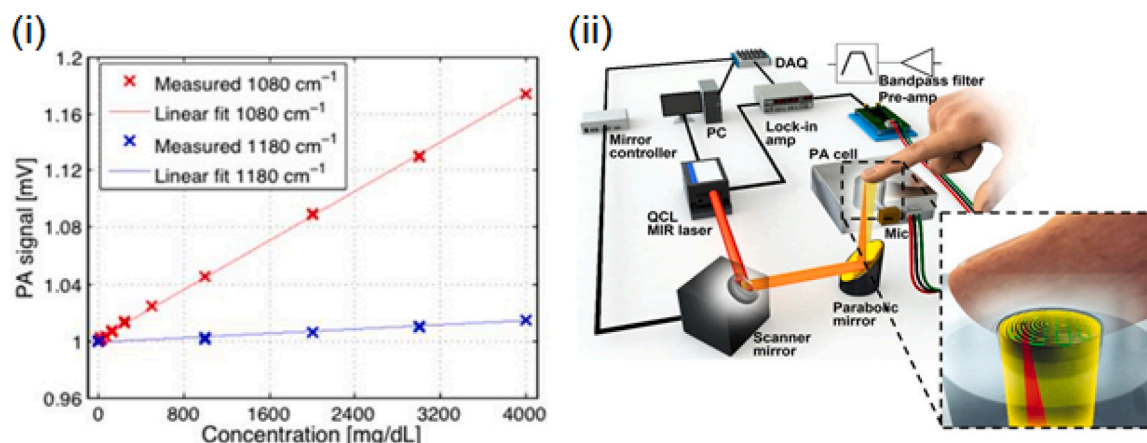


Fig. 6. (i) Relationship between the PA signal and glucose concentration (in mg/dL) in aqueous solutions for two different wavelengths 1080 cm^{-1} (red) and 1180 cm^{-1} (blue). The PA signals were normalized to 1 for pure water. (ii) A schematic of the scanning photoacoustic spectroscopy system for glucose monitoring consists of a two-axis fast steering mirror system, a PA cell, a bandpass filter pre-amplifier, a lock-in amplifier system, and an infrared laser source for illuminating the finger. Microscopic PA images were acquired simultaneously using a stereomicroscope equipped with an interchangeable lens camera. (i) Adapted from [180]. (ii) Adapted from [176].

(Fig. 6(ii)). Technological advances in lasers with high pulse repetition frequency can increase the time resolution of such systems. Sim et al. also suggested that such a technology can also be adapted to forensic sciences [176].

3. PA imaging for guidance of surgical and interventional procedures

Image guidance plays a paramount role in surgeries [181], analogous to navigational technologies employed to guide vehicles through uncharted terrain. Image-guided surgical procedures utilize the demarcation of anatomical features, including vasculature, to minimize collateral tissue damage. The use of image guidance in surgeries also reduces the duration of hospitalization and the probability of additional surgeries being required. Features of US imaging, including its low equipment cost, safety, portability, high spatial resolution, and real-time visualization capabilities, have promoted this technology to be deployed in a number of image-guided surgical settings that include endovenous laser ablation (EVLA) procedures, biopsy acquisition, and neurosurgery [182]. As previously mentioned, artifacts and low contrast in some settings limit the ability of US imaging to provide sufficient image guidance on its own [183–185]. PA imaging has emerged as a novel imaging approach with sufficiently high sensitivity and specificity to overcome the limitations of US imaging while retaining its salient features. We discuss below how PA imaging proves to be more attractive modality than US imaging for guiding surgical tools, placement of implants, tracking temperature fluctuations and lesion formation.

3.1. PA imaging for guiding and tracking biopsy needles

Metallic needles are used to acquire biopsy tissues from several organs, including sentinel lymph nodes, liver, prostate, and breast [186–189]. In a typical biopsy procedure, small tissue samples of a few cubic centimeters are extracted using a US or stereotactic (low dose) X-ray guided needle. US-guided metallic needle placement limitations may include low contrast, transducer-needle misalignment, artifacts produced by angular dependency, comet tail errors, and acoustic clutter [183–185]. Angular dependency is caused when the sound waves echoed from a tissue move away from the US imaging plane and are not received by the US transducer. Examples include the US imaging of tracking fibers in EVLA procedures, in which complications may arise from a failure to detect the fiber tip [183] properly. Comet-tail errors are produced from artifacts generated by a short train of reverberations

caused by an echogenic focus with strong parallel reflectors within it [183,184]. This is particularly important for diagnosing adenomyomatosis (hyperplasia) in the gallbladder, wherein comet tail artifacts may arise from the presence of cholesterol crystals within the hyperplastic tissue [190]. Acoustic clutter involves scattering of soundwaves by multiple tissue layers, which degrade the fidelity of the US waves returning to the detection transducer, thus decreasing the image contrast. This may occur in instances such as US-guided percutaneous liver and kidney biopsies in obese patients. Acoustic clutter requires multiple needle passes to achieve sufficient US contrast for visualization, resulting in greater procedure durations and potentially causing complications [191,192]. Although both US and PA imaging depend on the detection of US waves, PA-induced US wave generation is determined by the wavelength-dependent optical absorption of the imaged region instead of the region echogenic character alone [61]. Though not being endogenous contrasts, metallic needles, as parts of the surgical procedures, absorb light more efficiently than tissues, and thus allow for higher resolution images with high needle-tissue contrast. As such, the omnidirectional acoustic waves traveling from the needle tip provide an angle-independent needle tip tracking, a significant advantage over US needle tracking alone (Fig. 7(a-b)). Recent studies on utilizing PA imaging to track needles are listed in Table 3.

3.2. PA-guided robotic surgical systems

PA imaging systems have been successfully integrated with the da Vinci® robot for guiding a plethora of surgeries, including mastoidectomy and hysterectomy procedures [199,200,217]. In mastoidectomies, infected mastoid air cells are removed using an endoscopic camera and a drilling tool. These surgical techniques utilize an endoscopic camera to visualize superficial anatomical structures and traditional modalities like CT, MRI, and US imaging to guide the endoscope around major nerves and blood vessels. Should image-guidance technologies fail to the point of a critical error, the procedure can cause paralysis or death due to a damage of the facial nerves and arteries. PA-compatible surgical tools can be developed by adding optical fibers to the current surgical tools (Fig. 7(c-f)) to minimize or prevent the occurrence of such pitfalls. In endonasal transsphenoidal surgery, pituitary tumors are removed by drilling through the sphenoid bone under endoscopic guidance. However, the endoscope shows only superficial features and does not provide accurate localization data relative to the drill and bone [201]. Major complications include accidental damage to the carotid artery, which is occluded by the sphenoid bone and may result in thrombus formation,

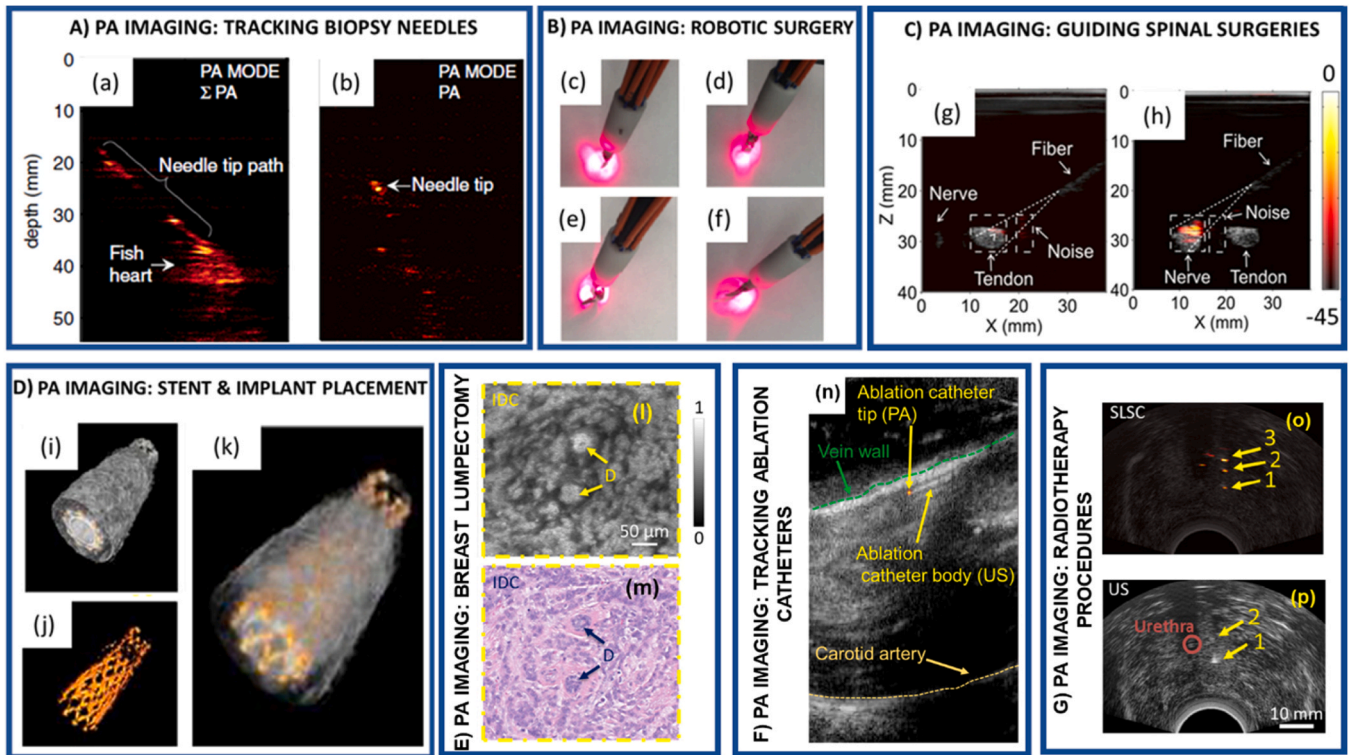


Fig. 7. A) PA imaging for tracking biopsy needles - (a) Sum of all PA frames indicating the path of the biopsy needle. (b) PA imaging tracks the needle tip inside the chicken breast tissue. B) PA imaging for guiding robotic surgeries - (c - f) light profile for scissor tool orientations of the Da Vinci® Surgical system. C) PA imaging for guiding spinal surgeries - differentiate between tendon and nerve samples are shown in (g) and (h), respectively. PA images of this nerve/tendon pair are superimposed on the corresponding US images. A small PA signal from the tendon is indicated with a “V” in (g). The dashed lines are marginal rays that indicate the angular range of light emerging from the fiber. The images (g and (h) were normalized to the maximum value of the image (h), and they are displayed on the same color scale. The color scale indicates the PA amplitude in dB. D) PA imaging for placing stents - 3D reconstruction of the vessel and stent: (i-k) The 3D image was created by acquiring a stack of cross-sectional images and combining them. The ultrasound and photoacoustic signals can be displayed with different transparency in the reconstructed image to show the position and shape of the stent within the vessel. E) PA imaging for guiding breast lumpectomy procedures - Zoomed-in (l) UV-PAM and (m) H&E-stained images of the excised breast tissue indicating two ducts surrounded by invasive ductal carcinoma. F) PA imaging for fiber tip tracking in EVLA procedures - (n) PA imaging accurately tracks the catheter tip within the jugular vein of a canine model. G) PA Imaging for guiding radiotherapy procedures - (o) Postoperative US image of three brachytherapy seeds in a canine prostate and (p) PA images of the seeds acquired after euthanasia. The photoacoustic images were overlaid on the US images and share the same scale indicated in the corresponding curvilinear or linear US image. (A) Adapted from [216]. (B) Adapted from [217]. (C) Adapted from [24]. (D) Adapted from [218]. (E) Adapted from [219]. (F) Adapted from [220]. (G) Adapted from [221].

stroke, and death. PA imaging excels at detecting these critical structures, surpassing CT, US, and MR angiography imaging alone in terms of resolution, applicability to treatments for patients with metallic implants, and safety per PA imaging’s use of non-ionizing laser pulses. During hysterectomy procedures, real-time US imaging fails to distinguish between the ureter and the uterine arteries due to their hypochoic (dense) acoustic character, similar to the NIR fluorescence imaging’s limited tissue penetration at depths greater than a few millimeters. The work of Allard et al. successfully demonstrated PA imaging’s ability to fill this gap by developing a light delivery system surrounding the surgical tool for ureter and uterine artery discrimination at a depth of 10 mm [217]. Additionally, PA imaging has been used for guiding the magnet-assisted microrobots within deep tissues [222].

3.3. PA imaging for image-guided spinal surgeries

PA imaging has also been implemented to enhance image-guided surgical interventions such as vertebroplasty, kyphoplasty and spinal fusion surgery [201,204,223]. In vertebroplasty, bone cement is injected through a hollow needle into a fractured bone to bolster its structural integrity. In kyphoplasty, a balloon is inserted through a hollow needle into a fractured bone, and the area occupied is filled with bone cement upon the balloon’s inflation and removal. Traditionally, fluoroscopy

provides image guidance during these surgeries [224,225]. However, X-ray fluoroscopy utilizes ionizing radiation and fails to visualize the blood vessels and the nerves within the drill path. PA imaging exploits the absorption-based contrast feature of tissues and overcomes this crucial obstacle to visualize blood vessels with sufficiently high resolution and thereby minimizing perforations [61]. sPA imaging at wavelengths around $\lambda = 1210$ nm can show nerves due to their highly absorptive lipid content. Pulsed laser light of wavelengths greater than $\lambda = 900$ nm can be used for visualizing blood vessels (Fig. 7(g-h)). The deployment of two wavelengths in conjunction allows for the guidance of spinal surgery needles with sufficient resolution to avoid critical neuronal and musculoskeletal structures. In spinal fusion surgeries, screws are inserted at the outer layer of the cortical bone pedicle, and then passed through the porous cancellous core and into the vertebral body. Collateral damage to the surrounding tissues in such a procedure may result from the operator’s expertise or images lacking high spatial resolution. As previously mentioned, current imaging modalities, including CT, and fluoroscopy suffer from harmful ionizing radiation. US imaging suffers from angular dependency (which arises from angled positions of the instrument placed within the body) and large acoustic impedance mismatches between bones and soft tissues [223]. Quantitative PA imaging improves spinal fusion surgery imaging fidelity as it can better differentiate cortical and cancellous bone properties as a

Table 3
Selected studies in the last decade that utilized photoacoustic imaging for tracking surgical tools and implants.

Procedure	Model	Imaging Apparatus Central frequency (f_c) or Bandwidth	Imaging wavelength (nm)	Imaging depth (cm)	Reference (s)
PA imaging for the guidance of biopsy needles	Blood vessel mimicking phantom, ex vivo pork joint tissue, in vivo human fingers Human cadaver	AcousticX 7 MHz	850 nm	2.5	[193]
		Custom system 3–8 and 6–13 MHz	-	2	[194]
	Chicken breast phantom, in vivo rats sentinel lymph node Porcine muscle tissue <i>Ex vivo</i>	Custom system 4–7 MHz	695 nm	1.5	[195]
		Custom system 7 MHz	800 nm	~2 cm	[196]
	Various organs and tissues <i>ex vivo</i> Rats sentinel lymph node <i>in vivo</i>	Custom system 5.5 MHz	1064 nm	3	[197]
		Custom system 2.25 MHz	675, 690 nm	1.5	[198]
PA imaging for robotic surgical systems	PVC prostrate and gelatin prostrate phantom	Custom system 10 MHz	532 and 700 nm	-	[199]
		5–9 MHz			
	<i>ex vivo</i> Bovine tissue	Custom system 3–8 MHz	1064 nm	4	[200]
	Bovine bone embedded in a phantom <i>ex vivo</i>	Custom system 5–14 MHz	1064 nm	2	[201]
	<i>in vivo</i> swine model	Custom system 2.5 MHz	750 nm	5	[202]
PA image-guided spinal surgeries	<i>ex vivo</i> sheep vertebrae <i>ex vivo</i> human vertebra	Custom system	532 nm	-	[203]
		Custom system 3–8 and 1–5 MHz	750 nm	5	[204,205]
PA imaging for guiding ablation procedures	Phantom and <i>ex vivo</i> porcine tissue	Custom system 10 MHz	532 nm	-	[206]
		Custom system 5–10 MHz	700–800 nm	2.5	[207]
	<i>ex vivo</i> chicken breast and bovine liver tissue	Custom system 8.5 MHz	680, 700, 760, and 850 nm	3.2	[208]
	<i>ex vivo</i> ox foot	Custom system 4 MHz	700 nm	2	[209]
	<i>in vivo</i> canine tissue	Custom system 10 MHz	532 nm	1.5	[25]
PA imaging for guiding and monitoring radiotherapy procedures	Agar phantom and <i>ex vivo</i> porcine tissue <i>in vivo</i> canine tissue	Custom system 7.5 MHz	800 nm	2	[210]
		Custom system 4–9 MHz	1064 nm	1	[211]
Photoacoustic remote sensing for surgical guidance applications	Brain tissue Breast cancer - Prostate cancer	Custom PARS system	250 & 420 nm	-	[212]
			266 nm	0.005	[213]
			266 nm	-	[214]
Microrobots	Tissue mimicking phantoms	Custom system 11 MHz	680 nm	~2.5	[215]

factor of mineral density and composition [223]. The quantitative information gleaned from the PA imaging help avoid pedicle breaches during screw placement.

3.4. PA imaging for accurate placement of implants and stents

Current dental implant placement pipelines include ionizing imaging modalities such as X-ray and CT to identify the location of teeth, place an implant in the correct location, and measure the fixture's attributes (angle, length etc) [226]. Since these procedures may need to be performed multiple times, radiation can accumulate in the body. It may lead to complications such as cataracts, hair loss, and the onset of leukemia. The work of Lee et al. demonstrated the combination of US and PA imaging for real-time placement of implants and deciphering their attributes under the jawbone, eliminating the need for ionizing imaging techniques for proper implantation [227]. Coronary stents are used for repairing weakened or occluded vasculature. Visualizing the stent pre-and post-surgery requires both the accurate placement of the stent within the vessel and the proper assessment of the stent's residence with respect to plaques and endothelialization into the surrounding vessels. Current imaging procedures like X-ray coronary angiography or fluoroscopy are not ideal candidates for imaging these dynamics due to their ionizing nature. It is worth noting that 2D projections by X-ray

fluoroscopy may lead to the underestimation of lumen diameters and contacts between the stent and vascular epithelium. Other imaging techniques for visualizing stent placement, including MRI, suffer from susceptibility to artifact generation and cannot show the contacts between a stent and a vessel wall. Intravascular ultrasound (IVUS) suffers from low contrast and an inability to resolve stent-epithelium contacts as well [228–230]. Finally, OCT, although capable of generating higher resolution images than PA-US systems, suffers from limited imaging depths of about 2 mm [231,232]. As demonstrated by Su et al. [218], PA-US imaging can visualize the entire cross-section, its thickness variations, and details of the stent's geography with respect to the vascular lumen and epithelium (Fig. 7(i-k)) and therefore making PA imaging an attractive methodology for accurately assessing the placement of stents within the vessels.

3.5. PA-guided breast lumpectomy procedures

Breast-conserving surgery (BCS) involves removing a tumor while minimally excising the surrounding healthy tissue (extent of resection is decided by the negative margins observed in histological evaluation) [233]. To ensure the lowest probability of tumor recurrence, the correct orientation is needed to excise the minimal amount of necessary tissue. The lack of intraoperative assessment tools in this regime makes it

difficult to confirm the complete removal of tumors, which, in turn, opens the door for tumoral regrowth and the necessity of additional surgeries. Cytologic evaluation of whole lumpectomy surfaces using imprint cytology (i.e., a pathological assessment which provides morphological information about the specimen under investigation) is limited by extensive time requirements and the necessity for advanced operator training [234]. Previously, techniques including optical spectroscopy or elastic scattering spectroscopy in the UV wavelength range have been used to characterize the breast tumor margins in the surgical specimens [235]. In addition, Raman spectroscopy has been used for examining the tumor resection cavity [236]. Raman spectroscopy can provide specific information about the molecular and biochemical features of tissues. However, the long duration scan times render it impossible to fit in clinical settings. On the other hand, PA imaging can be acquired instantaneously along with US images. The ability of PA imaging to obtain information on different chromophores in real-time such as nuclei, cytochromes, blood, and lipids at different wavelengths, allows it to be used for visualizing the tumor and non-tumor regions before, during, and following surgical procedures [236–239]. Traditional post-surgical histology examinations by frozen sectioning are limited by the difficulties of freezing adipose-rich tissues and the time required for analyzing large surface areas. Compared to H&E labeling used in histology imaging, PA imaging in the UV wavelength range can resolve individual cell nuclei and provides a contrast level similar to the conventional histological imaging (Fig. 7(l-m)) [219]. Hence, PA imaging facilitates a method for confirming successful tumoral excisions following surgery while being entirely label-free (no use of exogenous contrast agents).

3.6. PA imaging for guiding ablation procedures

In clinical procedures such as EVLA, PA imaging can be used for accurate catheter tip tracking [185]. In EVLA, a US-guided catheter carrying high power continuous wave (CW at $\lambda = 1470$ nm) laser energy is placed inside a diseased artery or vein. The localized heat generated at the catheter tip due to the incident laser light will seal the vascular structure, reducing the probability of thrombus formation, uncontrolled bleeding, or ulcer formation. However, due to US artifacts, including angular dependency (catheter angled out of the US imaging plane) and operator errors including transducer-catheter misalignment, US imaging might lose track of the catheter tip due to reflected echoes moving away from the imaging plane, which ultimately skews US fidelity [182,185,240]. In addition, since the cross-section of the catheter body and the tip has similar echogenic features, it is difficult to distinguish different ablation fibers in transverse US imaging. PA imaging can be integrated with EVLA equipment where the pulsed and CW laser irradiation can be delivered using a dichroic mirror in the same ablation catheter [185,240]. As previously mentioned, PA imaging provides angle-independent, artifact-free, and high contrast images of the catheter tip since the PA signal is generated at the interface between the catheter tip and the surrounding medium. The spherical PA waves traveling omnidirectionally from the tip allow for accurate catheter tip tracking in all orientations. Simultaneously, US imaging produces the anatomical structures of the background tissue and the fiber body. Hence PA imaging combined with the US imaging can provide high contrast in real-time imaging of catheter tips within tissues during EVLA procedures (Fig. 7n) [25,182,185,220,240].

3.7. PA imaging for guiding and monitoring radiotherapy procedures

Brachytherapy is a form of radiation therapy where tumor cells are destroyed through the localized delivery of a radiation dose from radioactive sources placed nearby or within the tumors [241]. Advantages of brachytherapy include minimal exposure to surrounding tissues/organs, localized high dose delivery to tumors, and insensitiveness to organ motion suffered by other radiation-based treatment techniques.

Brachytherapy has been used for treating several types of cancer, ranging from brain tissues to skin tissues [242,243]. However, complications in the existing brachytherapy methods arise due to the migration of brachytherapy seeds, edema, and human error [244–246]. Transrectal ultrasound (TRUS)-guided brachytherapy may fail to properly visualize seeds due to their small sizes and the generation of artifacts reverberating from proximal sources of US reflectance [247,248]. Other forms of non-invasive imaging used to confirm successful seed placements may come at the cost of additional radiation, as in the case with placements done under CT guidance [249]. In lieu of such risky techniques, PA imaging has been able to confirm the accurate placement of cylindrical brachytherapy seeds, without the use of additional radiation sources. The seeds themselves provide strong photoacoustic response compared to surrounding tissue due to the high absorption of light by the seed's metal shell [210,211,221] (Fig. 7(o-p)).

3.8. Photoacoustic remote sensing for surgical-guidance applications

In traditional array transducer based PA imaging system, acoustic coupling of the transducer with water or gel is required for propagation of photoacoustic waves from the tissue to the transducer. Creating a sterile non-contact imaging environment for surgical samples becomes a challenge when acoustic coupling is a requirement. Recently, a non-contact photoacoustic remote sensing (PARS) microscopy method was introduced by Hajireza et al. [250,251] where a nanosecond excitation beam is co-focused with a CW probe beam and irradiated onto the target tissue. The intensity of the back-reflected “interrogation” probe beam is dependent on the optical properties of the tissue. Utilizing the UV absorption peak of DNA and other cellular chromophores, i.e., without any exogenous contrast agents and extensive sample preparation, PARS system generated “virtual” histology of the samples. The technique also achieved high signal-to-noise ratio (SNR) (40–50 dB) with minimal pulse energy of ~ 40 –60 nJ. Through mechanical scanning, a 3D visualization of subsurface nuclear morphology in resected tissues was also possible enabling the “on-site” evaluation of surgically resected tissues. Currently, the imaging speed for larger tissues is low, and the footprint of the imaging head is incompatible for clinical translation. Despite these challenges, the present results indicate a significant promise for these non-contact technologies, particularly for obtaining information on the tissues *in situ* in an operating room.

4. PA imaging for real-time thermometry and assessment of lesion formation

4.1. PA imaging for real-time temperature monitoring in therapies

PA imaging exploits the dependence of the Grüneisen coefficient, a measure of the efficient conversion of heat energy to pressure, for non-invasively monitoring the real-time temperature changes in tissues [61]. The PA signal is defined by: $P = \Gamma(T)\mu_a F = \frac{\beta c^2}{C_p}(T)\mu_a F$, where the Grüneisen parameter (Γ) is a dimensionless value representing the thermoelastic expansion efficiency of the medium. The term μ_a refers to the optical absorption coefficient of the target tissue (cm^{-1}). F is the local light fluence (J/cm^2). The Grüneisen parameter is a temperature-dependent multicomponent factor which is constituted by the thermal coefficient of volume expansion (β), speed of sound (c), and the heat capacity at constant pressure (C_p) [61]. The ability to monitor the temperature in real-time is derived from the principle that the changes in the surrounding temperature cause changes in the amplitude of the PA signal. This relationship is formulated by: $\Delta T = a \frac{\Delta P}{P}$, where $\Delta P/P$ refers to the relative amplitude of the PA signal, a refers to the temperature-dependent constant, and ΔT refers to the temperature change of the surrounding medium. These features allow PA imaging to be utilized as a non-invasive temperature feedback sensor in many thermal therapies listed below.

During thermal therapies, the heat caused by the ablation laser raises the tissue temperature to exceed beyond 50 °C [252–255], which induces denaturation, coagulation followed by tissue carbonization. These denaturing and coagulation phenomena alter the optical absorption properties of tissue chromophores μ_a . As PA imaging primarily depends on μ_a , PA thermometry procedures to monitor the tissue temperature are limited to certain threshold temperatures below 50 °C. However, a recent study has validated the ability of PA imaging to monitor the real-time tissue temperature variations beyond the coagulation temperature (≤ 90 °C) [25]. These studies utilize internal illumination-based PA imaging, where the laser fluence can be considered constant and compensated for the temperature-dependent optical properties of chromophores including blood and water at higher temperatures. Other tissue chromophores including fat can also be studied using this technique. In case of external illumination PA thermometry, the need for accurate fluence estimation causes further challenge for quantitative temperature measurement. Despite these challenges, efforts are being made to estimate the fluence through the tissue using light diffusion modeling. A thermal-energy-memory-based PA-based thermometry technique overcomes these challenges and provides direct monitoring of the absolute temperature of the tissue [256]. Overall, current PA imaging techniques utilizing external illumination

procedures suffer from these limitations, and quantitative thermometry is limited to a certain temperature range, often not exceeding 50 °C. The temperature is computed by estimating the Gruneisen parameter through a self-normalized ratio-metric measurement which eliminates temperature-irrelevant quantities including the optical properties of tissues.

4.1.1. PA imaging for in vivo temperature monitoring during cryotherapy

Cryotherapy is a minimally invasive technique that utilizes localized freezing for tissue destruction, and reduces irritation and inflammation caused by entrapped nerves. In addition to treating nerve-related issues, cryotherapy can also treat other diseases such as atopic dermatitis and prostate cancer [257–259]. In cryotherapy-based prostate cancer treatments, TRUS-guided cryoprobes consisting of pressurized argon gas (cooled below -100 °C) are placed inside a tissue [260]. Due to the Joule-Thomson effect, the tissues surrounding the cryoprobe are frozen in a localized fashion based on the concentration and pressure of argon and/or helium in the treated region. Freezing and thawing cycles are controlled by thermal needle sensors placed near the targeted region, be it a lesion, the urethra, or rectal wall. The first freezing cycle is activated via expanding argon/helium until the temperature of the lesion reaches a lethal value. Repeated compression-decompressions of the gas in use

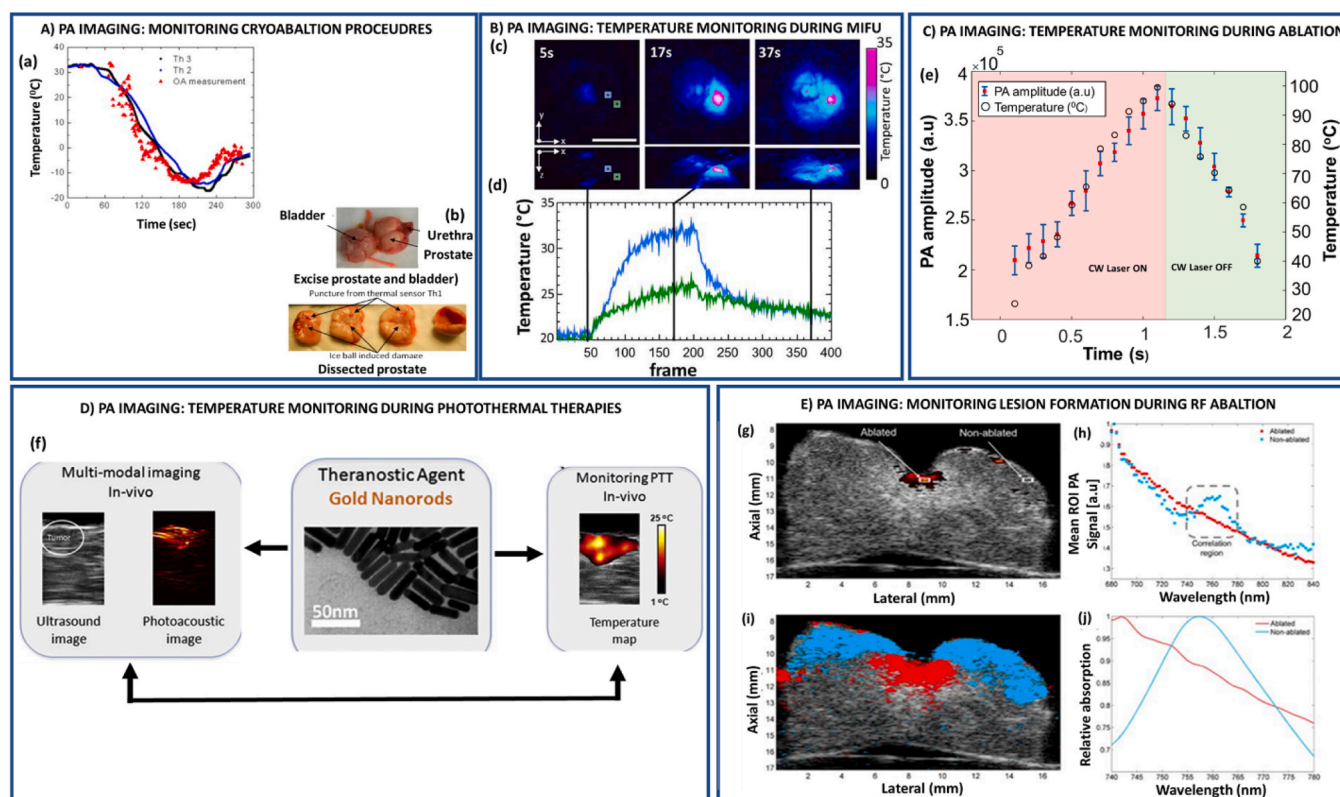


Fig. 8. A) PA imaging to monitor temperature during in vivo cryotherapy procedures - (a) The temporal temperature profile reconstructed for the high contrast object (blood vessel inside the ROI); for comparison, the temporal logged by the nearby thermal sensors are shown by the black and blue solid lines. (b) The prostate of the dog was excised and dissected following the cryotherapy to show transverse sections across the urethra demonstrating damage induced by the freezing B) Volumetric optoacoustic monitoring of temperature during MIFU therapy - (c) Transverse and lateral MIPs of the reconstructed optoacoustic volumes at different points during the procedure. (d) Time corresponding to the different treatment phases, being 5 s before the MIFU system was switched ON, 17 s at the maximum heating stage and 37 s at the post-treatment thermal expansion period. C) PA imaging for monitoring temperature during EVLA procedures - (e) plot indicating the variations in PA amplitude with changes in temperature caused by the CW laser carried by the catheter placed within the jugular vein of a canine model. D) PA imaging for monitoring temperature during PTT - (f) Gold nanorods, a theranostic agent, used for combined US and PA imaging and PTT. US and PA images of the mouse tumor injected with gold nanorods. The tumor region is shown in a white inset in the ultrasound image. The PA image shows higher contrast in the tumor area due to the accumulation of gold nanorods. Thermal image of a subcutaneous tumor in nude mouse. During the PTT procedure, approximately 25 °C temperature rise was observed in the tumor. E) PA imaging for monitoring lesion formation during RFA ablation - (g) Single wavelength PA image (710 nm) overlaying US image with ablated and non-ablated ROI's. (h) Mean ROI photoacoustic signal plotted vs. wavelength. (i) Tissue characterization map. (j) Reference spectra for ablated (averaged over eight samples from two hearts) and non-ablated (derived from optical extinction data from deoxyhemoglobin) tissue.

(A) Adapted from [264]. (B) Adapted from [265]. (C) Adapted from [240]. (D) Adapted from [266]. (E) Adapted from [267]. (C) Adapted from .

allow for repeated freezing cycles, which can be tuned to the desired level of tissue destruction. In rectal applications, the performance of cryotherapy depends on the temperature of the surrounding tissues and the formation of an ice ball proximal to the rectal wall [261]. Current imaging procedures, like TRUS, can partially estimate the damage caused by the ice ball to the surrounding tissues. However, it does not depict the entire boundary of the ice ball at temperatures around 20 °C [262]. PAT has been successfully implemented for monitoring the real-time temperatures of cryotherapy procedures by integrating a fiberoptic bundle coupled to a pulsed laser operating at 805 nm wavelength range (Fig. 8(a-b)). Since the amplitude of the PA signal increases with the surrounding temperature [240], the amplitude of a PA signal can be used as a proxy for monitoring the temperature of tissues during cryotherapy procedures. In addition, highly optically absorptive properties may themselves act as a temperature sensor [263]. This provides a similar PA signal response in all types of vascularized tissues regardless of the surrounding tissue composition, bestowing the ability to generate temperature maps of vascular regions for therapeutic surveillance [259].

4.1.2. PA imaging for monitoring tissue temperature during high and medium intensity focused ultrasound therapy

Therapeutic US has been used to treat maladies, including tumors, kidney stones, injured muscles, and neurological disorders [268,269]. High-intensity ultrasound waves delivered from the focal region of a high-intensity focused ultrasound (HIFU) transducer are subsequently absorbed by the soft tissues in the target area. The absorption of HIFU energy induces a rapid increase in temperature, courtesy of vibration-induced friction leading to tissue coagulation, and may cause a cell to undergo irreversible commitment to self-destruction in addition to damaging tumor-feeding blood vessels [270]. The effectiveness of HIFU treatments depends on proper monitoring and the composition of the treated tissue, and thus its subsequent acoustic properties. Current imaging modalities like MRI are limited by high cost, while US imaging is limited by low native imaging contrast, sensitivity, and resolution [271–273]. Once again, PA imaging demonstrates its usefulness in this application as it provides high optical contrast in deep regions (up to 5 cm) within the body. Cui et al. successfully implemented a PA microscopy system equipped with a HIFU module to demonstrate HIFU's ability to destroy tissue; in their case of swine liver embedded within chicken breast tissue, showing both the magnitude of the destructive HIFU effect on a human organ proxy and PA imaging's ability to successfully track it [274]. In addition to HIFU, medium-intensity focused ultrasound (MIFU) has acoustic intensity levels ranging between echography and HIFU (5–300 W/cm²) [265]. Like HIFU, MIFU can be used to induce thermal effects in soft tissues during physiotherapy and cancer therapy procedures, adding another tool to the US treatment arsenal depending on the tissues in need of treatment at different penetration depths [275]. Treatment outcomes from MIFU rely heavily on temperature monitoring and the duration of the exposure. Forfeiture of either parameters may result in the unintended destruction of non-target tissues or the undertreatment of the target zone. The work of Landa et al. demonstrated that four-dimensional (4D) PAT could accurately monitor and provide real-time feedback about the temperature changes during tissue heating in MIFU procedures via the generation of 3D maps of local tissue temperatures at various time points, allowing for the acquisition of highly spatially specific temperature changes that may have otherwise been overlooked using traditional 2-dimensional images (Fig. 8(c-d)) [265]. 4D PAT provides effective control of the targeted tissue's exposure time and prevents overheating the tissue beyond safe levels. PA-based temperature mapping was performed due to the dependence of the temperature-dependent Grüneisen parameter. The temperature distribution was estimated based on the Grüneisen parameter of water since tissues used in the experiment contained 75% water. However, accurate calibration *in vivo* is challenging as precise temperature calibration depends on the fluence estimation and the

varying optical properties of tissue chromophores, which change at higher temperatures.

4.1.3. PA imaging for real-time temperature monitoring in EVLA procedures

Current EVLA procedures cannot visualize changes in temperature while underway, as most EVLA procedures rely upon US imaging alone as the chosen method of image guidance. The lack of temperature monitoring reduces therapeutic precision and efficacy. It may also result in damage to perivenous tissues could cause endovenous heat-induced thrombosis formation and unnecessary pain and discomfort for the patient [276,277]. By exploiting the amplitude of PA signals and its proportionality to the surrounding temperature, PA imaging can be used to monitor temperatures at the fiber tip in real-time [25], as demonstrated by John et al. within the jugular vein of a canine model [220] (Fig. 8(e)). As previously mentioned, PA imaging procedures need an accurate laser fluence estimation at the target location to ensure the accuracy of both the US signal generation and the temperature within the target area. Estimating the delivered laser fluence in external illumination scenarios is difficult due to the complex light diffusion, absorption, and reflective dynamics that heterogeneous tissues exhibit. However, by utilizing internal illumination techniques, light fluence remains constant because the PA signal is generated at the interface, where light interacts with the surrounding medium immediately, removing the confounding influence of signal distortion as it travels through heterogeneous tissues. Hence, PA imaging utilizing internal illumination faces fewer challenges in providing accurate temperature monitoring within the vasculature.

4.1.4. PA imaging for monitoring the temperature of the fundus of the eye during laser irradiation

Light and heat-based therapies such as CW photocoagulation, PDT, and transpupillary thermotherapy offer a wide array of options for treating diseases of the retina [278,279]. The effectiveness of procedures that rely on temperature changes as a basis for therapeutic action requires non-invasive monitoring of the temperature of retina to prevent damage in regions outside of the target area. In photocoagulation, heating of the retinal tissue causes denaturation of proteins when local temperatures increase above 65 °C [254]. The work of Schüle et al. demonstrated the successful non-invasive monitoring of the increase in tissue temperature using a neodymium-doped yttrium lithium fluoride laser of wavelength $\lambda = 527$ nm and 500 Hz pulse repetition frequency (PRF) in both porcine cells and the eyes of living humans. The system was capable of detecting temperature fluctuations as small as 1 °C [280]. By deploying a unique contact lens to immobilize the eye and limit refraction, they were able to tune the frequency of pulsed laser energy, enabling precise control over local temperature increments. These measurements were essential to avoid the destruction of the neuron and photoreceptor populations within the target window. Such a precisely controlled thermal therapy will pave the way for future advancements and accurate personalized treatment of eye-related maladies.

4.1.5. PA imaging for monitoring temperature in photothermal therapies

PTT is a minimally invasive procedure used to treat a multitude of cancers, including those of head, neck, liver, skin, breast, bladder, and cervix [281]. PTT involves deploying light-absorbing dye or nanoparticles, which can convert electromagnetic radiation into cytotoxic heat upon stimulation. As with numerous other light-based therapies, temperature monitoring during PTT plays a critical role in determining its efficacy. Photothermal cancer treatment is performed by selectively heating a small number of cancer cells, which induces apoptosis, necrosis, or necroptosis in a sufficiently precise fashion to target lesions proximal to vital organs [282]. Tumor-targeting photoabsorbers such as gold nanoparticles [266] or dyes are irradiated with a high-intensity CW laser at the NIR spectrum to generate the cytotoxic heat (Fig. 8(f)). The efficiency of the treatment is dependent on the localization and accumulation of photoabsorbers at the tumor site [281], along with the

successful monitoring of the temperature increase to achieve cell death (42–60 °C) [255]. It should be noted that a cell is far more sensitive to the increase in the internal temperature relative to external surrounding, and the internalization of a photoabsorber by a cell increases the speed at which the death pathways may be activated [282–285]. Current imaging modalities like MRI and US imaging, though used for monitoring changes in tissue temperature, suffer from motion artifacts and low acoustic contrast during PTT [286–288]. The advantage of using PA imaging for monitoring PTT is two-fold. First, PA imaging can be used to locate tumors deeply embedded within the organs [61,281]. For example, PA imaging has been used to determine the location of tumors during PTT of liver cancer (Hepatocellular carcinoma) [289] and breast cancer [290]. Furthermore, the photoabsorbers used for PTT can also improve the contrast of the cancerous lesions in PA imaging when illuminated with a laser tuned to the wavelength specific to the photoabsorbers. Secondly, the PA signal is highly sensitive to the change in temperature compared to ultrasound waves due to the dependence of both the volume expansion coefficient and the speed of sound on temperature. More recently, numerical studies performed on realistic phantoms (such as the mouse head with glioblastoma tumor [39,55,291]) reveal the complexities involved in PTT dose with and without the use of nanoparticle systems. Such mathematical models can advance the utility of personalized PTT for patients together with progress in PA imaging and developments in nanotechnology.

4.2. PA imaging for real-time assessment of lesion formation during ablation procedures

The optical properties of the tissue change during the thermal ablation procedures such as laser and radiofrequency ablation (RFA). Since PA imaging is sensitive to detecting a contrast in optical absorption of tissues, it can be a suitable platform for non-invasive monitoring of lesion formation and tissue characterization.

4.2.1. PA imaging for real-time assessment of lesion formation in cardiac ablation procedures

The temperature monitoring capability of PA imaging has been successfully implemented in RFA, also termed electrosurgery. Electrosurgery involves alternating RFA current for the destruction of diseased tissues. Electrosurgery is often deployed in dermatology, oncology, and cardiology to treat cardiac arrhythmias [292,293]. Successful surgeries depend on the precision of catheter guidance and the correct evaluation of the desired clinical endpoint, whether it be the destruction of part of a cardiac-neuronal circuit or its stimulation and restoration to a prior firing pattern. Of the imaging techniques used to monitor surgical success, IVUS imaging fails to visualize lesion formations accurately due to limited contrast [294]. MRI is limited by high costs and the requirement of exogenous contrast agents (gadolinium), and infrared thermal imaging is restricted to superficial layers. OCT allows for monitoring tissue temperatures but cannot provide data on the formation of lesions. Under external illumination of $\lambda = 780$ nm, PAT has been demonstrated to evaluate the formation of lesions in real-time following ablation procedures, owing to the boost in PA signal generated from coagulated tissues [295]. Atrial fibrillation is a cardiac arrhythmia resulting from aberrant electrical activation patterns originating from the atrial wall rather than the sino-atrial node. Alternating RFA may resolve or diminish these misregulated neuronal firings by causing tissue necrosis via heat generated by the movement of ionic cellular components in response to the radiofrequency current. Imaging methods including OCT, NIR spectroscopy, and auto-fluorescence hyperspectral imaging lack reliable information regarding lesion formation in terms of depth. In contrast, US imaging may struggle to demarcate tissue borders in echogenic heterogeneous regions [296–301]. The curvature of the atrial wall also makes it difficult to align a US beam relative to the lesion site properly. Single-wavelength PA imaging accurately visualizes the center of a lesion but cannot completely distinguish between ablated and

non-ablated tissues (myocardium tissue) [302]. To this end, by exploiting PA signal-absorption coefficient dependency, sPA imaging in the wavelength range of 740–780 nm was performed by Dana et al. [267] to successfully differentiate ablated and non-ablated tissues in excised porcine ventricles (Fig. 8(g–j)). The PA signal strength from the ablated region decreased at a certain wavelength (near $\lambda = 760$ nm) and exhibited a peak corresponding to the non-ablated area. The peak in the PA signal was due to the absorption of deoxyhemoglobin, which is a strong absorber in harvested, oxygen-depleted tissues. Additionally, other sPA imaging studies of the heart performed by Iskander-Rizk et al. utilized wavelengths 790 nm and 930 nm for detecting lesions with a diagnostic accuracy of 97% [303]. Recent studies developed a PA-US theranostic endoscope that provides simultaneous imaging and therapy. In contrast to poor images provided by traditional ablation endoscopes [304,305], their theranostic endoscope provided high-contrast functional and anatomical information about the target tissue. The unique size of the endoscope allows it to be used in a variety of clinical applications [306–308]. Further, the endoscope was even able to distinguish between different tissue types and confirmed the extent of tissue ablation using tissue correlation maps. The tissue-temperature monitoring capability allowed the system to minimize complications and enhanced laser ablation assisted atrial fibrillation procedures.

4.2.2. PA imaging for real-time assessment of lesion formation in liver ablation procedures

Percutaneous RFA is a localized treatment for tumors in several organs including liver, and it provides a minimally invasive method for destroying nerves [309]. RFA involves applying heat to a target tissue, generated through alternating current carried by the needle-based electrode and surface-based ground pads. Currently, this procedure is limited due to difficulties in monitoring the precise position of the electrodes, which may lead to the recurrence of tumors, missing a target nerve in need of destruction, or causing the destruction of off-target tissues [310]. The need for contrast agents and the ionizing radiation generated in CT imaging curbed its widespread deployment [311]. The lack of real-time monitoring capabilities limits the utility of MRI imaging in guiding RFA procedures. Similar to the PA imaging of biopsy needles as described in previous section, several artifacts are also present when visualizing electrodes in US imaging [183,240,312]. In addition, larger tumors confound the ability of US imaging to estimate the amount of ablation that has taken place as a factor of tumoral heterogeneity, and the US imaging may be unable to distinguish proximal vasculature, which may act as a heat sink and lessens the degree of tissue ablation [313]. As PA imaging exploits the optical absorption properties of Hb and HbO₂ to visualize blood vessels and detect lesion formation based on changes in tissue absorbance, its integration with RFA procedures will undoubtedly improve gauging therapeutic efficacy [61,314]. The ablation monitoring capabilities of PA imaging were demonstrated and validated in *ex vivo* bovine liver samples [309,312]. PA imaging of the ablated tissue revealed a decrease in the PA signal intensity due to the reduction in the optical absorption properties and increased scattering of ablated tissues.

4.3. PA imaging for monitoring therapy-induced changes in vasculature and oxygenation in non-oncological applications

As previously mentioned, PA imaging is a facile and low-impact method of imaging several functional systems in the body. One of the PA imaging's most salient features is its ability to glean oxygenation dynamics, an important parameter pertaining to nearly every malady of the human body [22,315]. Although limited to diffusion and absorption-based metric as a function of imaging depth, PA imaging can be used non-endoscopically up to a depth of few centimeters depending on the illumination wavelength. This makes it easily integrable for monitoring various therapies including those in non-oncological malignancies such as stroke, aberrant vascular network junctions (termed

anastomoses) in the developing embryo, and rheumatoid arthritis.

4.3.1. Detection of strokes using PA imaging

Ischemic or hemorrhagic strokes account for ~10% of human deaths globally and are exceptionally difficult to predict [316]. Rapid treatment is of paramount importance to minimize cell death from oxygen deprivation, and the progress of either oxygen deprivation or restoration

following the treatment may be monitored using PA imaging. The work of Deng et. al. demonstrated the successful deployment of PA imaging for observing strokes in mice to this end, illustrating marked changes in blood volume and flow when paired with laser speckle imaging [317]. In their experiments, ischemia was induced surgically. It showed a drop of blood flow in arteries down to 34.13% of nominal at 60 minutes post-ischemia point and a further decrease in blood volume down to

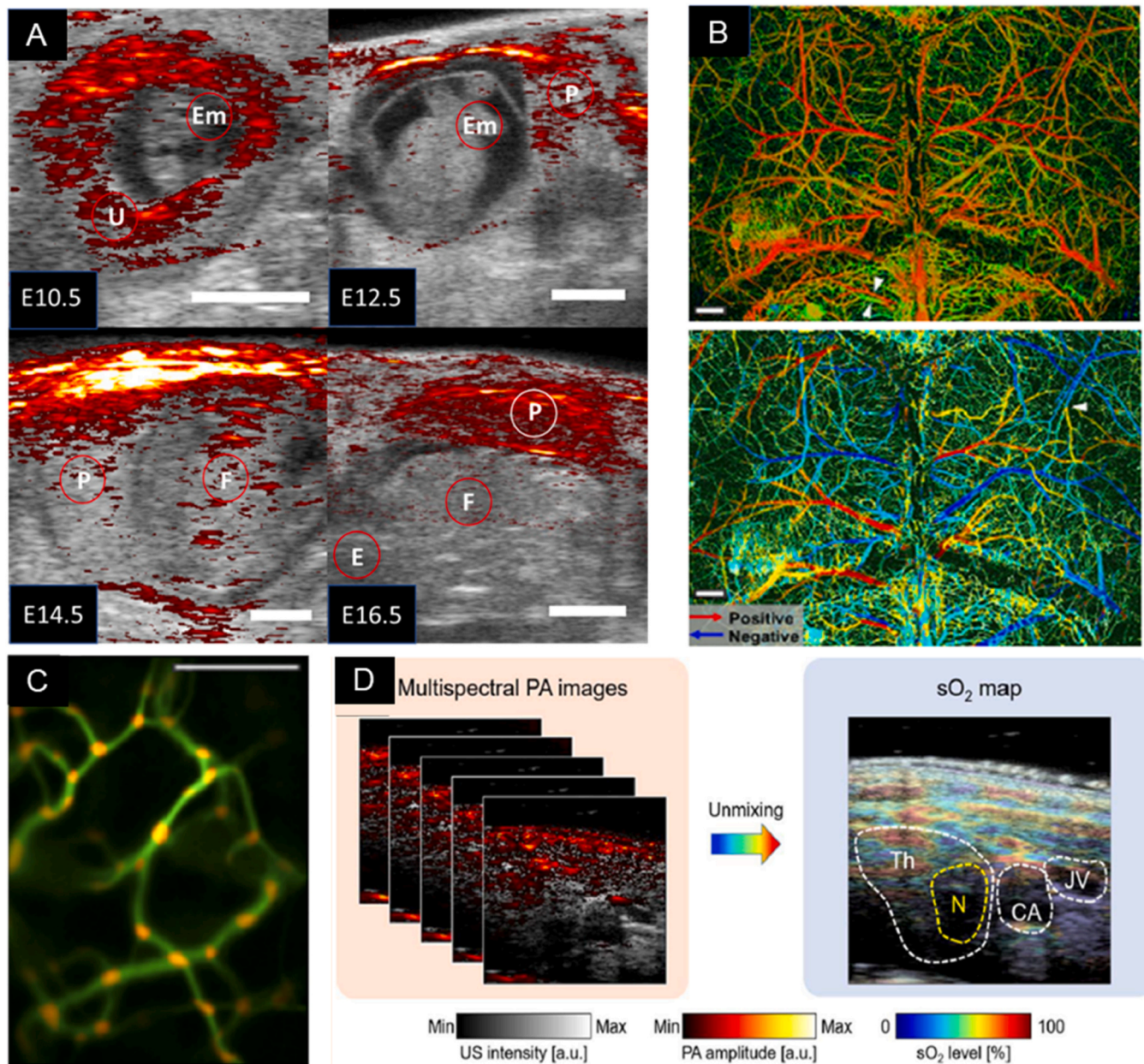


Fig. 9. (a) PA imaging overlaid on US background to demarcate regions of oxygenation of the developing mouse at various developmental points under 810 nm light and US transduction of 40 MHz. PA imaging intensity displayed in the strength of the PA signal breached the median value. Otherwise, the US image is presented alone. Scale bar = 200 μ m, embryo (Em), fetus (F), placenta (P), and uterus (U) demarcated. (b) PA imaging for the detection of strokes. SO₂ content (above) and blood flow direction (below) as extracted by PA imaging of the intact mouse skull. Imaging depth reached 400 μ m without losing resolution of fine vascular processes as denoted by the white arrows highlighting a proximal arteriole and venule. pO₂ map coded as higher (red) and lower (green) values, extracted from $\lambda = 532$ and $\lambda = 559$ nm laser illumination. Blood flow direction was mapped by contrasting forward and backward B-scans and the Doppler shifts of RBCs to infer their direction of movement. A white arrow denotes arteriole. Scale bar = 500 μ m. (c) PA imaging for the detection of strokes. ViTuBi map of bifurcation events in mouse ear vasculature. Generated by a composite of PA images from $\lambda = 415$ nm illumination and applying a filter that bins the likelihood of a bifurcation based on vascular convolution (or decreased RBC speed). Orange regions correlate to the emergence of a bifurcation toward the screen on the z-axis of the image. Scale bar = 50 μ m. (d) PA imaging for cancer detection and staging. Composite sO₂ map of thyroid region of a human patient with a malignant tumor, generated from spectral unmixing of z-stacked US and PA images from $\lambda = 700, 756, 796, 866,$ and 900 nm illumination. The tumor nodule exhibits decreased oxygen perfusion relative to the thyroid, and excision-critical features as the carotid artery and jugular vein can be easily identified. Th = thyroid, N = tumor nodule, CA = carotid artery, JV = jugular vein. (A) Adapted from [322]. (B) Adapted from [320]. (C) Adapted from [323]. (D) Adapted from [41].

74.63% of nominal 1-hour after ischemia was induced. The drop in blood flow was continued as the sampling time post-ischemia increased. It should be noted that their imaging began 15 minutes after the induction of ischemia, a critical window in humans to avoid damage to the brain [318]. Another important aspect to consider from Deng et al.'s work was that of the blood flow rates. Although blood flow rates starkly decreased at all time points, blood volume increased within 20-minutes post-ischemia. This compensatory process is regulated by the body and must be understood to avoid skewing blood-related data and stroke prognoses during clinical assessments. In addition, variability between arteries and veins blood flow and volume was another essential consideration that may lead to under- or over-estimating the impact of a cranial infarct. Addressing the highly time-sensitive nature of stroke diagnosis and treatment, Lv et al. developed a PA imaging system that was able to detect an infarct 5 minutes after onset; however, exogenous contrast agents were necessary [78]. As imaging technologies improve, the features such as high-resolution vascular maps deeper within the brain using PA will follow suit.

Great strides in the study of vascular structures following stroke were possible due to non-invasive PA imaging. For example, in the study by Hu et al., the vasculature and pO_2 content of the mouse cranium following cerebral artery occlusion-induced stroke was monitored using PA imaging at 563 and 570 nm [319]. Their work demonstrated that microvasculature, although absent from vascular images 60-minutes post-occlusion, re-perfused following the release of the cerebral artery occlusion. They also showed that arterial sO_2 returned to normal, and venous sO_2 values increased to nearly arterial levels. These findings serve as an excellent model upon which to base human stroke dynamics and have the potential to offer an avenue of improving treatments by establishing a standard perfusion and sO_2 model of re-oxygenation patterns. Another study by Ning et al. showed that the potential of PA imaging to image vascular structures, pO_2 values, and blood flow rates through the intact mouse skull at a depth of 400 μm (Fig. 9(b)) [320]. By implementing algorithm-controlled dynamic focal plane adjustments paired with the simultaneous US and PA imaging, the data on functional dynamics in the parietal and temporal cortices were deciphered. This setup, although covering only a small portion of the total brain vasculature, will be of great utility in the study of more superficial vasculature and neuronal cell types affected by stroke. The pairing of Ning et al.'s work with future developments in endoscopic imaging will undoubtedly pay dividends in the study of deeper vascular regions of the brain and may also be combined with a multitude of genetically encoded neuronal signaling sensors to understand brain physiology under the lens of disease progression and recovery at an unprecedented scale [321]. These advances in PA imaging along with parallel computing would be critical for establishing normative models to decipher stroke and other human brain functions [39].

Another important facet of treating strokes and other maladies which affect vasculature is the dynamics of angiogenesis following an infarct or other sources of vascular challenge. Novel bifurcations of vasculature indicate network re-arrangement and/or angiogenesis events and B. van der Sanden et al. have produced a tool for effectively characterizing these bifurcations *in vivo* [323]. Their tool termed Virtual Tubes out of Bifurcations, or ViTuBi, is an algorithm-based method of bifurcation detection that relies on applying a filter to z-stacked PA images of the vasculature to determine the probability that a bifurcation is present (Fig. 9(c)). Said filter makes these determinations as a product of vascular complexity, determined by comparing 8 PA image-stacks at a time against the averages of 50. If RBC movement is above the threshold of the binning algorithm, a bifurcation extending out of the imaging plane along the z-axis is proposed to exist. Van der Sanden et al. proposed ViTuBi to be more sensitive than previous bifurcation predicting algorithm-based methods such as Angiotool [324]. However, they warn that ViTuBi may overestimate bifurcation events, as the algorithm might bin vasculature that is not parallel to the imaging plane or exhibits high directional or diametric complexity. The authors intend to deploy this

technique for the study of tumor angiogenesis, but its deployment for the study of post-infarct angiogenesis in the brain may also prove extremely useful for diagnostics and therapeutic planning. It should be noted that the brain is not composed of only neurons and vasculature, but a wide range of cell types including non-neuronal varieties. As greater understanding of these systems come to light, their pairings with the study and development of the future PA imaging systems will propel the field of stroke-related medicine and neuroscience forward.

4.3.2. PA-guided functional Imaging of the placenta

On the opposite end of the spectrum from treating maladies that arise in fully developed humans, PA imaging has been implemented to study and treat maladies pertaining to fetal development, most notably the oxygenation dynamics of the placenta (Fig. 9a) [322]. Acting as a filter, organizer, and conductor of fetal nutrient delivery and as an avenue for eliminating metabolic waste, proper functioning of the placenta is critical for nominal fetal development. Placental development and differentiation are extremely complex, involving several plasma membrane fusion-mediated molecular events that restructure gene expression profiles to reprogram cells from cytosolic independence on the periphery of the developing blastocyst to placenta [325,326]. Several factors in maternal diet can affect how this intricate process unfolds. Further study of its developmental underpinnings paired with PA imaging technologies will serve as an indispensable means of assessing and facilitating critical oxygen dynamics during development [327].

The work of Maneas et al. serves as an excellent example of the utility of PA imaging in deciphering vascular function during the fetal development process [81] PA imaging was capable of demarcating vasculature in deeper tissues that otherwise might be overlooked via white light imaging. In addition, contrast was obtained from the scar tissue post laser coagulation treatment. Future developments in the realm of endoscopic PA imaging systems will likely see such highly detailed oxygen dynamics as gleaned from their work moving into the *in vivo* arena for treating developmental disorders in humans. In another study by Yamaleyeva et al. [32] placental vasculature and sO_2 values were used to predict fetal nutrient insufficiency or the development of fetal hypoxia. Other methods of sO_2 acquisition such as MRI and contrast imaging, are prohibitively expensive for their wide adoption and have less than ideal data acquisition speed. Using PA imaging, they were able to confirm the relationships between hypertensive or hypoxic mothers, placental oxygen dynamics, and the resulting effects on fetal development [32]. In addition, PA imaging conferred increased sensitivity over current standards for assessing these placental-fetal relationships as scalp pH, scalp pO_2 , electrocardiography, pulse oximetry, and heart rate monitoring. Their oxygenation levels easily defined various disparate regions of the placental-fetal juncture via PA imaging, which may be used as a standard or control for future imaging studies. Using murine models of preeclampsia, Lawrence et al. noted that the onset of placental hypoxia can induce hypertension and increased translation of hypoxia-inducible factor 1 α (HIF-1 α), a known promoter of several pro-tumor progression pathways to include epithelial-mesenchymal transition [33]. This cascade of detrimental changes to the mother's vascular and proteomic dynamics illustrates the diverse array of effects that can result from misregulated oxygenation dynamics of the placenta, increasing the mother's risk for both atherosclerosis, heart disease, and the tumor-proliferative influence of HIF-1 α [328].

Fetal development is a complicated process, requiring proper genomic sequence, epigenomic modifications, and several precisely-timed cascades of transcription factors and cell signaling activity, [329]. Modern understanding of human fetal development is still based mainly upon libraries of preserved embryos. However, transcriptional profiling and cutting-edge imaging technologies are making great strides toward chronicling the steps and checkpoints of molecular activity necessary for healthy development [330–334]. PA imaging has once again carved out a unique place among these technologies, as its capacity for imaging vasculature and oxygen dynamics in a non-invasive

fashion has proven to be indispensable. Future developments in the pairing of mesoscale imaging systems and endoscopic PA imaging will serve to enhance both the scientific knowledgebase and therapeutic reach of applications to developmental disorders and dysfunction.

4.4. PA imaging for the detection of rheumatoid arthritis

Rheumatoid arthritis (RA), an inflammatory autoimmune disease, affects 0.24% of the human population and may progress to an immunological attack of the organs in addition to causing tremendous joint pain [335]. As is the case with cancer, the emergence of a state of inflammation and destruction around fluid-filled regions of the joints is a detailed summation of both genetic and environmental influence, making its treatment complex. Expression levels and the activity-regulation of tumor necrosis factor cytokines and their subsequent interplay with innate and adaptive immune cell receptors are the primary means of RA progression in the genomic and cellular domains. At the same time, such agonists as infection and microbiome activity have been shown to influence RA progression in the environmental domain [336]. The actions of both regimes are affected by molecular dynamics to include pO_2 , pCO_2 , pH, and the presence of ROS, all of which are beholden to existing or novel vasculature. Because of this, the study of RA via PA imaging has made great progress in the early detection and assessment of RA, which in turn improves therapeutic outcomes. Utilizing a $\lambda = 750/850$ nm PA imaging setup paired with a 7 MHz US transducer, Joseph et al. were able to successfully confirm the presence of a hypoxic state and neovascularization events in the hindlimbs of mice [337]. *In vivo* imaging of these dynamics over 20 days in arthritic mice was achieved by Guo et al. [338]. They administered free and micellated dexamethasone to ameliorate the effects of complete Freund's adjuvant induction into an inflamed/arthritic state [338]. Following PA and US imaging, histological analysis confirmed the correlations of PA signal intensity as a proxy for relative hemoglobin concentration, thus angiogenesis events, to structural aberrations in arthritic mice. In addition, they were able to apply their imaging setup to human joints, and future applications of PA imaging to clinical volunteers undergoing treatment for RA would further serve as a method for improving the validation of PA imaging's power to predict early indicators of the onset of RA such as hypoxia and angiogenesis around synovium.

5. Challenges for broader adaptation of the technology and future directions

PA imaging, since its inception in 1880 by Alexander Graham Bell [339,340], has traversed a long path and is now on the verge of becoming a vital tool in the armamentarium of clinical imaging technologies with many developments in the US, laser, and image processing fields. Some of the roadblocks that exist for broader adaptation of the technology for clinical applications include limited penetration depth, low temporal resolution compared to US imaging, relying on operator expertise to decipher artifacts and need for application dependent light delivery and detection scheme (i.e., lack of a universal system adaptable for imaging several areas in the body such as X-ray). Unlike MRI, CT, PET, and SPECT modalities, it is impossible to get whole human body or organ level images with PA imaging due to the limited penetration depth of the visible and NIR wavelengths in the tissue. More recently the develop the utility of NIR II window for deep tissue imaging has been demonstrated by several groups [341]. Though the fluence at the NIR II window of wavelengths is low, future developments in this area can push the penetration depth limits of PA imaging. Another aspect impacting light penetration depth is the melanin content and the pigmentation in the skin [136]. The variations in skin tone can impact light penetration and quantification. A recent study by Mantri et al. provided the correction factor based on the skin type to compensate for the discrepancy in oximetry measurements [134]. Further compensation

methods that include skin thickness and age is needed when clinically utilizing the technology on patients with broad range of skin types. Despite the limitation on penetration depth, high spatial resolution of the technology has proven to be useful in deciphering vascular information of the pathologies using endogenous contrast as described in this review. An added complexity here is that light fluence is directly impacted by the tissue optical absorption and scattering properties, thereby fluence compensation to quantify absorption in tissue is mathematically complicated problem. The utilization of various light illumination schemes (single fiber illumination, tomography, bi-directional multi-directional illuminations) exacerbates the complexity. Considering the light illumination to gauge fluence at the target of interest in the body to quantify optical absorber concentration remains a challenge.

Conventionally PA imaging employs high energy class IV Q-switched pulsed laser to obtain image with high SNR while the overall performance of the system depends on the high spatial resolution and fast temporal resolution that can be achieved. Even though PA imaging can provide functional information, its potential in real-time clinical applications is hindered by the low data acquisition speed that depends on the PRF of the lasers used which are typically less than 100 Hz [342,343]. In the recent decades, advancements in the semiconductor technologies led to the development of laser diodes and light emitting diodes (LED) to overcome the limitation of low PRF of Q-switched lasers. Particularly LEDs have very high PRF in the order of up to 16 kHz which results in an imaging frame rate of up to 60 Hz that is much higher than the Q-switched laser PA imaging systems [51,344,345]. Several clinical and preclinical studies have demonstrated the feasibility of compact, low-cost LED based PA imaging systems in potential real-time clinical applications. Particularly Wang et. al., demonstrated in a clinical study that LED based PA imaging systems can serve as a potential diagnostic imaging modality for inflammatory arthritis [346]. Other studies have validated the LED based PA imaging for vasculature imaging, monitoring angiogenesis and functional oxygen saturation imaging [51, 347–349]. The main drawback of the LEDs in comparison to the Q-switched lasers is that they have relatively low pulse energy. The energy output of LED array is in the order of 200 μ J per pulse. The high signal to noise ratio with the low pulse energies of LED can be compensated by exploiting their high PRF and averaging multiple frames. By averaging 384 frames the SNR of LED based PA imaging system can be improved by 20 times and the performance of system can be made comparable to lasers with peak energy of 8 mJ/pulse [51,344, 350]. Although averaging results in increased SNR, it reduces the imaging frame rate. There are few drawbacks in the LEDs based PA imaging system that needs to be addressed to have maximum impact in clinical applications. The current design of LED arrays has either single or dual wavelength emission as a result they cannot be spectrally tuned to other wavelengths which limits their use in multispectral PA spectroscopy. The low power of LED limits the penetration depth and affects SNR at high imaging frame rate. Lastly, the temporal pulse width of LEDs is larger than the lasers pulse width which imposes the limit on the spatial resolution of the system. Overall, despite the limitations, LEDs are significant advancements in PA imaging due to their flexible pulse-width settings, low-cost, compact nature, and high PRF and hold potential in real-time imaging.

Preclinical PA imaging systems employ either 2D array or 1D array or single element US transducers for image acquisition [23,351,352]. These systems generally acquire 2D images but real-time 3D visualization of a tumor or the surrounding vasculature would be highly beneficial and can expand the applications of PA imaging in many clinical settings. Often these PA systems employ automated 3D scanning with motorized electronic controls or mechanical 3D probe for facilitating 3D PA image acquisition. However, these scanners tend to be bulky and wouldn't be ideal for handheld operation [352,353]. Various ways have been developed to convert traditional PA imaging systems into handheld systems and a comprehensive review on them has been published elsewhere [354]. While PA images have high optical contrast-to-noise ratio,

the quantitation of chromophore concentration along with fluence compensation and artifact reduction are still a challenge. Several research studies the feasibility of using a light diffusion model to achieve a quantitative PA imaging and reduce the induced bias in spectral unmixing due to different tissue behavior at different wavelengths. However, this could be a challenging task due to the heterogeneity of some tissue structures and the complexity of the light diffusion model [355–357]. Deep learning (DL) based methodologies are being heralded as the next game changer for PA and the clinical translation of PA computed tomography and PA microscopy might be accelerated with DL due to its capability for resolution improvement, artifact removal, quality improvement with sparsely sampled data [358,359]. Recent research on image reconstruction utilizing signals from the transducer employed U-net [360–362], Deep convolutional neural network (CNN) [363], modified U-net [361,364] that significantly corrected limited-view and sparse sampled artifacts. The modified U-nets based DL methods are being implemented for under-sampled artifacts removal [365]. Gradient descent optimization-based DL strategies are also being applied heavily to various reconstruction tasks [366]. Furthermore, several recent studies also demonstrated that the low SNR in LED illuminated PA imaging systems can be addressed with various DL methods such as U-net [367,368], recurrent neural network (RNN) [363], multi-level wavelet CNN [369]. DL is also being explored in removal of motion blurriness using CNN [370] and sparse-sampled artifacts using U-net and CNN [371,372]. Denoising and resolution enhancement in photoacoustic microscopy was accomplished also with U-net [373]. In addition to improvement of SNR and artifact reduction, another aspect where DL is being used is spectral unmixing of the PA signals due to various chromophores in the tissue. Initial studies showed that modified multiwavelength spectral unmixing based on U-net [374,375] and RNN based Eigen spectra [376] have potential and could offer better results than traditional unmixing algorithms. The influx of publications on DL and PA imaging in the past 2–3 years showcases the potential that there is a lot of room for improvement and technological advances in the future. Particularly, as the field is evolving, perspective on determining proper training samples, reducing training time complexity, resolving the depth-limitation in the optical diffusive zone, making a more generalized network rather than probe specific algorithms could increase the reliability and usability of the technology.

Like any other imaging modality, the clinical translation and applications of the PA imaging technology will be highly dependent on its biosafety. In general, the safety of PA imaging can be divided into two major categories: safety of the imaging devices and toxicity of contrast agents. Since the scope of this review deals with PA imaging with endogenous contrast agents, we will focus on the safety of the devices. Device safety includes the PA acquisition component: i.e., ultrasonic component of PA imaging; is of no safety concern, inherited from the safety of the US imaging and the fact that it operates in passive receive mode. The major safety issue with most PA imaging systems is related to the safety of the laser and the maximum permissible exposure (MPE) on human tissue [377]. Laser safety is less of a concern for some PA imaging systems such as LED based PA imaging systems, PA microscopy and catheter or needle guidance where low energy lasers are often utilized. For deep tissue imaging, the accessible depth via PA imaging depends on the fluence of the excitation light on the surface of the tissue and is limited by MPE according to the laser safety use regulations determined by American National Standard Institute (ANSI). ANSI standards describe the maximum fluence (i.e., energy/surface area) which is safe to be irradiated to the skin at different wavelengths. Currently, the MPE set by ANSI is 20 mJ/cm² for 532 nm laser. These limits are defined for skin and the safety limits specific for other tissues are not defined. Currently, there are various attempts to investigate the safety aspects of increased fluence for deep tissue PA imaging [378,379]. These studies aim to introduce tissue specific safety limits for PA applications. Overall, complying with laser safety by limiting the body exposure to standard limits and of course proper eye protection of patients and imaging

system operators makes PA imaging a safe imaging modality.

6. Conclusion

PA imaging has shown a steady growth and tremendous potential for clinical and preclinical applications. Given the clinically relevant penetration depth of PA imaging and the facile combination with widely available clinical US imaging, it has become an attractive diagnostic choice for many translational clinical investigations. While augmenting PA imaging with exogenous molecular contrast agents enable PA imaging to detect events at cellular and at molecular levels, PA imaging of tissue's endogenous contrast seemingly have an easier path to be adopted in clinical applications. PA imaging of endogenous biomarkers such as hemoglobin, melanin, lipid, collagen, and water is shown to have important clinical diagnostic potency. Owing to its advantages such as acceptable temporal resolution (i.e., real-time), PA also demonstrated a great deal of promise for more accurate image-guidance of interventional and surgical procedures. The goal of this review article was to provide a summary of applications of PA imaging of endogenous contrast, discuss state-of-art development and introduce several niche applications where PA imaging systems are well-suited to enhance and revolutionize the field of diagnostic imaging and therapy monitoring.

Declaration of Competing Interest

The authors declare that they have no known competing financial interests or personal relationships that could have appeared to influence the work reported in this paper.

Data Availability

No data was used for the research described in the article.

Acknowledgements

The authors would like to acknowledge partial support from the NIH Funds R21CA263694 and R01CA266701 for Mallidi and R01EB030058 (NIH) and W81XWH-18-1-0039 (Department of Defense) for Mehrmohammadi.

References

- [1] E. Seeram, Computed tomography: a technical review, *Radio. Technol.* 89 (3) (2018), 279ct-302ct.
- [2] V.P.B. Grover, J.M. Tognarelli, M.M.E. Crossey, I.J. Cox, S.D. Taylor-Robinson, M. J.W. McPhail, Magnetic resonance imaging: principles and techniques: lessons for clinicians, *J. Clin. Exp. Hepatol.* 5 (3) (2015) 246–255.
- [3] R.S. Miletič, Positron Emission Tomography and Single-Photon Emission Computed Tomography in Neurology, *Continuum (Minneapolis)* 22(5, Neuroimaging) (2016) 1636–1654.
- [4] A.L. Klibanov, J.A. Hossack, Ultrasound in radiology: from anatomic, functional, molecular imaging to drug delivery and image-guided therapy, *Invest Radio.* 50 (9) (2015) 657–670.
- [5] C. Balas, Review of biomedical optical imaging—a powerful, non-invasive, non-ionizing technology for improving in vivo diagnosis, *Meas. Sci. Technol.* 20 (10) (2009), 104020.
- [6] L.V. Wang, S. Hu, Photoacoustic tomography: in vivo imaging from organelles to organs, *science* 335 (6075) (2012) 1458–1462.
- [7] M. Xu, L.V. Wang, Photoacoustic imaging in biomedicine, *Rev. Sci. Instrum.* 77 (4) (2006), 041101.
- [8] S. Manohar, D. Razansky, Photoacoustics: a historical review, *Adv. Opt. Photon* 8 (4) (2016), 586–32.
- [9] S. Mallidi, G.P. Luke, S. Emelianov, Photoacoustic imaging in cancer detection, diagnosis, and treatment guidance, *Trends Biotechnol.* 29 (5) (2011) 213–221.
- [10] S. Sethuraman, S.R. Aglyamov, J.H. Amirian, R.W. Smalling, S.Y. Emelianov, Intravascular photoacoustic imaging using an IVUS imaging catheter, *IEEE Trans. Ultrason., Ferroelectr., Freq. Control* 54 (5) (2007) 978–986.
- [11] M. Juratli, E. Galanzha, M. Sarimollaoglu, D. Nedosekin, J. Suen, V. Zharov, Photoacoustic monitoring of clot formation during surgery and tumor surgery, *SPIE* 2013.
- [12] S.C. Hester, M. Kuriakose, C.D. Nguyen, S. Mallidi, Role of ultrasound and photoacoustic imaging in photodynamic therapy for cancer, *Photochem. Photobiol.* 96 (2) (2020) 260–279.

- [13] S. Mallidi, T. Larson, J. Aaron, K. Sokolov, S. Emelianov, Molecular specific optoacoustic imaging with plasmonic nanoparticles, *Opt. Express* 15 (11) (2007) 6583–6588.
- [14] X. Yang, E.W. Stein, S. Ashkenazi, L.V. Wang, Nanoparticles for photoacoustic imaging, *WIREs Nanomed. Nanobiotechnol.* 1 (4) (2009) 360–368.
- [15] G.P. Luke, D. Yeager, S.Y. Emelianov, Biomedical applications of photoacoustic imaging with exogenous contrast agents, *Ann. Biomed. Eng.* 40 (2) (2012) 422–437.
- [16] A. Hannah, G. Luke, K. Wilson, K. Homan, S. Emelianov, Indocyanine green-loaded photoacoustic nanodroplets: dual contrast nanoconstructs for enhanced photoacoustic and ultrasound imaging, *ACS Nano* 8 (1) (2014) 250–259.
- [17] Adl Zerda, Z. Liu, S. Bodapati, R. Teed, S. Vaithilingam, B.T. Khuri-Yakub, X. Chen, H. Dai, S.S. Gambhir, Ultrahigh sensitivity carbon nanotube agents for photoacoustic molecular imaging in living mice, *Nano Lett.* 10 (6) (2010) 2168–2172.
- [18] R.E. Borg, J. Rochford, Molecular photoacoustic contrast agents: design principles & applications, *Photochem. Photobiol.* 94 (6) (2018) 1175–1209.
- [19] Q. Chen, W. Qin, W. Qi, L. Xi, Progress of clinical translation of handheld and semi-handheld photoacoustic imaging, *Photoacoustics* 22 (2021), 100264.
- [20] H.F. Zhang, K. Maslov, M. Sivaramakrishnan, G. Stoica, L.V. Wang, Imaging of hemoglobin oxygen saturation variations in single vessels in vivo using photoacoustic microscopy, *Appl. Phys. Lett.* 90 (5) (2007), 053901.
- [21] X. Wang, X. Xie, G. Ku, L.V. Wang, G. Stoica, Noninvasive imaging of hemoglobin concentration and oxygenation in the rat brain using high-resolution photoacoustic tomography, *J. Biomed. Opt.* 11 (2) (2006), 024015.
- [22] M. Li, Y. Tang, J. Yao, Photoacoustic tomography of blood oxygenation: a mini review, *Photoacoustics* 10 (2018) 65–73.
- [23] M. Xavierselvan, J. Cook, J. Duong, N. Diaz, K. Homan, S. Mallidi, Photoacoustic nanodroplets for oxygen enhanced photodynamic therapy of cancer, *Photoacoustics* 25 (2022), 100306.
- [24] J.M. Mari, W. Xia, S.J. West, A.E. Desjardins, Interventional multispectral photoacoustic imaging with a clinical ultrasound probe for discriminating nerves and tendons: an ex vivo pilot study, *J. Biomed. Opt.* 20 (11) (2015), 110503.
- [25] Y. Yan, S. John, T. Shaik, B. Patel, M.T. Lam, L. Kabbani, M. Mehrmohammadi, Photoacoustic-guided endovenous laser ablation: characterization and in vivo canine study, *Photoacoustics* 24 (2021), 100298.
- [26] S.L. Jacques, S.A. Prahl, Assorted Spectra. <https://omlc.org/spectra/> (Accessed 07/25/ 2022).
- [27] T. Paola, B. Andrea, C. Daniela, F. Andrea, C. Rinaldo, P. Antonio, Diffuse optical spectroscopy of breast tissue extended to 1100 nm, *J. Biomed. Opt.* 14 (5) (2009) 1–7.
- [28] Y. Matsumoto, Y. Asao, A. Yoshikawa, H. Sekiguchi, M. Takada, M. Furu, S. Saito, M. Kataoka, H. Abe, T. Yagi, K. Togashi, M. Toi, Label-free photoacoustic imaging of human palmar vessels: a structural morphological analysis, *Sci. Rep.* 8 (1) (2018) 786.
- [29] H. Yun, S. Junhui, I.M. Konstantin, C. Rui, V.W. Lihong, Wave of single-impulse-stimulated fast initial dip in single vessels of mouse brains imaged by high-speed functional photoacoustic microscopy, *J. Biomed. Opt.* 25 (6) (2020) 1–11.
- [30] L. Lin, P. Hu, J. Shi, C.M. Appleton, K. Maslov, L. Li, R. Zhang, L.V. Wang, Single-breath-hold photoacoustic computed tomography of the breast, *Nat. Commun.* 9 (1) (2018) 2352.
- [31] K. Haedicke, L. Agemy, M. Omar, A. Bereznoi, S. Roberts, C. Longo-Machado, M. Skubal, K. Nagar, H.-T. Hsu, K. Kim, High-resolution optoacoustic imaging of tissue responses to vascular-targeted therapies, *Nat. Biomed. Eng.* 4 (3) (2020) 286–297.
- [32] L.M. Yamaleyeva, Y. Sun, T. Bledsoe, A. Hoke, S.B. Gurley, K.B. Brosnihan, Photoacoustic imaging for in vivo quantification of placental oxygenation in mice, *FASEB J.* 31 (12) (2017) 5520–5529.
- [33] D.J. Lawrence, M.E. Escott, L. Myers, S. Intapad, S.H. Lindsey, C.L. Bayer, Spectral photoacoustic imaging to estimate in vivo placental oxygenation during preeclampsia, *Sci. Rep.* 9 (1) (2019) 558.
- [34] S. Mallidi, K. Watanabe, D. Timerman, D. Schoenfeld, T. Hasan, Prediction of tumor recurrence and therapy monitoring using ultrasound-guided photoacoustic imaging, *Theranostics* 5 (3) (2015) 289–301.
- [35] Y. Mantri, J. Tsujimoto, B. Donovan, C.C. Fernandes, P.S. Garimella, W.F. Penny, C.A. Anderson, J.V. Jakerst, Photoacoustic monitoring of angiogenesis predicts response to therapy in healing wounds, *Wound Repair Regen.* 30 (2) (2022) 258–267.
- [36] Y. Mantri, A. Mishra, C.A. Anderson, J.V. Jakerst, Photoacoustic imaging to monitor outcomes during hyperbaric oxygen therapy: validation in a small cohort and case study in a bilateral chronic ischemic wound, *Biomed. Opt. Express* 13 (11) (2022) 5683–5694.
- [37] X. Zhu, Q. Huang, A. DiSpirito, T. Vu, Q. Rong, X. Peng, H. Sheng, X. Shen, Q. Zhou, L. Jiang, U. Hoffmann, J. Yao, Real-time whole-brain imaging of hemodynamics and oxygenation at micro-vessel resolution with ultrafast wide-field photoacoustic microscopy, *Light.: Sci. Appl.* 11 (1) (2022) 138.
- [38] X. Cai, A. Bandla, C. Wang, Y. Liu, C.K. Chuan, Y. Xu, X. Liu, S. Xu, W. Wu, N. V. Thakor, B. Liu, Photothermal-Activatable Liposome Carrying Tissue Plasminogen Activator for Photoacoustic Image-Guided Ischemic Stroke Treatment, *Small Struct.* 3 (2022), 2100118.
- [39] S. Na, J.J. Russin, L. Lin, X. Yuan, P. Hu, K.B. Jann, L. Yan, K. Maslov, J. Shi, D. J. Wang, C.Y. Liu, L.V. Wang, Massively parallel functional photoacoustic computed tomography of the human brain, *Nat. Biomed. Eng.* 6 (5) (2022) 584–592.
- [40] I. Daimiel, Insights into hypoxia: non-invasive assessment through imaging modalities and its application in breast cancer, *J. Breast Cancer* 22 (2) (2019) 155–171.
- [41] J. Kim, B. Park, J. Ha, I. Steinberg, E.-Y. Park, W. Choi, S. Hooper, S.S. Gambhir, D.-J. Lim, C. Kim, Multispectral photoacoustic assessment of thyroid cancer nodules in vivo, *Photons Plus Ultrasound: imaging and Sensing 2020*, Int. Soc. Opt. Photonics (2020) 1124004.
- [42] T.L. Lefebvre, E. Brown, L. Hacker, T. Else, M.-E. Oraipoulou, M. R. Tomaszewski, R. Jena, S.E. Bohndiek, The potential of photoacoustic imaging in radiation oncology, *Front. Oncol.* 12 (2022).
- [43] E. Liapis, A. Karlas, U. Klemm, V. Ntziachristos, Chemotherapeutic effects on breast tumor hemodynamics revealed by eigenspectra multispectral photoacoustic tomography (eMSOT), *Theranostics* 11 (16) (2021) 7813–7828.
- [44] D.J. Rohrbach, H. Salem, M. Aksahin, U. Sunar, Photodynamic therapy-induced microvascular changes in a nonmelanoma skin cancer model assessed by photoacoustic microscopy and diffuse correlation spectroscopy, *Photonics, Multidiscip. Digit. Publ. Inst.* (2016) 48.
- [45] P. Keša, E. Pokorná, M. Grajciarová, Z. Tonar, P. Vočková, P. Trochet, M. Kopeček, R. Jakša, L. Sefc, P. Klener, Quantitative in vivo monitoring of hypoxia and vascularization of patient-derived murine xenografts of mantle cell lymphoma using photoacoustic and ultrasound imaging, *Ultrasound Med. Biol.* 47 (4) (2021) 1099–1107.
- [46] J. Li, A. Chekkoury, J. Prakash, S. Glasl, P. Vetschera, B. Koberstein-Schwarz, I. Olefir, V. Gujrati, M. Omar, V. Ntziachristos, Spatial heterogeneity of oxygenation and haemodynamics in breast cancer resolved in vivo by conical multispectral photoacoustic mesoscopy, *Light.: Sci. Appl.* 9 (1) (2020) 57.
- [47] E. Hysi, L.A. Wirtzfeld, J.P. May, E. Undzys, S.-D. Li, M.C. Kolios, Photoacoustic signal characterization of cancer treatment response: correlation with changes in tumor oxygenation, *Photoacoustics* 5 (2017) 25–35.
- [48] E. Liapis, U. Klemm, A. Karlas, J. Reber, V. Ntziachristos, Resolution of spatial and temporal heterogeneity in bevacizumab-treated breast tumors by eigenspectra multispectral photoacoustic tomography, *Cancer Res.* 80 (23) (2020) 5291–5304.
- [49] I. Quiros-Gonzalez, M.R. Tomaszewski, M.A. Golinska, E. Brown, L. Ansel-Bollepalli, L. Hacker, D.-L. Couturier, R.M. Sainz, S.E. Bohndiek, Photoacoustic tomography detects response and resistance to bevacizumab in breast cancer mouse models, *Cancer Res.* 82 (8) (2022) 1658–1668.
- [50] L.J. Rich, A. Miller, A.K. Singh, M. Seshadri, Photoacoustic imaging as an early biomarker of radio therapeutic efficacy in head and neck cancer, *Theranostics* 8 (8) (2018) 2064–2078.
- [51] M. Xavierselvan, M.K.A. Singh, S. Mallidi, In vivo tumor vascular imaging with light emitting diode-based photoacoustic imaging system, *Sensors* 20 (16) (2020) 4503.
- [52] M.R. Tomaszewski, I.Q. Gonzalez, J.P. O'Connor, O. Abeyakoon, G.J. Parker, K. J. Williams, F.J. Gilbert, S.E. Bohndiek, Oxygen enhanced optoacoustic tomography (OE-OT) reveals vascular dynamics in murine models of prostate cancer, *Theranostics* 7 (11) (2017) 2900–2913.
- [53] J.-M. Yang, C. Favazza, R. Chen, J. Yao, X. Cai, K. Maslov, Q. Zhou, K.K. Shung, L. V. Wang, Simultaneous functional photoacoustic and ultrasonic endoscopy of internal organs in vivo, *Nat. Med.* 18 (8) (2012) 1297–1302.
- [54] A. Claus, A. Sweeney, D.M. Sankepal, B. Li, D. Wong, M. Xavierselvan, S. Mallidi, 3D ultrasound-guided photoacoustic imaging to monitor the effects of suboptimal tyrosine kinase inhibitor therapy in pancreatic tumors, *Front. Oncol.* 12 (2022).
- [55] E. Amidi, G. Yang, K.M.S. Uddin, H. Luo, W. Middleton, M. Powell, C. Siegel, Q. Zhu, Role of blood oxygenation saturation in ovarian cancer diagnosis using multi-spectral photoacoustic tomography, *J. Biophotonics* 14 (4) (2021), e202000368.
- [56] K. Kratkiewicz, A. Pattyn, N. Alijabbari, M. Mehrmohammadi, Ultrasound and photoacoustic imaging of breast cancer: clinical systems, challenges, and future outlook, *J. Clin. Med* 11 (5) (2022).
- [57] N. Nyayapathi, J. Xia, Photoacoustic imaging of breast cancer: a mini review of system design and image features, *J. Biomed. Opt.* 24 (12) (2019), 121911.
- [58] R.W. Pinsky, M.A. Helvie, Mammographic breast density: effect on imaging and breast cancer risk, *J. Natl. Compr. Cancer Netw.* 8 (10) (2010) 1157–1165.
- [59] V.A. McCormack, I. dos Santos, Silva, Breast density and parenchymal patterns as markers of breast cancer risk: a meta-analysis, *Cancer Epidemiology and Prevention, Biomarkers* 15 (6) (2006) 1159–1169.
- [60] N. Oebisu, M. Hoshi, M. Ieguchi, J. Takada, T. Iwai, M. Ohsawa, H. Nakamura, Contrast-enhanced color Doppler ultrasonography increases diagnostic accuracy for soft tissue tumors, *Oncol. Rep.* 32 (4) (2014) 1654–1660.
- [61] P. Beard, Biomedical photoacoustic imaging, *Interface Focus* 1 (4) (2011) 602–631.
- [62] D. Hanahan, R.A. Weinberg, Hallmarks of cancer: the next generation, *Cell* 144 (5) (2011) 646–674.
- [63] D. Piras, W. Xia, W. Steenbergen, T.Gv Leeuwen, S. Manohar, Photoacoustic imaging of the breast using the twelve photoacoustic mammoscope: present status and future perspectives, *IEEE J. Sel. Top. Quantum Electron.* 16 (4) (2010) 730–739.
- [64] S.M. Schoustra, D. Piras, R. Huijink, T. Op 't Root, L. Alink, W.M. Kobold, W. Steenbergen, S. Manohar, Twente Photoacoustic Mammoscope 2: system overview and three-dimensional vascular network images in healthy breasts, *J. Biomed. Opt.* 24 (12) (2019) 1–12.
- [65] A. Oraevsky, R. Su, H. Nguyen, J. Moore, Y. Lou, S. Bhadra, L. Forte, M. Anastasio, W. Yang, Full-view 3D imaging system for functional and

- anatomical screening of the breast, *Photons Plus Ultrasound: imaging and Sensing* 2018, *Int. Soc. Opt. Photonics* (2018) 104942Y.
- [66] R.A. Kruger, C.M. Kuzmiak, R.B. Lam, D.R. Reinecke, S.P. Del Rio, D. Steed, Dedicated 3D photoacoustic breast imaging, *Med Phys.* 40 (11) (2013), 113301.
- [67] S.S. Alshahrani, Y. Yan, N. Alijabbari, A. Pattyn, I. Avrutsky, E. Malyarenko, J. Poudel, M. Anastasio, M. Mehrmohammadi, All-reflective ring illumination system for photoacoustic tomography, *J. Biomed. Opt.* 24 (4) (2019), 046004.
- [68] N. Alijabbari, S.S. Alshahrani, A. Pattyn, M. Mehrmohammadi, Photoacoustic tomography with a ring ultrasound transducer: a comparison of different illumination strategies, *Appl. Sci. (Basel)* 9 (15) (2019) 3094.
- [69] S. Alshahrani, Y. Yan, I. Avrutsky, E. Malyarenko, M. Anastasio, M. Mehrmohammadi, An advanced photoacoustic tomography system based on a ring geometry design, *Medical Imaging 2018: ultrasonic Imaging and Tomography*, *Int. Soc. Opt. Photonics* (2018) 1058005.
- [70] A.A. Oraevsky, B. Clingman, J. Zalev, A.T. Stavros, W.T. Yang, J.R. Parikh, Clinical photoacoustic imaging combined with ultrasound for coregistered functional and anatomical mapping of breast tumors, *Photoacoustics* 12 (2018) 30–45.
- [71] U.S.F.a.D. Administration, *Imagio® Breast Imaging System – P200003, FDA's approval to market* (2021).
- [72] H. Zhao, N. Chen, T. Li, J. Zhang, R. Lin, X. Gong, L. Song, Z. Liu, C. Liu, Motion correction in optical resolution photoacoustic microscopy, *IEEE Trans. Med. Imaging* 38 (9) (2019) 2139–2150.
- [73] L.V. Wang, Prospects of photoacoustic tomography, *Med. Phys.* 35 (12) (2008) 5758–5767.
- [74] Xue Wen, Peng Lei, Kedi Xiong, Pengfei Zhang, Sihua Yang, High-robustness intravascular photoacoustic endoscope with a hermetically sealed opto-sono capsule, *Opt. Express* 28 (2020) 19255–19269.
- [75] X. Jing, F. Yang, C. Shao, K. Wei, M. Xie, H. Shen, Y. Shu, Role of hypoxia in cancer therapy by regulating the tumor microenvironment, *Mol. Cancer* 18 (1) (2019) 157.
- [76] D.M. Brizel, S.P. Scully, J.M. Harrelson, L.J. Layfield, J.M. Bean, L.R. Prosnitz, M. W. Dewhirst, Tumor oxygenation predicts for the likelihood of distant metastases in human soft tissue sarcoma, *Cancer Res.* 56 (5) (1996) 941.
- [77] Z. Xie, C. Shu, X. Gong, L. Song, Carotid atherosclerosis detection using photoacoustic imaging system, *SPIE2019*.
- [78] J. Lv, S. Li, J. Zhang, F. Duan, Z. Wu, R. Chen, M. Chen, S. Huang, H. Ma, L. Nie, In vivo photoacoustic imaging dynamically monitors the structural and functional changes of ischemic stroke at a very early stage, *Theranostics* 10 (2) (2020) 816–828.
- [79] V.H. Fingar, Vascular effects of photodynamic therapy, *J. Clin. Laser Med. Surg.* 14 (5) (1996) 323–328.
- [80] M. Trendowski, The promise of sonodynamic therapy, *Cancer Metastas. Rev.* 33 (1) (2014) 143–160.
- [81] E. Maneas, R. Aughwane, N. Huynh, W. Xia, R. Ansari, M. Kuniyil Ajith Singh, J. C. Hutchinson, N.J. Sebire, O.J. Arthurs, J. Deprest, S. Ourselin, P.C. Beard, A. Melbourne, T. Vercauteren, A.L. David, A.E. Desjardins, Photoacoustic imaging of the human placental vasculature, *J. Biophotonics* 13 (4) (2020), e201900167.
- [82] K. Lund-Olesen, Oxygen tension in synovial fluids, *Arthritis Rheum.* 13 (6) (1970) 769–776.
- [83] S. Toyokuni, K. Okamoto, J. Yodoi, H. Hiai, Persistent oxidative stress in cancer, *FEBS Lett.* 358 (1) (1995) 1–3.
- [84] M. Johansson, D.G. DeNardo, L.M. Coussens, Polarized immune responses differentially regulate cancer development, *Immunol. Rev.* 222 (1) (2008) 145–154.
- [85] G.S. Charames, B. Bapat, Genomic instability and cancer, *Curr. Mol. Med.* 3 (7) (2003) 589–596.
- [86] W.C. Willett, B. MacMahon, Diet and cancer—an overview, *New Engl. J. Med.* 310 (11) (1984) 697–703.
- [87] Q. Shao, E. Morgounova, S. Ashkenazi, Tissue oxygen monitoring by photoacoustic lifetime imaging (PALI) and its application to image-guided photodynamic therapy (PDT), *SPIE2015*.
- [88] R.I. Siphanto, K.K. Thumma, R.G.M. Kolkman, T.Gv Leeuwen, F.F.Md Mul, J. Wv Neck, L.N.Av Adrichem, W. Steenbergen, Serial noninvasive photoacoustic imaging of neovascularization in tumor angiogenesis, *Opt. Express* 13 (1) (2005) 89–95.
- [89] K. Tachibana, L.B. Feril, Y. Ikeda-Dantsuji, Sonodynamic therapy, *Ultrasonics* 48 (4) (2008) 253–259.
- [90] P.A. Riley, Melanin, *Int. J. Biochem. Cell B* 29 (11) (1997) 1235–1239.
- [91] N. Kollias, A.H. Baqer, Absorption mechanisms of human melanin in the visible, 400–720 nm, *J. Invest. Dermatol.* 89 (4) (1987) 384–388.
- [92] S.D. Koziowski, L.J. Wolfram, R.R. Alfano, Fluorescence spectroscopy of eumelanins, *IEEE J. Quantum Elect.* 20 (12) (1984) 1379–1382.
- [93] J.M. Gallas, M. Eisner, Fluorescence of melanin dependence upon excitation wavelength and concentration, *Photochem. Photobiol.* 45 (5) (1987) 595–600.
- [94] D. Wrobel, A. Planner, I. Hanyz, A. Wielgus, T. Sarna, Melanin-porphyrin interaction monitored by delayed luminescence and photoacoustics, *J. Photo Photo B* 41 (1–2) (1997) 45–52.
- [95] R.H. Silverman, F. Kong, Y.C. Chen, H.O. Lloyd, H.H. Kim, J.M. Cannata, K. K. Shung, D.J. Coleman, High-resolution photoacoustic imaging of ocular tissues, *Ultrasound Med Biol.* 36 (5) (2010) 733–742.
- [96] X. Shu, H. Li, B.Q. Dong, C. Sun, H.F. Zhang, Quantifying melanin concentration in retinal pigment epithelium using broadband photoacoustic microscopy, *Biomed. Opt. Express* 8 (6) (2017) 2851–2865.
- [97] G.C. Langhout, D.J. Grootendorst, O.E. Nieweg, M.W. Wouters, J.A. van der Hage, J. Jose, H. van Boven, W. Steenbergen, S. Manohar, T.J. Ruers, Detection of melanoma metastases in resected human lymph nodes by noninvasive multispectral photoacoustic imaging, *Int. J. Biomed. Imaging* 2014 (2014), 163652.
- [98] J. Hult, A. Merdasa, A. Pekar-Lukacs, M. Tordengren Stridh, A. Khodaverdi, J. Albinsson, B. Gesslein, U. Dahlstrand, L. Engqvist, Y. Hamid, D. Larsson Albér, B. Persson, T. Erlöv, R. Sheikh, M. Cinthio, M. Malmjö, Comparison of photoacoustic imaging and histopathological examination in determining the dimensions of 52 human melanomas and nevi ex vivo, *Biomed. Opt. Express* 12 (7) (2021) 4097–4114.
- [99] Magne Tordengren Stridh, Jenny Hult, Aboma Merdasa, John Albinsson, Agnes Pekar-Lukacs, Bodil Gesslein, Ulf Dahlstrand, Karl Engelsberg, Johanna Berggren, Magnus Cinthio, Rafi Sheikh, Malin Malmjö, Photoacoustic imaging of periorbital skin cancer ex vivo: unique spectral signatures of malignant melanoma, basal, and squamous cell carcinoma, *Biomed. Opt. Express* 13 (2022) 410–425.
- [100] S.L. Jacques, D.J. McAuliffe, The melanosome: threshold temperature for explosive vaporization and internal absorption coefficient during pulsed laser irradiation, *Photochem. Photobiol.* 53 (6) (1991) 769–775.
- [101] T. Liu, X.J. Liu, R. Wen, Y.W. Li, C.A. Puliafito, H.F. Zhang, S.L. Jiao, Optical coherence photoacoustic microscopy for in vivo multimodal retinal imaging, *Invest Ophth Vis. Sci.* 56 (7) (2015).
- [102] J.-T. Oh, M.-L. Li, H.F. Zhang, K. Maslov, L.V. Wang, Three-dimensional imaging of skin melanoma in vivo by dual-wavelength photoacoustic microscopy, *J. Biomed. Opt.* 11 (3) (2006), 034032.
- [103] X. Shu, W. Liu, H.F. Zhang, Monte Carlo investigation on quantifying the retinal pigment epithelium melanin concentration by photoacoustic ophthalmoscopy, *J. Biomed. Opt.* 20 (10) (2015), 106005.
- [104] N.C.F. Codella, D. Gutman, M.E. Celebi, B. Helba, M.A. Marchetti, S.W. Dusza, A. Kallou, K. Liopyris, N. Mishra, H. Kittler, A. Halpern, Skin lesion analysis toward melanoma detection: A challenge at the 2017 International symposium on biomedical imaging (ISBI), hosted by the international skin imaging collaboration (ISIC), 2018 IEEE 15th International Symposium on Biomedical Imaging (ISBI 2018), 2018, pp. 168–172.
- [105] E.I. Galanzha, E.V. Shashkov, P.M. Spring, J.Y. Suen, V.P. Zharov, In vivo, noninvasive, label-free detection and eradication of circulating metastatic melanoma cells using two-color photoacoustic flow cytometry with a diode laser, *Cancer Res* 69 (20) (2009) 7926–7934.
- [106] D.A. Nedosekin, M. Sarimollaoglu, E.V. Shashkov, E.I. Galanzha, V.P. Zharov, Ultra-fast photoacoustic flow cytometry with a 0.5 MHz pulse repetition rate nanosecond laser, *Opt. Express* 18 (8) (2010) 8605–8620.
- [107] Y. Wang, K. Maslov, Y. Zhang, S. Hu, L. Yang, Y. Xia, J. Liu, L.V. Wang, Fiber-laser-based photoacoustic microscopy and melanoma cell detection, *J. Biomed. Opt.* 16 (1) (2011), 011014.
- [108] R. Marchesini, A. Bono, M. Carrara, In vivo characterization of melanin in melanocytic lesions: spectroscopic study on 1671 pigmented skin lesions, *J. Biomed. Opt.* 14 (1) (2009), 014027.
- [109] H.F. Zhang, K. Maslov, G. Stoica, L.V. Wang, Functional photoacoustic microscopy for high-resolution and noninvasive in vivo imaging, *Nat. Biotechnol.* 24 (7) (2006) 848–851.
- [110] V.G. Kanellis, A review of melanin sensor devices, *Biophys. Rev.* 11 (6) (2019) 843–849.
- [111] J.A. Viator, L.O. Svaasand, G. Aguilar, B. Choi, J.S. Nelson, Photoacoustic measurement of epidermal melanin, *P Soc. Photo-Opt. Ins.* 4960 (2003) 14–20.
- [112] K. Park, J.Y. Kim, C. Lee, S. Jeon, G. Lim, C. Kim, Handheld photoacoustic microscopy probe, *Sci. Rep.* 7 (1) (2017) 13359.
- [113] S.J. Ford, P.L. Bigliardi, T.C.P. Sardella, A. Ulrich, N.C. Burton, M. Kacprowicz, M. Bigliardi, M. Olivo, D. Razansky, Structural and functional analysis of intact hair follicles and pilosebaceous units by volumetric multispectral photoacoustic tomography, *J. Invest. Dermatol.* 136 (4) (2016) 753–761.
- [114] B. Hindelang, J. Aguirre, A. Bereznoi, H. He, K. Eyerich, V. Ntziachristos, T. Biedermann, U. Darsow, Optoacoustic mesoscopy shows potential to increase accuracy of allergy patch testing, *Contact Dermat.* 83 (3) (2020) 206–214.
- [115] S. Khattak, N. Gupta, X. Zhou, L. Pires, B.C. Wilson, Y.H. Yucel, Non-invasive dynamic assessment of conjunctival melanomas by photoacoustic imaging, *Exp. Eye Res.* 179 (2019) 157–167.
- [116] P.K. Kelsey, J.S. Eric, C.R. Ethier, E. Stanislav, Photoacoustic properties of anterior ocular tissues, *J. Biomed. Opt.* 24 (5) (2019), 056004.
- [117] J. Nolan, M. Sarimollaoglu, D.A. Nedosekin, A. Jamshidi-Parsian, E.I. Galanzha, R.A. Kore, R.J. Griffin, V.P. Zharov, In vivo flow cytometry of circulating tumor-associated exosomes, *Anal. Cell. Pathol.* 2016 (2016) 1628057.
- [118] J. Lavaud, M. Henry, J.L. Coll, V. Jossierand, Exploration of melanoma metastases in mice brains using endogenous contrast photoacoustic imaging, *Int. J. Pharm.* 532 (2) (2017) 704–709.
- [119] R.H. Edgar, A. Tarhini, C. Sander, M.E. Sanders, J.L. Cook, J.A. Viator, Predicting metastasis in melanoma by enumerating circulating tumor cells using photoacoustic flow cytometry, *Lasers Surg. Med.* 53 (4) (2021) 578–586.
- [120] A.J. Sinnamon, M.G. Neuwirth, Y. Song, S.M. Schultz, S. Liu, X. Xu, C.M. Sehgal, G.C. Karakousis, Multispectral photoacoustic imaging for the detection of subclinical melanoma, *J. Surg. Oncol.* 119 (8) (2019) 1070–1076.
- [121] V. Neuschmelting, H. Lockau, V. Ntziachristos, J. Grimm, M.F. Kircher, Lymph node micrometastases and in-transit metastases from melanoma: in vivo detection with multispectral photoacoustic imaging in a mouse model, *Radiology* 280 (1) (2016) 137.
- [122] I. Stoffels, S. Morscher, I. Helfrich, U. Hillen, J. Leyh, N.C. Burton, T.C. Sardella, J. Claussen, T.D. Poeppel, H.S. Bachmann, Metastatic status of sentinel lymph

- nodes in melanoma determined noninvasively with multispectral optoacoustic imaging, *Sci. Transl. Med.* 7 (317) (2015), 317ra199–317ra199.
- [123] A. Khodaverdi, T. Erlöv, J. Hult, N. Reistad, A. Pekar-Lukacs, J. Albinsson, A. Merdasa, R. Sheikh, M. Malmjö, M. Cinthio, Automatic threshold selection algorithm to distinguish a tissue chromophore from the background in photoacoustic imaging, *Biomed. Opt. Express* 12 (7) (2021) 3836–3850.
- [124] H. Ma, Z. Wang, Z. Cheng, G. He, T. Feng, C. Zuo, H. Qiu, Multiscale confocal photoacoustic dermoscopy to evaluate skin health, *Quant. Imaging Med. Surg.* 12 (5) (2022) 2696–2708.
- [125] B. Park, C. Bang, C. Lee, J. Han, W. Choi, J. Kim, G. Park, J. Rhie, J. Lee, C. Kim, 3D wide-field multispectral photoacoustic imaging of human melanomas in vivo: a pilot study, *J. Eur. Acad. Dermatol. Venereol.* 35 (3) (2021) 669–676.
- [126] P. Hai, Y. Qu, Y. Li, L. Zhu, L. Shmuylovich, L.A. Cornelius, L.V. Wang, Label-free high-throughput photoacoustic tomography of suspected circulating melanoma tumor cells in patients in vivo, *J. Biomed. Opt.* 25 (3) (2020), 036002.
- [127] E.I. Galanzha, Y.A. Menyayev, A.C. Yadem, M. Sarimollaoglu, M.A. Juratli, D. A. Nedosekin, S.R. Foster, A. Jamshidi-Parsian, E.R. Siegel, I. Makhoul, L. F. Hutchins, J.Y. Suen, V.P. Zharov, In vivo liquid biopsy using Cytophone platform for photoacoustic detection of circulating tumor cells in patients with melanoma, *Sci. Transl. Med.* 11 (496) (2019) eaat5857.
- [128] B. Aedán, C. Elizabeth, J.D. Jemima, S. Shazrinizam, M. James, J. Jithin, L.K.M. D. Jack, J.L. Martin, Preoperative measurement of cutaneous melanoma and nevi thickness with photoacoustic imaging, *J. Med. Imaging* 5 (1) (2018), 015004.
- [129] Z. Xu, Y. Pan, N. Chen, S. Zeng, L. Liu, R. Gao, J. Zhang, C. Fang, L. Song, C. Liu, Visualizing tumor angiogenesis and boundary with polygon-scanning multiscale photoacoustic microscopy, *Photoacoustics* 26 (2022), 100342.
- [130] T.T. Mai, S.W. Yoo, S. Park, J.Y. Kim, K.-H. Choi, C. Kim, S.Y. Kwon, J.-J. Min, C. Lee, In vivo quantitative vasculature segmentation and assessment for photodynamic therapy process monitoring using photoacoustic microscopy, *Sensors* 21 (5) (2021) 1776.
- [131] R. Garza-Morales, B.E. Rendon, M.T. Malik, J.E. Garza-Cabrales, A. Aucouturier, L.G. Bermúdez-Humarán, K.M. McMasters, L.R. McNally, J.G. Gomez-Gutierrez, Targeting melanoma hypoxia with the food-grade lactic acid bacterium *Lactococcus lactis*, *Cancers* 12 (2) (2020).
- [132] J. Zhang, F. Duan, Y. Liu, L. Nie, High-resolution photoacoustic tomography for early-stage cancer detection and its clinical translation, *Radiol.: Imaging Cancer* 2 (3) (2020).
- [133] N. Liu, Z. Chen, D. Xing, Integrated photoacoustic and hyperspectral dual-modality microscopy for co-imaging of melanoma and cutaneous squamous cell carcinoma in vivo, *J. Biophoton.* 13 (8) (2020), e202000105.
- [134] Y. Mantri, J.V. Jokerst, Impact of skin tone on photoacoustic oximetry and tools to minimize bias, *Biomed. Opt. Express* 13 (2) (2022) 875–887.
- [135] G. Fredman, Y. Qiu, M. Ardigo, M. Mogensen, Skin tags imaged by reflectance confocal microscopy, optical coherence tomography and multispectral optoacoustic tomography at the bedside, *Ski. Res. Technol.* 27 (3) (2021) 324–331.
- [136] X. Li, U. Dinish, J. Aguirre, R. Bi, K. Dev, A.B.E. Attia, S. Nitkunanantharajah, Q. H. Lim, M. Schwarz, Y.W. Yew, Optoacoustic mesoscopy analysis and quantitative estimation of specific imaging metrics in Fitzpatrick skin phototypes II to V, *J. Biophotonics* 12 (9) (2019), e201800442.
- [137] Y.W. Yew, U. Dinish, E.C.E. Choi, R. Bi, C.J.H. Ho, K. Dev, X. Li, A.B.E. Attia, M.K. Wong, G. Balasundaram, Investigation of morphological, vascular and biochemical changes in the skin of an atopic dermatitis (AD) patient in response to dupilumab using raster scanning optoacoustic mesoscopy (RSOM) and handheld confocal Raman spectroscopy (CRS), *J. Dermatol. Sci.* 95 (3) (2019) 123–125.
- [138] S. Chuah, A. Attia, V. Long, C. Ho, P. Malempati, C. Fu, S. Ford, J. Lee, W. Tan, D. Razansky, Structural and functional 3D mapping of skin tumours with non-invasive multispectral optoacoustic tomography, *Ski. Res. Technol.* 23 (2) (2017) 221–226.
- [139] M. Schwarz, A. Buehler, J. Aguirre, V. Ntziachristos, Three-dimensional multispectral optoacoustic mesoscopy reveals melanin and blood oxygenation in human skin in vivo, *J. Biophotonics* 9 (1–2) (2016) 55–60.
- [140] A. Hariri, C. Moore, Y. Mantri, J.V. Jokerst, Photoacoustic imaging as a tool for assessing hair follicular organization, *Sensors* 20 (20) (2020) 5848.
- [141] K.E. Kadler, C. Baldock, J. Bella, R.P. Boot-Handford, Collagens at a glance, *J. Cell Sci.* 120 (12) (2007) 1955–1958.
- [142] A.P. Regensburger, L.M. Fonteyne, J. Jungert, A.L. Wagner, T. Gerhalter, A. M. Nagel, R. Heiss, F. Flenkenthaler, M. Qurashi, M.F. Neurath, N. Klymiuk, E. Kemter, T. Frohlich, M. Uder, J. Woelfle, W. Rascher, R. Trollmann, E. Wolf, M. J. Waldner, F. Knieling, Detection of collagens by multispectral optoacoustic tomography as an imaging biomarker for Duchenne muscular dystrophy, *Nat. Med.* 25 (12) (2019) 1905–1915.
- [143] S. Sethuraman, J.H. Amirian, S.H. Litovsky, R.W. Smalling, S.Y. Emelianov, Spectroscopic intravascular photoacoustic imaging to differentiate atherosclerotic plaques, *Opt. Express* 16 (5) (2008) 3362–3367.
- [144] K. Jansen, M. Wu, A.F. van der Steen, G. van Soest, Photoacoustic imaging of human coronary atherosclerosis in two spectral bands, *Photoacoustics* 2 (1) (2014) 12–20.
- [145] J.M. Seeger, E. Barratt, G.A. Lawson, N. Klingman, The relationship between carotid plaque composition, plaque morphology, and neurologic symptoms, *J. Surg. Res* 58 (3) (1995) 330–336.
- [146] P. Wang, P. Wang, H.W. Wang, J.X. Cheng, Mapping lipid and collagen by multispectral photoacoustic imaging of chemical bond vibration, *J. Biomed. Opt.* 17 (9) (2012).
- [147] N. Chalasani, Z. Younossi, J.E. Lavine, A.M. Diehl, E.M. Brunt, K. Cusi, M. Charlton, A.J. Sanyal, A. American Gastroenterological, D. American Association for the Study of Liver, G. American College of, The diagnosis and management of non-alcoholic fatty liver disease: practice guideline by the American Gastroenterological Association, American Association for the Study of Liver Diseases, and American College of Gastroenterology, *Gastroenterology* 142(7) (2012) 1592–609.
- [148] G. Xu, Z.X. Meng, J.D. Lin, C.X. Deng, P.L. Carson, J.B. Fowlkes, C. Tao, X.J. Liu, X.D. Wang, High Resolution Physio-chemical Tissue Analysis: Towards Noninvasive In Vivo Biopsy, *Sci. Rep.* 6 (2016).
- [149] O. Rom, G. Xu, Y. Guo, Y. Zhu, H. Wang, J. Zhang, Y. Fan, W. Liang, H. Lu, Y. Liu, Nitro-fatty acids protect against steatosis and fibrosis during development of nonalcoholic fatty liver disease in mice, *EBioMedicine* 41 (2019) 62–72.
- [150] R. Pugatsch, D. Elad, A.J. Jaffa, O. Eytan, Analysis of cervical dynamics by ultrasound imaging, *Ann. N. Y. Acad. Sci.* 1101 (2007) 203–214.
- [151] K. Yoshida, H. Jiang, M. Kim, J. Vink, S. Creemers, D. Paik, R. Wapner, M. Mahendroo, K. Myers, Quantitative evaluation of collagen crosslinks and corresponding tensile mechanical properties in mouse cervical tissue during normal pregnancy, *PLoS One* 9 (11) (2014), e112391.
- [152] M.M. Maurer, S. Badir, M. Pensalfini, M. Bajka, P. Abitabile, R. Zimmermann, E. Mazza, Challenging the in-vivo assessment of biomechanical properties of the uterine cervix: a critical analysis of ultrasound based quasi-static procedures, *J. Biomech.* 48 (9) (2015) 1541–1548.
- [153] S.M. Yellon, Contributions to the dynamics of cervix remodeling prior to term and preterm birth, *Biol. Reprod.* 96 (1) (2017) 13–23.
- [154] H.F. Andersen, C.E. Nugent, S.D. Wanty, R.H. Hayashi, Prediction of risk for preterm delivery by ultrasonographic measurement of cervical length, *Am. J. Obstet. Gynecol.* 163 (3) (1990) 859–867.
- [155] Z. Xu, C. Li, L.V. Wang, Photoacoustic tomography of water in phantoms and tissue, *J. Biomed. Opt.* 15 (3) (2010), 036019.
- [156] S.K.V. Sekar, I. Bargigia, A.D. Mora, P. Taroni, A. Ruggeri, A. Tosi, A. Pifferi, A. Farina, Diffuse optical characterization of collagen absorption from 500 to 1700 nm, *J. Biomed. Opt.* 22 (1) (2017).
- [157] Y. Yan, N. Gomez-Lopez, M. Basij, A.V. Shahvari, F. Vadillo-Ortega, E. Hernandez-Andrade, S.S. Hassan, R. Romero, M. MehrMohammadi, Photoacoustic imaging of the uterine cervix to assess collagen and water content changes in murine pregnancy, *Biomed. Opt. Express* 10 (9) (2019) 4643–4655.
- [158] Y. Yan, M. Basij, A. Garg, A. Varrey, A. Alhousseini, R. Hsu, E. Hernandez-Andrade, R. Romero, S.S. Hassan, M. Mehrmohammadi, Spectroscopic photoacoustic imaging of cervical tissue composition in excised human samples, *PLoS One* 16 (3) (2021), e0247385.
- [159] A. Varrey, M. Mehrmohammadi, A. Garg, F. Qureshi, Y. Yan, M. Basij, A. Siddiqui, A. Alhousseini, N. Gomez-Lopez, R. Romero, S. Hassan, Photoacoustic imaging of the uterine cervix: a novel method to characterize tissue composition, *Am. J. Obstet. Gynecol.* 220 (1) (2019) S14–S15.
- [160] Y. Qu, P. Hu, J.H. Shi, K. Maslov, P.N. Zhao, C.Y. Li, J. Ma, A. Garcia-Urbe, K. Meyers, E. Diveley, S. Pizzella, L. Muench, N. Punyamurthy, N. Goldstein, O. Onwumere, M. Alisio, K. Meyenburg, J. Maynard, K. Helm, E. Altieri, J. Slaughter, S. Barber, T. Burger, C. Kramer, J. Chubiz, M. Anderson, R. McCarthy, S.K. England, G.A. Macones, M.J. Stout, M. Tuuli, L.H.V. Wang, In vivo characterization of connective tissue remodeling using infrared photoacoustic spectra, *J. Biomed. Opt.* 23 (12) (2018), 121621.
- [161] M. Bonora, S. Patergnani, A. Rimessi, E. De Marchi, J.M. Suski, A. Bononi, C. Giorgi, S. Marchi, S. Missiroli, F. Poletti, M.R. Wiekowski, P. Pinton, ATP synthesis and storage, *Purinergic Signal* 8 (3) (2012) 343–357.
- [162] Z. Suba, M. Ujjál, Disorders of glucose metabolism and risk of oral cancer, *Fogorv. Szle.* 100 (5) (2007) 250–257.
- [163] K. Matz, K. Keresztes, C. Tatschl, M. Nowotny, A. Dachenhausen, M. Brainin, J. Tuomilehto, Disorders of glucose metabolism in acute stroke patients: an underrecognized problem, *Diabetes Care* 29 (4) (2006) 792–797.
- [164] W. Dinh, R. Futh, W. Nickl, T. Krahn, P. Ellinghaus, T. Scheffold, L. Bansemir, A. Bufo, M.C. Barroso, M. Lankisch, Elevated plasma levels of TNF-alpha and interleukin-6 in patients with diastolic dysfunction and glucose metabolism disorders, *Cardiovasc. Diabetol.* 8 (1) (2009) 58.
- [165] A.G. Bertoni, J.S. Krop, G.F. Anderson, F.L. Brancati, Diabetes-related morbidity and mortality in a national sample of US elders, *Diabetes Care* 25 (3) (2002) 471–475.
- [166] P.V. Roder, B. Wu, Y. Liu, W. Han, Pancreatic regulation of glucose homeostasis, *Exp. Mol. Med* 48 (2016), e219.
- [167] C. Diabetes, G. Complications Trial Research, D.M. Nathan, S. Genuth, J. Lachin, P. Cleary, O. Crofford, M. Davis, L. Rand, C. Siebert, The effect of intensive treatment of diabetes on the development and progression of long-term complications in insulin-dependent diabetes mellitus, in: *N Engl J Med*, 329, 1993, pp. 977–986.
- [168] C.M. Díaz-García, C. Lahmann, J.R. Martínez-François, B. Li, D. Koveal, N. Nathwani, M. Rahman, J.P. Keller, J.S. Marvin, L.L. Looger, G. Yellen, Quantitative in vivo imaging of neuronal glucose concentrations with a genetically encoded fluorescence lifetime sensor, *J. Neurosci. Res.* 97 (8) (2019) 946–960.
- [169] R.J. Russell, M.V. Pishko, C.C. Gefrides, M.J. McShane, G.L. Cote, A fluorescence-based glucose biosensor using concanavalin A and dextran encapsulated in a poly (ethylene glycol) hydrogel, *Anal. Chem.* 71 (15) (1999) 3126–3132.
- [170] M.A. Pleitez, T. Lieblein, A. Bauer, O. Hertzberg, H. von Lilienfeld-Toal, W. Mantele, In vivo noninvasive monitoring of glucose concentration in human epidermis by mid-infrared pulsed photoacoustic spectroscopy, *Anal. Chem.* 85 (2) (2013) 1013–1020.

- [171] J. Kottmann, J.M. Rey, J. Luginbuhl, E. Reichmann, M.W. Sigrist, Glucose sensing in human epidermis using mid-infrared photoacoustic detection, *Biomed. Opt. Express* 3 (4) (2012) 667–680.
- [172] E. Alarousu, J. Hast, M. Kinnunen, M. Kirillin, R. Myllyla, J. Plucinski, A. Popov, A. Priezzhev, T. Prykari, J. Saarela, Z. Zuomin, Non-invasive glucose sensing in scattering media using OCT, PAS and TOF techniques, *Saratov Fall Meeting 2003: Optical Technologies in Biophysics and Medicine V 5474* (2004) 33–41.
- [173] M.J. Goetz, G.L. Cote, R. Erckens, W. March, M. Motamedi, Application of a multivariate technique to raman-spectra for quantification of body chemicals, *IEEE T Bio-Med. Eng.* 42 (7) (1995) 728–731.
- [174] S.T. Pan, H. Chung, M.A. Arnold, G.W. Small, Near-infrared spectroscopic measurement of physiological glucose levels in variable matrices of protein and triglycerides, *Anal. Chem.* 68 (7) (1996) 1124–1135.
- [175] M. Kohl, M. Cope, M. Essenpreis, D. Bocker, Influence of glucose-concentration on light-scattering in tissue-simulating phantoms, *Opt. Lett.* 19 (24) (1994) 2170–2172.
- [176] J.Y. Sim, C.G. Ahn, E.J. Jeong, B.K. Kim, In vivo microscopic photoacoustic spectroscopy for non-invasive glucose monitoring invulnerable to skin secretion products, *Sci. Rep.* 8 (1) (2018) 1059.
- [177] H.S. Ashton, H.A. MacKenzie, P. Rae, Y.C. Shen, S. Spiers, J. Lindberg, Blood glucose measurements by photoacoustics, *Aip Conf. Proc.* 463 (1999) 570–572.
- [178] G. Spanner, R. Niessner, New concept for the non-invasive determination of physiological glucose concentrations using modulated laser diodes, *Fresen J. Anal. Chem.* 354 (3) (1996) 306–310.
- [179] P.P. Pai, P.K. Sanki, S. Sarangi, S. Banerjee, Modelling, verification, and calibration of a photoacoustics based continuous non-invasive blood glucose monitoring system, *Rev. Sci. Instrum.* 86 (6) (2015).
- [180] J. Kottmann, J.M. Rey, M.W. Sigrist, Mid-infrared photoacoustic detection of glucose in human skin: towards non-invasive diagnostics, *Sensors* 16 (10) (2016) 1663.
- [181] T.M. Peters, Image-guidance for surgical procedures, *Phys. Med. Biol.* 51 (14) (2006) R505.
- [182] Y. Yan, S. John, M. Ghalehnovi, L. Kabbani, N.A. Kennedy, M. Mehrmohammadi, Ultrasound and photoacoustic imaging for enhanced image-guided endovenous laser ablation procedures, *Medical Imaging 2018: Ultrasonic Imaging and Tomography*, *Int. Soc. Opt. Photonics* (2018) 105800T.
- [183] G. Reusz, P. Sarkany, J. Gal, A. Csomos, Needle-related ultrasound artifacts and their importance in anaesthetic practice, *Br. J. Anaesth.* 112 (5) (2014) 794–802.
- [184] M. Ziskin, D. Thickman, N. Goldenberg, M. Lapayowker, J. Becker, The comet tail artifact, *J. Ultrasound Med.* 1 (1) (1982) 1–7.
- [185] S. John, V. Yan, L. Kabbani, N.A. Kennedy, M. Mehrmohammadi, Integration of Endovenous Laser Ablation and Photoacoustic Imaging Systems for Enhanced Treatment of Venous Insufficiency, 2018 IEEE International Ultrasonics Symposium (IUS), IEEE, 2018, pp. 1–4.
- [186] C. Kim, T.N. Erpelding, K.I. Maslov, L. Jankovic, W.J. Akers, L. Song, S. Achilefu, J.A. Margenthaler, M.D. Pashley, L.V. Wang, Handheld array-based photoacoustic probe for guiding needle biopsy of sentinel lymph nodes, *J. Biomed. Opt.* 15 (4) (2010), 046010.
- [187] E. Caturelli, L. Solmi, M. Anti, S. Fusilli, P. Roselli, A. Andriulli, F. Fornari, C.D. V. Blanco, I. De. Sio, Ultrasound guided fine needle biopsy of early hepatocellular carcinoma complicating liver cirrhosis: a multicentre study, *Gut* 53 (9) (2004) 1356–1362.
- [188] S. Natarajan, L.S. Marks, D.J. Margolis, J. Huang, M.L. Macairan, P. Lieu, A. Fenster, Clinical application of a 3D ultrasound-guided prostate biopsy system. *Urologic oncology: seminars and original investigations*, Elsevier, 2011, pp. 334–342.
- [189] G. Sauer, H. Deissler, K. Strunz, G. Helms, E. Remmel, K. Koretz, R. Terinde, R. Kreinberg, Ultrasound-guided large-core needle biopsies of breast lesions: analysis of 962 cases to determine the number of samples for reliable tumour classification, *Br. J. Cancer* 92 (2) (2005) 231.
- [190] M. Bonatti, N. Vezzali, F. Lombardo, F. Ferro, G. Zamboni, M. Tauber, G. Bonatti, Gallbladder adenomyomatosis: imaging findings, tricks and pitfalls, *Insights Imaging* 8 (2) (2017) 243–253.
- [191] J. Perrault, D.B. McGill, B.J. Ott, W.F. Taylor, Liver biopsy: complications in 1000 inpatients and outpatients, *Gastroenterology* 74 (1) (1978) 103–106.
- [192] F. Piccinino, E. Sagnelli, G. Pasquale, G. Giusti, A. Battocchia, M. Bernardi, R. Bertolazzi, F. Bianchi, E. Brunelli, G. Budillon, Complications following percutaneous liver biopsy: a multicentre retrospective study on 68 276 biopsies, *J. Hepatol.* 2 (2) (1986) 165–173.
- [193] M. Shi, T. Zhao, S.J. West, A.E. Desjardins, T. Vercauteren, W. Xia, Improving needle visibility in LED-based photoacoustic imaging using deep learning with semi-synthetic datasets, *Photoacoustics* 26 (2022), 100351.
- [194] K. Watanabe, J. Tokumine, A.K. Lefor, H. Nakazawa, K. Yamamoto, H. Karasawa, M. Nagase, T. Yorozu, Photoacoustic needle improves needle tip visibility during deep peripheral nerve block, *Sci. Rep.* 11 (1) (2021) 8432.
- [195] H. Wang, S. Liu, T. Wang, C. Zhang, T. Feng, C. Tian, Three-dimensional interventional photoacoustic imaging for biopsy needle guidance with a linear array transducer, *J. Biophotonics* 12 (12) (2019), e201900212.
- [196] J. Su, A. Karpouk, B. Wang, S. Emelianov, Photoacoustic imaging of clinical metal needles in tissue, *J. Biomed. Opt.* 15 (2) (2010), 021309.
- [197] M.A. Lediju Bell, J. Shubert, Photoacoustic-based visual servoing of a needle tip, *Sci. Rep.* 8 (1) (2018) 15519.
- [198] K. Sivasubramanian, V. Periyasamy, M. Pramanik, Non-invasive sentinel lymph node mapping and needle guidance using clinical handheld photoacoustic imaging system in small animal, *J. Biophotonics* 11 (1) (2018), e201700061.
- [199] H. Moradi, S. Tang, S.E. Salcudean, Toward intra-operative prostate photoacoustic imaging: configuration evaluation and implementation using the da Vinci research kit, *IEEE Trans. Med. Imaging* 38 (1) (2018) 57–68.
- [200] N. Gandhi, M. Allard, S. Kim, P. Kazanzides, M. Lediju Bell, Photoacoustic-based approach to surgical guidance performed with and without a da Vinci robot, *J. Biomed. Opt.* 22 (12) (2017), 121606.
- [201] M.A.L. Bell, A.K. Ostrowski, K. Li, P. Kazanzides, E.M. Bector, Localization of transcranial targets for photoacoustic-guided endonasal surgeries, *Photoacoustics* 3 (2) (2015) 78–87.
- [202] M. Graham, F. Assis, D. Allman, A. Wiacek, E. Gonzalez, M. Gubbi, J. Dong, H. Hou, S. Beck, J. Chrispin, M.A.L. Bell, In vivo demonstration of photoacoustic image guidance and robotic visual servoing for cardiac catheter-based interventions, *IEEE Trans. Med. Imaging* 39 (4) (2020) 1015–1029.
- [203] L. Zhu, Y. Zhao, Y. Shen, F. Gao, L. Liu, F. Gao, Photoacoustic Characterization of Cortical and Cancellous Bone in The Vertebrae, 2021 43rd Annual International Conference of the IEEE Engineering in Medicine & Biology Society (EMBC), 2021, pp. 294–297.
- [204] J. Shubert, M.A. Lediju Bell, Photoacoustic imaging of a human vertebra: implications for guiding spinal fusion surgeries, *Phys. Med. amp; Biol.* 63 (14) (2018), 144001.
- [205] E.A. Gonzalez, A. Jain, M.A.L. Bell, Combined ultrasound and photoacoustic image guidance of spinal pedicle cannulation demonstrated with intact ex vivo specimens, *IEEE T Bio-Med. Eng.* 68 (8) (2021) 2479–2489.
- [206] Y. Yan, S. John, M. Ghalehnovi, L. Kabbani, N.A. Kennedy, M. Mehrmohammadi, Photoacoustic imaging for image-guided endovenous laser ablation procedures, *Sci. Rep.* 9 (1) (2019) 2933.
- [207] M. Basij, S. John, D. Bustamante, L. Kabbani, V. Maskoun, M. Mehrmohammadi, Integrated ultrasound and photoacoustic-guided laser ablation theranostic endoscopic system, *IEEE T Bio-Med Eng.* (2022) 1–9.
- [208] H. Kruit, K. Joseph Francis, E. Rascevska, S. Manohar, Annular fiber probe for interstitial illumination in photoacoustic guidance of radiofrequency ablation, *Sensors* (2021).
- [209] T.F. Fehm, X.L. Deán-Ben, P. Schaur, R. Sroka, D. Razansky, Volumetric photoacoustic imaging feedback during endovenous laser therapy – an ex vivo investigation, *J. Biophotonics* 9 (9) (2016) 934–941.
- [210] M.K. Singh, V. Parameshwarappa, E. Hendriksen, V. Steenberg, S. Manohar, Photoacoustic-guided focused ultrasound for accurate visualization of brachytherapy seeds with the photoacoustic needle, *J. Biomed Opt.* 21 (12) (2016), 120501.
- [211] M.A. Lediju Bell, N.P. Kuo, D.Y. Song, J.U. Kang, E.M. Bector, In vivo visualization of prostate brachytherapy seeds with photoacoustic imaging, *J. Biomed Opt* 19 (12) (2014) 126011. Dec.
- [212] B.R. Ecclestone, K. Bell, S. Abbasi, D. Dinakaran, F.K.H. van Landeghem, J. R. Mackey, P. Fieguth, P. Haji, Reza, Improving maximal safe brain tumor resection with photoacoustic remote sensing microscopy, *Sci. Rep.* 10 (1) (2020) 17211.
- [213] S. Abbasi, M. Le, B. Sonier, D. Dinakaran, G. Bigras, K. Bell, J.R. Mackey, P. Haji Reza, All-optical Reflection-mode Microscopic Histology of Unstained Human Tissues, *Sci. Rep.* 9 (1) (2019) 13392.
- [214] B.S. Restall, B.D. Cikaluk, M.T. Martell, N.J.M. Haven, R. Mittal, S. Silverman, L. Peiris, J. Deschenes, B.A. Adam, A. Kinnaird, R.J. Zemp, Fast hybrid optomechanical scanning photoacoustic remote sensing microscopy for virtual histology, *Biomed. Opt. Express* 13 (1) (2022) 39–47.
- [215] Y. Yan, W. Jing, M. Mehrmohammadi, Photoacoustic imaging to track magnetic-manipulated micro-robots in deep tissue, *Sensors* 20 (10) (2020) 2816.
- [216] D. Piras, C. Grijsen, P. Schutte, W. Steenberg, S. Manohar, Photoacoustic needle: minimally invasive guidance to biopsy, *J. Biomed. Opt.* 18 (7) (2013), 070502.
- [217] M. Allard, J. Shubert, M.A.L. Bell, Feasibility of photoacoustic-guided teleoperated hysterectomies, *J. Med. Imaging* 5 (2) (2018), 021213.
- [218] J.L. Su, B. Wang, S.Y. Emelianov, Photoacoustic imaging of coronary artery stents, *Opt. Express* 17 (22) (2009) 19894–19901.
- [219] T.T. Wong, R. Zhang, P. Hai, C. Zhang, M.A. Pleitez, R.L. Aft, D.V. Novack, L. V. Wang, Fast label-free multilayered histology-like imaging of human breast cancer by photoacoustic microscopy, *Sci. Adv.* 3 (5) (2017), e1602168.
- [220] S. John, Y. Yan, T. Shaik, L. Kabbani, M. Mehrmohammadi, Photoacoustic Guided Endovenous Laser Ablation: Calibration and In Vivo Canine Studies, 2020 IEEE International Ultrasonics Symposium (IUS), IEEE, 2020, pp. 1–4.
- [221] M.A.L. Bell, X. Guo, D.Y. Song, E.M. Bector, Transurethral light delivery for prostate photoacoustic imaging, *J. Biomed. Opt.* 20 (3) (2015), 036002.
- [222] Y. Yan, M. Mehrmohammadi, W. Jing, Non-invasive Photoacoustic Imaging of Magnetic Micro-robot through Deep Non-Transparent Tissue, 2020 International Conference on Manipulation, Automation and Robotics at Small Scales (MARSS), IEEE, 2020, pp. 1–6.
- [223] J. Shubert, M.A.L. Bell, A novel drill design for photoacoustic guided surgeries, *Photons Plus Ultrasound: Imaging and Sensing 2018*, *Int. Soc. Opt. Photonics* (2018) 104940J.
- [224] B.M. Boszczyk, M. Bierschneider, S. Panzer, et al., Fluoroscopic radiation exposure of the kyphoplasty patient, *Eur Spine J* 15 (2006) 347–355.
- [225] H.C. Choi, Fluoroscopic Radiation Exposure during Percutaneous Kyphoplasty, *J. Korean Neurosurgical Soc.* 49 (1) (2011) 37–42. Jan.
- [226] D.A. Tyndall, J.B. Price, S. Tetradis, S.D. Ganz, C. Hildebolt, W.C. Scarfe, Position statement of the American Academy of Oral and Maxillofacial Radiology on selection criteria for the use of radiology in dental implantology with emphasis on cone beam computed tomography, *Oral Surgery, Oral Medicine, Oral Pathol. Oral. Radiol.* 113 (6) (2012) 817–826.

- [227] D. Lee, S. Park, C. Kim, Dual-modal photoacoustic and ultrasound imaging of dental implants, *Photons Plus Ultrasound: Imaging and Sensing 2018*, Int. Soc. Opt. Photonics (2018) 104940B.
- [228] Jr Hug, E. Nagel, A. Bornstedt, B. Schnackenburg, H. Oswald, E. Fleck, Coronary arterial stents: safety and artifacts during MR imaging, *Radiology* 216 (3) (2000) 781–787.
- [229] D. Maintz, R.M. Botnar, R. Fischbach, W. Heindel, W.J. Manning, M. Stuber, Coronary magnetic resonance angiography for assessment of the stent lumen: a phantom study, *J. Cardiovasc. Magn. Reson.* 4 (3) (2002) 359–367.
- [230] Y. Kawase, K. Hoshino, R. Yoneyama, J. McGregor, R.J. Hajjar, I.-K. Jang, M. Hayase, In vivo volumetric analysis of coronary stent using optical coherence tomography with a novel balloon occlusion-flushing catheter: a comparison with intravascular ultrasound, *Ultrasound Med. Biol.* 31 (10) (2005) 1343–1349.
- [231] T.L.P. Slottow, R. Pakala, T. Okabe, D. Hellinga, R.J. Lovce, F.O. Tio, A.B. Bui, R. Waksman, Optical coherence tomography and intravascular ultrasound imaging of bioabsorbable magnesium stent degradation in porcine coronary arteries, *Cardiovascular Revascularization, Medicine* 9 (4) (2008) 248–254.
- [232] P. Barlis, K. Dimopoulos, J. Tanigawa, E. Dzielicka, G. Ferrante, F. Del Furia, C. Di, Mario, Quantitative analysis of intracoronary optical coherence tomography measurements of stent strut apposition and tissue coverage, *Int. J. Cardiol.* 141 (2) (2010) 151–156.
- [233] I.H. Kunkler, L.J. Williams, W.J.L. Jack, D.A. Cameron, J.M. Dixon, Breast-Conserving Surgery with or without Irradiation in Early Breast Cancer, *N Engl J Med* 388 (7) (2023) 585–594.
- [234] J.Q. Brown, T.M. Bydlon, L.M. Richards, B. Yu, S.A. Kennedy, J. Geradts, L. G. Wilke, M. Junker, J. Gallagher, W. Barry, N. Ramanujam, Optical assessment of tumor resection margins in the breast, *IEEE J. Sel. Top. Quantum Electron* 16 (3) (2010) 530–544.
- [235] I.J. Bigio, S.G. Bown, G.M. Briggs, C. Kelley, S. Lakhani, D.C.O. Pickard, P. M. Ripley, I. Rose, C. Saunders, Diagnosis of breast cancer using elastic-scattering spectroscopy: preliminary clinical results, *J. Biomed. Opt.* 5 (2) (2000) 221–229.
- [236] A.S. Haka, Z. Volynskaya, J.A. Gardecki, J. Nazemi, J. Lyons, D. Hicks, M. Fitzmaurice, R.R. Dasari, J.P. Crowe, M.S. Feld, In vivo margin assessment during partial mastectomy breast surgery using Raman spectroscopy, *Cancer Res.* 66 (6) (2006) 3317–3322.
- [237] K.E. Peyer, L. Zhang, B.J. Nelson, Bio-inspired magnetic swimming microrobots for biomedical applications, *Nanoscale* 5 (4) (2013) 1259–1272.
- [238] S.Y. Emelianov, P.-C. Li, M. O'Donnell, Photoacoustics for molecular imaging and therapy, *Phys. Today* 62 (8) (2009) 34–39.
- [239] D.-K. Yao, K. Maslov, K.K. Shung, Q. Zhou, L.V. Wang, In vivo label-free photoacoustic microscopy of cell nuclei by excitation of DNA and RNA, *Opt. Lett.* 35 (24) (2010) 4139–4141.
- [240] S. John, Y. Yan, S.Y. Forta, L. Kabbani, M. Mehrmohammadi, Integrated ultrasound and photoacoustic imaging for effective endovenous laser ablation: a characterization study, 2019 IEEE International Ultrasonics Symposium (IUS), IEEE, 2019, pp. 122–125.
- [241] C. Chargari, E. Deutsch, P. Blanchard, S. Gouy, H. Martelli, F. Guerin, I. Dumas, A. Bossi, P. Morice, A.N. Viswanathan, C. Haie-Meder, Brachytherapy: an overview for clinicians, *CA Cancer J. Clin.* 69 (5) (2019) 386–401.
- [242] J.H. Suh, G.H. Barnett, Brachytherapy for brain tumor, *Hematol Oncol Clin North Am* 13 (3) (1999) 635–650. Jun.
- [243] J. Skowronek, Brachytherapy in the treatment of skin cancer: an overview, *Postepy Dermatol Alergol* 32 (5) (2015) 362–367. Oct.
- [244] D.B. Fuller, J.A. Kozioł, A.C. Feng, Prostate brachytherapy seed migration and dosimetry: analysis of stranded sources and other potential predictive factors, *Brachytherapy* 3 (1) (2004) 10–19.
- [245] F.M. Waterman, N. Yue, B.W. Corn, A.P. Dicker, Edema associated with I-125 or Pd-103 prostate brachytherapy and its impact on post-implant dosimetry: an analysis based on serial CT acquisition, *Int. J. Radiat. Oncol. *Biol. *Phys.* 41 (5) (1998) 1069–1077.
- [246] Y. Yu, T.K. Podder, Y.D. Zhang, W.S. Ng, V. Mistic, J. Sherman, D. Fuller, D. J. Rubens, J.G. Strang, R.A. Brasacchio, E.M. Messing, Robotic system for prostate brachytherapy, *Comput. Aided Surg.* 12 (6) (2007) 366–370.
- [247] A. Polo, C. Salembier, J. Venselaar, P. Hoskin, PgtG. ESTRO, Review of intraoperative imaging and planning techniques in permanent seed prostate brachytherapy, *Radiother. Oncol.* 94 (1) (2010) 12–23.
- [248] K.K. Win, J. Wang, C. Zhang, Y. Ran, Identification and removal of reverberation in ultrasound imaging, 2010 5th IEEE Conference on Industrial Electronics and Applications, 2010, pp. 1675–1680.
- [249] J. Ricke, P. Wust, Computed tomography-guided brachytherapy for liver cancer, *Semin Radiat Oncol* 21 (4) (2011) 287–293. Oct.
- [250] S. Jeon, J. Kim, D. Lee, J.W. Baik, C. Kim, Review on practical photoacoustic microscopy, *Photoacoustics* 15 (2019), 100141.
- [251] P. Hajireza, W. Shi, K. Bell, R.J. Paproski, R.J. Zemp, Non-interferometric photoacoustic remote sensing microscopy, *Light Sci. Appl.* 6 (6) (2017), e16278.
- [252] F.J.O. Landa, C. Özsoy, X.L. Deán-Ben, D. Razansky, Optoacoustic monitoring of RF ablation lesion progression. *Photons Plus Ultrasound: Imaging and Sensing 2019*, Spie., 2019, pp. 198–204.
- [253] A.A. Oraevsky, R.O. Esenaliev, M. Motamedi, A.A. Karabutov, Real time optoacoustic monitoring of changes in tissue properties, Google Patents, 2001.
- [254] I.V. Larina, K.V. Larin, R.O. Esenaliev, Real-time optoacoustic monitoring of temperature in tissues, *J. Phys. D. Appl. Phys.* 38 (15) (2005) 2633–2639.
- [255] Q. Peng, A. Juzeniene, J. Chen, L.O. Svaasand, T. Warloe, K.E. Giercksky, J. Moan, Lasers in medicine, *Repr. Prog. Phys.* 71 (5) (2008), 056701.
- [256] Y. Zhou, M. Li, W. Liu, G. Sankin, J. Luo, P. Zhong, J. Yao, Thermal memory based photoacoustic imaging of temperature, *Optica* 6 (2) (2019) 198–205.
- [257] M.D. Andrews, Cryosurgery for common skin conditions, *Am. Fam. Physician* 69 (10) (2004).
- [258] T. Klimentko, S. Ahvenainen, S.-L. Karvonen, Whole-body cryotherapy in atopic dermatitis, *Arch. Dermatol.* 144 (6) (2008) 806–808.
- [259] E. Petrova, A. Liopo, V. Nadvoretzkiy, S. Ermilov, Imaging technique for real-time temperature monitoring during cryotherapy of lesions, *J. Biomed. Opt.* 21 (11) (2016), 116007.
- [260] B. Maytal, Fast Joule-Thomson cryocycling device for cryosurgical applications. *Advances in Cryogenic Engineering*, Springer, 1998, pp. 911–917.
- [261] D. Rukstalis, A.E. Katz, Handbook of urologic cryoablation, CRC Press, 2007.
- [262] Y.-S. Hsiao, C.X. Deng, Calibration and evaluation of ultrasound thermography using infrared imaging, *Ultrasound Med. Biol.* 42 (2) (2016) 503–517.
- [263] E.V. Petrova, A.A. Oraevsky, S.A. Ermilov, Red blood cell as a universal optoacoustic sensor for non-invasive temperature monitoring, *Appl. Phys. Lett.* 105 (9) (2014), 094103.
- [264] E. Petrova, H. Brecht, M. Motamedi, A. Oraevsky, S. Ermilov, In vivo optoacoustic temperature imaging for image-guided cryotherapy of prostate cancer, *Phys. Med. Biol.* 63 (6) (2018), 064002.
- [265] F.J.O. Landa, S.R. Penacoba, F.M. de Espinosa, D. Razansky, X.L. Deán-Ben, Four-dimensional optoacoustic monitoring of tissue heating with medium intensity focused ultrasound, *Ultrasonics* 94 (2019) 117–123.
- [266] P. Rai, S. Mallidi, X. Zheng, R. Rahmzadeh, Y. Mir, S. Elrington, A. Khurshid, T. Hasan, Development and applications of photo-triggered theranostic agents, *Adv. Drug Deliv. Rev.* 62 (11) (2010) 1094–1124.
- [267] N. Dana, L. Di Biase, A. Natale, S. Emelianov, R. Bouchard, In vitro photoacoustic visualization of myocardial ablation lesions, *Heart Rhythm* 11 (1) (2014) 150–157.
- [268] D.L. Miller, N.B. Smith, M.R. Bailey, G.J. Czarnota, K. Hynynen, I.R.S. Makin, B.C. o.t.a.I.o.U.i. Medicine, Overview of therapeutic ultrasound applications and safety considerations, *J. Ultrasound Med.* 31 (4) (2012) 623–634.
- [269] G. ter Haar, Heat and sound: Focused ultrasound in the clinic, *Int. J. Hyperther.* 31 (2015) 223–224.
- [270] J.C. Rewcastle, High intensity focused ultrasound for prostate cancer: a review of the scientific foundation, technology and clinical outcomes, *Technol. Cancer Res. Treat.* 5 (6) (2006) 619–625.
- [271] J. Kennedy, F. Wu, G. Ter Haar, F. Gleeson, R. Phillips, M. Middleton, D. Cranston, High-intensity focused ultrasound for the treatment of liver tumours, *Ultrasonics* 42 (1–9) (2004) 931–935.
- [272] C. Damianou, K. Ioannides, V. Hadjisavvas, N. Mylonas, A. Couppis, D. Iosif, In vitro and in vivo brain ablation created by high-intensity focused ultrasound and monitored by MRI, *IEEE Trans. Ultrason., Ferroelectr., Freq. Control* 56 (6) (2009) 1189–1198.
- [273] K. Hynynen, O. Pomeroy, D.N. Smith, P.E. Huber, N.J. McDannold, J. Kettenbach, J. Baum, S. Singer, F.A. Jolesz, MR imaging-guided focused ultrasound surgery of fibroadenomas in the breast: a feasibility study, *Radiology* 219 (1) (2001) 176–185.
- [274] H. Cui, J. Staley, X. Yang, Integration of photoacoustic imaging and high-intensity focused ultrasound, *J. Biomed. Opt.* 15 (2) (2010), 021312.
- [275] F.J.O. Landa, S.R. Penacoba, X.L. Deán-Ben, F.M. de Espinosa, D. Razansky, Monitoring of tissue heating with medium intensity focused ultrasound via four dimensional optoacoustic tomography, *Photons Plus Ultrasound: Imaging and Sensing 2018*, Int. Soc. Opt. Photonics (2018) 104945J.
- [276] R.R. Van Den Bos, M. Neumann, K.P.D.E. ROOS, T. Nijsten, Endovenous laser ablation-induced complications: review of the literature and new cases, *Dermatol. Surg.* 35 (8) (2009) 1206–1214.
- [277] W. Malskat, M. Stokbroekx, C. van der Geld, T. Nijsten, R. Van, den Bos, Temperature profiles of 980- and 1,470-nm endovenous laser ablation, endovenous radiofrequency ablation and endovenous steam ablation, *Lasers Med. Sci.* 29 (2) (2014) 423–429.
- [278] M.P.S. Group, Laser photocoagulation of subfoveal recurrent neovascular lesions in age-related macular degeneration: results of a randomized clinical trial, *Arch. Ophthalmol.* 109 (9) (1991) 1232–1241.
- [279] J. Roeder, R. Brinkmann, C. Wirtelauer, H. Laqua, R. Birngruber, Subthreshold (retinal pigment epithelium) photocoagulation in macular diseases: a pilot study, *Br. J. Ophthalmol.* 84 (1) (2000) 40–47.
- [280] G. Schüle, G. Huttmann, C. Framme, J. Roeder, R. Brinkmann, Noninvasive optoacoustic temperature determination at the fundus of the eye during laser irradiation, *J. Biomed. Opt.* 9 (1) (2004) 173–180.
- [281] J. Shah, S. Park, S.R. Aglyamov, T. Larson, L. Ma, K.V. Sokolov, K.P. Johnston, T. E. Milner, S.Y. Emelianov, Photoacoustic imaging and temperature measurement for photothermal cancer therapy, *J. Biomed. Opt.* 13 (3) (2008), 034204.
- [282] Y. Zhang, X. Zhan, J. Xiong, S. Peng, W. Huang, R. Joshi, Y. Cai, Y. Liu, R. Li, K. Yuan, N. Zhou, W. Min, Temperature-dependent cell death patterns induced by functionalized gold nanoparticle photothermal therapy in melanoma cells, *Sci. Rep.* 8 (1) (2018) 8720.
- [283] H.-C. Huang, K. Rege, J.J. Heys, Spatiotemporal temperature distribution and cancer cell death in response to extracellular hyperthermia induced by gold nanorods, *ACS Nano* 4 (5) (2010) 2892–2900.
- [284] R. Tanimoto, T. Hiraiwa, Y. Nakai, Y. Shindo, K. Oka, N. Hiroi, A. Funahashi, Detection of temperature difference in neuronal cells, *Sci. Rep.* 6 (1) (2016) 22071.
- [285] F. Vetrone, R. Naccache, A. Zamarrón, A. Juarranz de la Fuente, F. Sanz-Rodríguez, L. Martínez Maestro, E. Martín Rodríguez, D. Jaque, J. García Sole, J. A. Capobianco, Temperature sensing using fluorescent nanothermometers, *ACS Nano* 4 (6) (2010) 3254–3258.

- [286] B. Quesson, J.A. de Zwart, C.T. Moonen, Magnetic resonance temperature imaging for guidance of thermotherapy, *J. Magn. Reson. Imaging: Off. J. Int. Soc. Magn. Reson. Med.* 12 (4) (2000) 525–533.
- [287] L.R. Hirsch, R.J. Stafford, J. Bankson, S.R. Sershen, B. Rivera, R. Price, J.D. Hazle, N.J. Halas, J.L. West, Nanoshell-mediated near-infrared thermal therapy of tumors under magnetic resonance guidance, *Proceedings of the National Academy of Sciences* 100(23) (2003) 13549–13554.
- [288] S. Aglyamov, S. Emelianov, J. Shah, K. Sokolov, T. Milner, Ultrasound-Based Thermal and Elasticity Imaging to Assist Photothermal Cancer Therapy—Preliminary Study, 2006 IEEE Ultrasonics Symposium, IEEE, 2006, pp. 1029–1032.
- [289] L. Zhang, M. Wang, F. Wu, L. Liu, X. Ren, Z. Hai, Intracellular Formation of Hemicyanine Nanoparticle Enhances Tumor-Targeting Photoacoustic Imaging and Photothermal Therapy, *Adv Healthc Mater* 12 (9) (2023), e2202676. Apr.
- [290] T.T.V. Phan, N.Q. Bui, S.-W. Cho, S. Bharathiraja, P. Manivasagan, M.S. Moorthy, S. Mondal, C.-S. Kim, J. Oh, Photoacoustic Imaging-Guided Photothermal Therapy with Tumor-Targeting HA-FeOOH@ PPy Nanorods, *Sci. Rep.* 8 (1) (2018) 8809.
- [291] A. Capart, K. Metwally, C. Bastiancich, A. Da Silva, Multiphysical numerical study of photothermal therapy of glioblastoma with photoacoustic temperature monitoring in a mouse head, *Biomed. Opt. Express* 13 (3) (2022) 1202–1223.
- [292] S. Sachdeva, A. Dogra, Radiofrequency ablation in dermatology, *Indian J. Dermatol.* 52 (3) (2007) 134.
- [293] M.-H. Chen, W. Yang, K. Yan, M.-W. Zou, L. Solbiati, J.-B. Liu, Y. Dai, Large liver tumors: protocol for radiofrequency ablation and its clinical application in 110 patients—mathematic model, overlapping mode, and electrode placement process, *Radiology* 232 (1) (2004) 260–271.
- [294] V. Nagaraja, A. Kalra, R. Puri, When to use intravascular ultrasound or optical coherence tomography during percutaneous coronary intervention? *Cardiovasc Diagn Ther* 10 (5) (2020) 1429–1444. Oct.
- [295] J. Rebling, F.J.O. Landa, X.L. Deán-Ben, D. Razansky, A new catheter design for combined radiofrequency ablation and optoacoustic treatment monitoring using copper-coated light-guides, *Optical Fibers and Sensors for Medical Diagnostics and Treatment Applications XVIII*, Int. Soc. Opt. Photonics (2018) 1048805.
- [296] M. Wright, E. Harks, S. Deladi, F. Suijver, M. Barley, A. van Dusschoten, S. Fokkenrood, F. Zuo, F. Sacher, M. Hocini, Real-time lesion assessment using a novel combined ultrasound and radiofrequency ablation catheter, *Heart Rhythm* 8 (2) (2011) 304–312.
- [297] M. Granier, P.F. Winum, M. Granier, P. Liaud, G. Cayla, P. Messner, J.-L. Pasquie, I. Schuster, Real-time atrial wall imaging during radiofrequency ablation in a porcine model, *Heart Rhythm* 12 (8) (2015) 1827–1835.
- [298] T. Szili-Torok, G.P. Kimman, D. Theuns, J. Roelandt, L. Jordaens, Visualisation of intra-cardiac structures and radiofrequency lesions using intracardiac echocardiography, *Eur. J. Echocardiogr.* 4 (1) (2003) 17–22.
- [299] C.P. Fleming, L.M. Barwick, K.J. Quan, A.M. Rollins, In-vitro characterization of ablation lesions using oct, *Am. Heart Assoc.* (2008).
- [300] R.P. Singh-Moon, C.C. Marboe, C.P. Hendon, Near-infrared spectroscopy integrated catheter for characterization of myocardial tissues: preliminary demonstrations to radiofrequency ablation therapy for atrial fibrillation, *Biomed. Opt. Express* 6 (7) (2015) 2494–2511.
- [301] D.A. Gil, L.M. Swift, H. Asfour, N. Muselmyan, M.A. Mercader, N.A. Sarvazyan, Autofluorescence hyperspectral imaging of radiofrequency ablation lesions in porcine cardiac tissue, *J. Biophotonics* 10 (8) (2017) 1008–1017.
- [302] S. Iskander-Rizk, P. Kruizinga, A.F.W. van der Steen, G. van Soest, Spectroscopic photoacoustic imaging of radiofrequency ablation in the left atrium, *Biomed. Opt. Express* 9 (3) (2018) 1309–1322.
- [303] S. Iskander-Rizk, P. Kruizinga, R. Beurskens, G. Springeling, F. Mastik, N.M. de Groot, P. Knops, A.F. van der Steen, G. van Soest, Real-time photoacoustic assessment of radiofrequency ablation lesion formation in the left atrium, *Photoacoustics* 16 (2019), 100150.
- [304] S. Bordignon, K.R. Chun, M. Gunawardene, B. Schulte-Hahn, B. Nowak, A. Fuernkranz, B. Schmidt, Endoscopic ablation systems, *Expert Rev. Med Devices* 10 (2) (2013) 177–183.
- [305] V.Y. Reddy, C. Houghtaling, J. Fallon, G. Fischer, N. Farr, J. Clarke, J. McIntyre, E. Sinofsky, J.N. Ruskin, D. Keane, Use of a diode laser balloon ablation catheter to generate circumferential pulmonary venous lesions in an open-thoracotomy caprine model, *Pace* 27 (1) (2004) 52–57.
- [306] M. Basij, A. Karpiouk, I. Winer, S. Emelianov, M. Mehrmohammadi, Dual-illumination ultrasound/photoacoustic system for cervical, *Cancer Imaging, IEEE Photonics J.* 13 (1) (2021).
- [307] M. Basij, A. Karpiouk, I. Winer, S. Emelianov, M. Mehrmohammadi, Dual-illumination ultrasound/photoacoustic endoscopic system, 2020 IEEE International Ultrasonics Symposium (IUS), IEEE, 2020, pp. 1–4.
- [308] M. Basij, Y. Yan, S.S. Alshahrani, H. Helmi, T.K. Burton, J.W. Burmeister, M. M. Dominello, I.S. Winer, M. Mehrmohammadi, Miniaturized phased-array ultrasound and photoacoustic endoscopic imaging system, *Photoacoustics* 15 (2019), 100139.
- [309] K.J. Francis, S. Manohar, Photoacoustic imaging in percutaneous radiofrequency ablation: device guidance and ablation visualization, *Phys. Med. Biol.* 64 (18) (2019), 184001.
- [310] S. Mulier, Y. Ni, J. Jamart, T. Ruers, G. Marchal, L. Michel, Local recurrence after hepatic radiofrequency coagulation: multivariate meta-analysis and review of contributing factors, *Ann. Surg.* 242 (2) (2005) 158.
- [311] L.-H. Lee, J.-I. Hwang, Y.-C. Cheng, C.-Y. Wu, S.-W. Lee, S.-S. Yang, H.-Z. Yeh, C.-S. Chang, T.-Y. Lee, Comparable outcomes of ultrasound versus computed tomography in the guidance of radiofrequency ablation for hepatocellular carcinoma, *PLoS One* 12 (1) (2017).
- [312] K.J. Francis, S. Manohar, Photoacoustic assisted device guidance and thermal lesion imaging for radiofrequency ablation, European Conference on Biomedical Optics, Optical Society of America, 2019, p. 11077_40.
- [313] B.M. Künzli, P. Abitabile, C.A. Maurer, Radiofrequency ablation of liver tumors: actual limitations and potential solutions in the future, *World J. Hepatol.* 3 (1) (2011) 8.
- [314] M. Toi, Y. Asao, Y. Matsumoto, H. Sekiguchi, A. Yoshikawa, M. Takada, M. Kataoka, T. Endo, N. Kawaguchi-Sakita, M. Kawashima, Visualization of tumor-related blood vessels in human breast by photoacoustic imaging system with a hemispherical detector array, *Sci. Rep.* 7 (2017) 41970.
- [315] F. Cao, Z. Qiu, H. Li, P. Lai, Photoacoustic Imaging in Oxygen Detection, *Appl. Sci.* 7 (2017) 1262.
- [316] K. Prame Kumar, C.H.Y. Wong, Imbalance in the force: the dark side of the microbiota on stroke risk and progression, *Curr. Opin. Neurobiol.* 62 (2020) 10–16.
- [317] Z. Deng, Z. Wang, X. Yang, Q. Luo, H. Gong, In vivo imaging of hemodynamics and oxygen metabolism in acute focal cerebral ischemic rats with laser speckle imaging and functional photoacoustic microscopy, *J. Biomed. Opt.* 17 (8) (2012), 081415.
- [318] J.L. Saver, Time is brain—quantified, *Stroke* 37 (1) (2006) 263–266.
- [319] S. Hu, E. Gonzales, B. Soetikno, E. Gong, P. Yan, K. Maslov, J.-M. Lee, L.V. Wang, Optical-resolution photoacoustic microscopy of ischemic stroke, *Photons Plus Ultrasound: Imaging and Sensing 2011*, Int. Soc. Opt. Photonics (2011), 789906.
- [320] B. Ning, N. Sun, R. Cao, R. Chen, K. Kirk Shung, J.A. Hossack, J.M. Lee, Q. Zhou, S. Hu, Ultrasound-aided Multi-parametric Photoacoustic Microscopy of the Mouse Brain, *Sci. Rep.* 5 (1) (2015) 18775.
- [321] M.A. Mohr, D. Bushey, A. Aggarwal, J. Marvin, E.J. Marquez, Y. Liang, R. Patel, J. Macklin, C.-Y. Lee, D. Kim, jyCaMP: An optimized calcium indicator for two-photon imaging at fiber laser wavelengths, *bioRxiv* (2019) 816660.
- [322] C.L. Bayer, B.J. Włodarczyk, R.H. Finnell, S.Y. Emelianov, Ultrasound-guided spectral photoacoustic imaging of hemoglobin oxygenation during development, *Biomed. Opt. Express* 8 (2) (2017) 757–763.
- [323] B. van der Sanden, O. Hugon, M. Inglebert, O. Jacquin, E. Lacot, Vascular bifurcation mapping with photoacoustic microscopy, *Biomed. Opt. Express* 11 (3) (2020) 1298–1305.
- [324] L. Gambardella, E. Zudaire, S. Vermeren, Quantitative analysis of angiogenesis in the allantois explant model, in: E. Zudaire, F. Cuttitta (Eds.), *The Textbook of Angiogenesis and Lymphangiogenesis: Methods and Applications*, Springer, Netherlands, Dordrecht, 2012, pp. 189–204.
- [325] D. Feliciano, I. Espinosa-Medina, A. Weigel, K.M. Milano, Z. Tang, T. Lee, H.J. Kliman, S.M. Guller, C.M. Ott, J. Lippincott-Schwartz, Transcriptional reprogramming in fused cells is triggered by plasma-membrane diminution, *bioRxiv* (2019) 832378.
- [326] T.G. Zybina, E.V. Zybina, Cell reproduction and genome multiplication in the proliferative and invasive trophoblast cell populations of mammalian placenta, *Cell Biol. Int.* 29 (12) (2005) 1071–1083.
- [327] M. Eaton, A.H. Davies, J. Devine, X. Zhao, D.G. Simmons, E. Mariusdóttir, D. R. Natale, J.R. Matyas, E.A. Bering, M.L. Workentine, Complex patterns of cell growth in the placenta in normal pregnancy and as adaptations to maternal diet restriction, *PLoS One* 15 (1) (2020), e0226735.
- [328] G.N. Masoud, W. Li, HIF-1 α pathway: role, regulation and intervention for cancer therapy, *Acta Pharm. Sin. B* 5 (5) (2015) 378–389.
- [329] C.G. Eberhart, P. Argani, Wnt signaling in human development: beta-catenin nuclear translocation in fetal lung, kidney, placenta, capillaries, adrenal, and cartilage, *Pediatr. Dev. Pathol.* 4 (4) (2001) 351–357.
- [330] R.F. Gasser, *Atlas of human embryos*, Medical Department, Harper & Row 1975.
- [331] K. McDole, L. Guignard, F. Amat, A. Berger, G. Malandain, L.A. Royer, S. C. Turaga, K. Branson, P.J. Keller, In toto imaging and reconstruction of post-implantation mouse development at the single-cell level, *Cell* 175 (3) (2018) 859–876, e33.
- [332] A. Sahakyan, K. Plath, Transcriptome encyclopedia of early human development, *Cell* 165 (4) (2016) 777–779.
- [333] A.F. Groff, N. Resetkova, F. DiDomenico, D. Sakkas, A. Penzias, J.L. Rinn, K. Egan, RNA-seq as a tool for evaluating human embryo competence, *Genome Res.* 29 (10) (2019) 1705–1718.
- [334] H. Fang, Y. Yang, C. Li, S. Fu, Z. Yang, G. Jin, K. Wang, J. Zhang, Y. Jin, Transcriptome analysis of early organogenesis in human embryos, *Dev. Cell* 19 (1) (2010) 174–184.
- [335] M. Cross, E. Smith, D. Hoy, L. Carmona, F. Wolfe, T. Vos, B. Williams, S. Gabriel, M. Lassere, N. Johns, R. Buchbinder, A. Woolf, L. March, The global burden of rheumatoid arthritis: estimates from the global burden of disease 2010 study, *Ann. Rheum. Dis.* 73 (7) (2014) 1316–1322.
- [336] F. Angelotti, A. Parma, G. Cafaro, R. Capecchi, A. Alunno, I. Puxeddu, One year in review 2017: pathogenesis of rheumatoid arthritis, *Clin. Exp. Rheuma* 35 (3) (2017) 368–378.
- [337] F.K. Joseph, M. Xavierselvan, M.K.A. Singh, S. Mallidi, C. Van Der Laken, F. Van De Loo, W. Steenbergen, LED-based photoacoustic imaging for early detection of joint inflammation in rodents: towards achieving 3Rs in rheumatoid arthritis research, *Photons Plus Ultrasound: Imaging and Sensing 2020*, Int. Soc. Opt. Photonics (2020) 112400M.
- [338] H. Guo, Q. Wang, W. Qi, X. Sun, B. Ke, L. Xi, Assessing the development and treatment of rheumatoid arthritis using multiparametric photoacoustic and ultrasound imaging, *J. Biophotonics* 12 (11) (2019), e201900127.

- [339] A.G. Bell, On the production and reproduction of sound by light, *Am. J. Sci.* s3 20 (118) (1880) 305.
- [340] A.G. Bell, Upon the production of sound by radiant energy, *Lond., Edinb., Dublin Philos. Mag. J. Sci.* 11 (71) (1881) 510–528.
- [341] P.K. Upputuri, M. Pramanik, Photoacoustic imaging in the second near-infrared window: a review, *J. Biomed. Opt.* 24 (4) (2019) 1–20.
- [342] J. Gamelin, A. Aguirre, A. Maurudis, L.V. Wang, Q. Zhu, Improvements in time resolution of tomographic photoacoustic imaging using a priori information for multiplexed systems, *Photons Plus Ultrasound: Imaging and Sensing 2009*, *Int. Soc. Opt. Photonics* (2009) 71771C.
- [343] P.K. Upputuri, M. Pramanik, Fast photoacoustic imaging systems using pulsed laser diodes: a review, *Biomed. Eng. Lett.* 8 (2) (2018) 167–181.
- [344] Y. Zhu, G. Xu, J. Yuan, J. Jo, G. Gandikota, H. Demirci, T. Agano, N. Sato, Y. Shigeta, X. Wang, Light emitting diodes based photoacoustic imaging and potential clinical applications, *Sci. Rep.* 8 (1) (2018) 9885.
- [345] A. Hariri, J. Lemaster, J. Wang, A.S. Jeevarathinam, D.L. Chao, J.V. Jokerst, The characterization of an economic and portable LED-based photoacoustic imaging system to facilitate molecular imaging, *Photoacoustics* 9 (2018) 10–20.
- [346] J. Jo, G. Xu, Y. Zhu, M. Burton, J. Sarazin, E. Schioppa, G. Gandikota, X. Wang, Detecting joint inflammation by an LED-based photoacoustic imaging system: a feasibility study, *J. Biomed. Opt.* 23 (11) (2018) 1–4.
- [347] R. Bulsink, M. Kuniyil Ajith Singh, M. Xavierselvan, S. Mallidi, W. Steenbergen, K. J. Francis, Oxygen saturation imaging using LED-based photoacoustic system, *Sensors* 21 (1) (2021) 283.
- [348] Y. Zhu, X. Lu, X. Dong, J. Yuan, M.L. Fabiilli, X. Wang, LED-based photoacoustic imaging for monitoring angiogenesis in fibrin scaffolds, *Tissue Eng. Part C. Methods* 25 (9) (2019) 523–531.
- [349] M. Xavierselvan, S. Mallidi, LED-based functional photoacoustics—portable and affordable solution for preclinical cancer imaging, in: M. Kuniyil Ajith Singh (Ed.), *LED-Based Photoacoustic Imaging: From Bench to Bedside*, Springer, Singapore, Singapore, 2020, pp. 303–319.
- [350] S. Agrawal, M. Kuniyil Ajith Singh, K. Johnstonbaugh, D.C. Han, C.R. Pameijer, S.-R. Kothapalli, Photoacoustic imaging of human vasculature using led versus laser illumination: a comparison study on tissue phantoms and in vivo humans, *Sensors* 21 (2) (2021).
- [351] Y. Li, L. Li, L. Zhu, K. Maslov, J. Shi, P. Hu, E. Bo, J. Yao, J. Liang, L. Wang, L. V. Wang, Snapshot photoacoustic topography through an ergodic relay for high-throughput imaging of optical absorption, *Nat. Photonics* 14 (3) (2020) 164–170.
- [352] C. Lee, W. Choi, J. Kim, C. Kim, Three-dimensional clinical handheld photoacoustic/ultrasound scanner, *Photoacoustics* 18 (2020), 100173.
- [353] Q. Huang, Z. Zeng, A review on real-time 3D ultrasound imaging technology, *BioMed. Res. Int.* 2017 (2017) 6027029.
- [354] M.W. Schellenberg, H.K. Hunt, Hand-held optoacoustic imaging: a review, *Photoacoustics* 11 (2018) 14–27.
- [355] M.A. Naser, D.R.T. Sampaio, N.M. Munoz, C.A. Wood, T.M. Mitcham, W. Stefan, K.V. Sokolov, T.Z. Pavan, R. Avritscher, R.R. Bouchard, Improved photoacoustic-based oxygen saturation estimation with SNR-regularized local fluence correction, *IEEE Trans. Med. Imaging* 38 (2) (2019) 561–571.
- [356] A. Pattyn, Z. Mumm, N. Alijabbari, N. Duric, M.A. Anastasio, M. Mehrmohammadi, Model-based optical and acoustical compensation for photoacoustic tomography of heterogeneous mediums, *Photoacoustics* 23 (2021), 100275.
- [357] S. Park, A.A. Oraevsky, R. Su, M.A. Anastasio, Compensation for non-uniform illumination and optical fluence attenuation in three-dimensional optoacoustic tomography of the breast, *Photons Plus Ultrasound: Imaging and Sensing 2019*, *Int. Soc. Opt. Photonics* (2019) 108784X.
- [358] Y. LeCun, Y. Bengio, G. Hinton, Deep learning, *Nature* 521 (7553) (2015) 436–444.
- [359] L. Deng, D. Yu, *Deep learning: methods and applications*, 2014.
- [360] D. Waibel, J. Gröhl, F. Isensee, T. Kirchner, K. Maier-Hein, L. Maier-Hein, Reconstruction of initial pressure from limited view photoacoustic images using deep learning, *Photons Plus Ultrasound: Imaging and Sensing 2018*, *Int. Soc. Opt. Photonics* (2018) 104942S.
- [361] M. Kim, G.S. Jeng, I. Pelivanov, M. O'Donnell, Deep-learning image reconstruction for real-time photoacoustic system, *IEEE Trans. Med. Imaging* 39 (11) (2020) 3379–3390.
- [362] J. Feng, J. Deng, Z. Li, Z. Sun, H. Dou, K. Jia, End-to-end Res-UNet based reconstruction algorithm for photoacoustic imaging, *Biomed. Opt. Express* 11 (9) (2020) 5321–5340.
- [363] E.M.A. Anas, H.K. Zhang, J. Kang, E. Boctor, Enabling fast and high quality LED photoacoustic imaging: a recurrent neural networks based approach, *Biomed. Opt. Express* 9 (8) (2018) 3852–3866.
- [364] H. Lan, D. Jiang, C. Yang, F. Gao, F. Gao, Y-Net: hybrid deep learning image reconstruction for photoacoustic tomography in vivo, *Photoacoustics* 20 (2020), 100197.
- [365] G. Godefroy, B. Arnal, E. Bossy, Compensating for visibility artefacts in photoacoustic imaging with a deep learning approach providing prediction uncertainties, *Photoacoustics* 21 (2021), 100218.
- [366] G. Wang, J.C. Ye, K. Mueller, J.A. Fessler, Image reconstruction is a new frontier of machine learning, *IEEE Trans. Med. Imaging* 37 (6) (2018) 1289–1296.
- [367] M.K.A. Singh, K. Sivasubramanian, N. Sato, F. Ichihashi, Y. Sankai, L. Xing, Deep learning-enhanced LED-based photoacoustic imaging, *Photons Plus Ultrasound: Imaging and Sensing 2020*, *Int. Soc. Opt. Photonics* (2020) 1124038.
- [368] R. Manwar, X. Li, S. Mahmoodkalayeh, E. Asano, D. Zhu, K. Avnaki, Deep learning protocol for improved photoacoustic brain imaging, *J. Biophotonics* 13 (10) (2020), e202000212.
- [369] A. Hariri, K. Alipour, Y. Mantri, J.P. Schulze, J.V. Jokerst, Deep learning improves contrast in low-fluence photoacoustic imaging, *Biomed. Opt. Express* 11 (6) (2020) 3360–3373.
- [370] X. Chen, W. Qi, L. Xi, Deep-learning-based motion-correction algorithm in optical resolution photoacoustic microscopy, *Vis. Comput. Ind. Biomed. Art.* 2 (1) (2019) 12.
- [371] A. DiSpirito, D.W. Li, T. Vu, M.M. Chen, D. Zhang, J.W. Luo, R. Horstmeyer, J. J. Yao, Reconstructing Undersampled Photoacoustic Microscopy Images Using Deep Learning, *Ieee Trans. Med. Imaging* 40 (2) (2021) 562–570.
- [372] J. Zhou, D. He, X. Shang, Z. Guo, S.L. Chen, J. Luo, Photoacoustic microscopy with sparse data by convolutional neural networks, *Photoacoustics* 22 (2021), 100242.
- [373] A. Sharma, M. Pramanik, Convolutional neural network for resolution enhancement and noise reduction in acoustic resolution photoacoustic microscopy, *Biomed. Opt. Express* 11 (12) (2020) 6826–6839.
- [374] C. Cai, K. Deng, C. Ma, J. Luo, End-to-end deep neural network for optical inversion in quantitative photoacoustic imaging, *Opt. Lett.* 43 (12) (2018) 2752–2755.
- [375] C. Yang, H. Lan, H. Zhong, F. Gao, Quantitative photoacoustic blood oxygenation imaging using deep residual and recurrent neural network, *2019 IEEE 16th International Symposium on Biomedical Imaging (ISBI 2019)*, IEEE, 2019, pp. 741–744.
- [376] I. Olefir, S. Tzoumas, C. Restivo, P. Mohajerani, L. Xing, V. Ntziachristos, Deep learning-based spectral unmixing for optoacoustic imaging of tissue oxygen saturation, *IEEE Trans. Med. Imaging* 39 (11) (2020) 3643–3654.
- [377] L.O. America, *American National Standard for Safe Use of Lasers ANSI Z136.1–2014*, American National Standards Institute, Inc Washington, DC2014.
- [378] K.M. Kempfski, A. Wiacek, M. Graham, E. Gonzalez, B. Goodson, D. Allman, J. Palmer, H. Hou, S. Beck, J. He, M.A. Lediju Bell, *In vivo* photoacoustic imaging of major blood vessels in the pancreas and liver during surgery, *J. Biomed. Opt.* 24 (12) (2019) 1–12.
- [379] J. Huang, A. Wiacek, K.M. Kempfski, T. Palmer, J. Izzi, S. Beck, M.A. Lediju Bell, Empirical assessment of laser safety for photoacoustic-guided liver surgeries, *Biomed. Opt. Express* 12 (3) (2021) 1205–1216.